

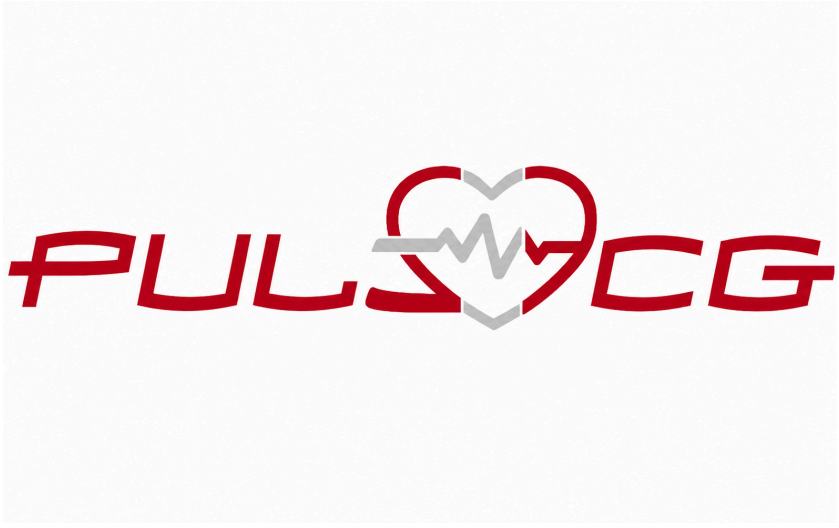
Politecnico di Torino



Department of Electronics and Telecommunications

Master Degree Thesis

Development of two wearable devices for vital signs measurement



Supervisors:

Prof. Eros Pasero
Prof. Vincenzo Randazzo
PhD. Marco Sento

Candidates:

Giuseppe Buonanno
Sofiya Karnaukh

July 2026

Acknowledgements

Innanzitutto desidero ringraziare il mio relatore, il Prof. Vincenzo Randazzo ed il corelatore Prof. Eros Pasero, i quali mi hanno mostrato l'esistenza di un mondo di ricerca e di innovazione che più si allinea ai miei interessi. Infatti, ormai (tanti) anni fa scelsi di iscrivermi ad Ingegneria Elettronica perché attratto dalla possibilità di poter contribuire a migliorare la vita quotidiana delle persone attraverso l'innovazione tecnologica. La mia tesi è stata il primo vero passo verso la concretizzazione di questa idea, che nel futuro della mia carriera conto di proseguire.
Il lavoro di questa tesi, comunque, segna la fine di un percorso accademico durato anni, che non sarebbe stato possibile sostenere senza il supporto e l'incoraggiamento di molte persone! Voglio ringraziare Papà e Mamma, mia sorella Roberta e "mio fratello" Andrea, che mi incoraggiavano ai tempi degli spararagnatele costruiti nello stanzino che adoravo chiamare "laboratorio", ma soprattutto erano lì a darmi sostegno e a ricordarmi ogni giorno quanto fosse importante non mollare mai, specialmente nei periodi più tosti di questo percorso, dove si festeggiava anche per i voti "bassi e fissi".
Un ringraziamento speciale va anche ai miei "amici del mare" Aurora "LolaLadiva", Giada "Pollo 'tosse'", Dario "il mio youtuber preferito, 'forza quattro?'" e tutti gli altri, che tra una "cena a casa di … e ognuno si porta le cose", un bagno a mare fatto alle otto di sera senza il sole e lunghe chiacchierate non hanno mai smesso di farmi sentire parte di un gruppo, anche quando ero lontano da casa.
Parlando di casa, ci tengo a ringraziare anche i miei ormai ex coinquilini Gianmarco e Lorenzo, con i quali abbiamo condiviso momenti indimenticabili nella leggendaria casa Rosselli, le nostre scommesse e "EHHH? 'pernacchia' ", chirurgie improvvisate al dito e corsi accelerati di pizza, gare a chi prendeva per primo il telecomando della TV…
Ringrazio anche i miei amici di Torino, Federico "Palazz", Gaia "Yzma", Daniele "Sergy" e Vincenzo "Kronk" che mi hanno fatto ricredere su questa città che inizialmente non mi era piaciuta, e l'hanno trasformata piano piano in casa, tra un "vieni qua", "ciao mbare", gite fuori porta e somiglianze inaspettate.
Infine, un ringraziamento a tutti i miei compagni di corso (Mauro, Dante, Rong, Ale, Leonardo, Jacopo, Giulia, Pietro, Alice e Martina) e i ragazzi del team PoliTek, con i quali le solite quattro mura di un aula o del laboratorio sono diventate un luogo di collaborazione, risate e supporto dando vita ad amicizie importanti anche (e soprattutto) fuori dalle mura del PollaioTecnico.

Sono grato a tutti voi, siete stati parte di questo percorso e senza di voi non sarei arrivato fin qui.
Grazie di cuore!

Abstract

This thesis describes the development and testing of pulsECG and SLVECG, two wearable prototypes designed for ECG and blood oxygen saturation (SpO_2) monitoring. The project was conceived with the aim of providing patients the ability to monitor these vital parameters without relying on hospital-grade equipment.

From a hardware perspective, both devices share the same core components, including an STM32WB30 microcontroller, selected for managing the Bluetooth Low Energy (BLE) communication stack toward the smartphone, analog circuitry for vital signal acquisition, and an analog-to-digital converter (ADC).

On the software side, a dedicated application was developed in Flutter (Dart language), capable of automatically connecting to both devices and simultaneously acquiring signals from them, ensuring smooth and real-time visualization of the monitored parameters. A significant portion of the work focused on revising previous hardware versions of the project. In particular, a critical issue in the analog-to-digital conversion stage had to be addressed: following an update of the ADC component by the manufacturer, the existing firmware had become obsolete. The ADC firmware management was therefore rewritten to guarantee correct digitalization of the incoming ECG signal. Alongside the electrocardiographic functionality, firmware for an onboard photoplethysmography (PPG) sensor was developed and tested, completing the acquisition system for SpO_2 estimation. The Flutter application was also updated to include PPG waveform visualization and SpO_2 calculation. The validity of the system was confirmed through experimental comparison tests: the saturation values obtained from the pulsECG prototype were consistent with those measured by a certified commercial pulse oximeter, demonstrating the accuracy of the acquisition chain. In conclusion, beyond validating the effectiveness of the proposed architecture for everyday monitoring, this thesis opens the possibility of integrating the developed system with neural interfaces. The system enables reconstruction of the standard 12-lead ECG using only five electrodes, representing a concrete step forward toward advanced, portable, and non-invasive diagnostic solutions.

Contents

1. Introduction 1
1.1. The heart structure 1
1.2. Cardiovascular diseases 2
1.2.1. Bradyarrhythmias 2
1.2.2. Tachyarrhythmias 3
1.3. Impact of CVDs on the population 4
1.4. The Shift Toward Preventive Cardiology 5
1.5. SpO_2 metric 5
1.6. Electrocardiography Overview: the ECG 7
1.6.1. ECG signal format 7
1.6.2. ECG signal leads 7
1.6.3. Visualizing ECG signals: the ECG paper 10
1.7. Electronic measurement implementations 11
1.7.1. Hospital-grade Monitors 11
1.7.2. Holter 11
1.7.3. KardiaMobile family 12
1.7.4. Smartwatches 13
1.7.5. 12-Lead ECG measurement with only 5 electrodes: pulsECG and SLVECG 14
2. Development process 15
2.1. Inital Prototype description 15
2.1.1. Board Overview 15
2.2. ADC part number change 16
2.3. INA bias resistors 18
2.4. Routing anomalies 19
2.5. Other signals acquisition 19
2.6. Reset pushbutton 19
2.7. RF debugging 19
2.8. LED indicators 19
3. Final Devices Composition 20
3.1. Master device ("pulsECG") 20
3.1.1 Circuit overview 21
Power management 21
HPL402323-2C 22
MAX1555EZK+T 23
SLW-66527511-SMT-TR 23
MAX1759EUB 24
BD2242G-GTR 24
REF2025AISDDCR 25
Analog Front-End 26
Electrodes 26
331171302030 27
FFSD-05-D-06.00-01-N and FTSH-105-01-F-DV-K-P-TR 27
INA826AIDR 28
OPA4330AIDR 28
ADC 29

MCP3564RT-E/ST 31
625L3I008M00000 32
SpO_2 acquisition system 33
MAXM86161EFD+T 34
Peripherals 35
MLPF-WB55-01E3 36
EVQ-PUJ02K 37
EAST1616RGBA8 37
USB4085-GF-A 37
STM32WB30CEU5A 38
FA-128 32.0000MF10Z-AJ3 40
CM8V-T1A-32.768kHz-9pF-20PPM-TB-QC 40
3.1.2 Board overview 41
Board configuration 41
PCB assembly 44
PCB enclosure and final assembled device 45
3.1.3 Layout overview 47
Electrodes attachment 47
Domain separation 47
Analog domain routing 48
Digital domain routing 48
Radiofrequency domain 48
3.2. Slave device ("SLVECG") 49
3.2.1. Schematic Diagrams 49
3.2.1.1. Analog Front-End 49
3.2.1.2. Microcontroller 51
3.2.1.3. Power management unit 52
3.2.1.4. Peripherals 52
3.2.2. Board Overview 54
3.2.2.1. Stackup 54
3.2.2.2. Characteristics 55
3.2.3. PCB Case Design 59
4. Firmware development 60
4.1. STM32CubeIDE 60
4.2. STM32CubeProgrammer 60
4.2.1. Flashing the BLE Stack on STM Microcontrollers using STM32CubeProgrammer 60
4.3. Interconnection protocols 61
4.3.1. SPI (Serial Peripheral Interface) 61
4.3.2. I²C 62
4.3.2.1. Physical Layer 62
4.3.2.2. Data Link Layer 63
4.3.2.3. MAXM86161 Supported Operations 64
4.3.2.4. Arbitration 64
4.3.3. DMA 65
4.3.4. Bluetooth© Low Energy (BLE) 65
4.4. Tasks scheduling: the STM32 Sequencer 66
4.5. Code overview 68
4.5.1. main 68
4.5.2. ECG Acquisition 68
4.5.2.1. Setup 69
4.5.2.2. Sequencer tasks 70
4.5.2.3. Bluetooth Services and Characteristics 71
4.5.2.4. Starting an acquisition 72

4.5.2.5. Stopping an acquisition ... 72
4.5.3. SpO_2 Acquisition ... 74
4.5.3.1. Startup ... 74
4.5.3.2. Bluetooth Services and Characteristics ... 74
4.5.3.3. Starting acquisition ... 74
4.5.3.4. Acquiring samples ... 76
4.5.3.5. Stopping acquisition ... 77
5. Mobile Application: pulsECG-X ... 78
5.1. The app engine: Flutter ... 78
5.2. App organization and design ... 79
5.2.1. Icon ... 79
5.2.2. Colors ... 79
5.2.3. Layout ... 80
5.3. App guide page ... 80
5.4. Bluetooth Connectivity page ... 81
5.5. Home Page / Acquisitions page ... 82
5.5.1. Acquisition of ECG signals ... 84
5.5.1.1. Conversion and Filtering of ECG Signals ... 86
5.5.1.2. Limb Leads ... 86
5.5.1.3. Precordial Leads ... 86
5.5.1.4. Complete Display of ECG Waveforms ... 87
5.5.2. ECG Report generation ... 89
5.5.3. SpO_2 acquisition page ... 90
5.5.3.1. Processing logic overview ... 90
5.5.3.2. Filtering ... 90
5.5.3.2.1. The primary pipeline ... 90
5.5.3.2.2. The secondary pipeline ... 92
5.5.3.2.3. Moving variance ... 94
5.5.3.2.4. Autocorrelation ... 95
5.5.3.3. Peaks and valleys detection ... 95
5.5.3.4. Results visualization ... 97
5.5.3.5. Finite State Machine implementation ... 100
5.5.3.6. Reset state ... 101
5.5.3.7. SettlePPG state ... 101
5.5.3.8. SettleFilters state ... 101
5.5.3.9. PeaksEstimation state ... 101
5.5.3.10. Acquisition state ... 101
5.5.3.11. Idle state ... 102
5.6. Devices settings page ... 103
5.6.1. Computation of the battery percentage ... 103
6. Testing and Results ... 105
6.0.1. Participant 1: Male, 26 years old ... 106
6.0.2. Participant 2: Female, 25 years old ... 109
6.0.3. Participant 3: Fluke ProSim 3[1] ... 112
7. SpO_2 testing and results ... 114
7.1. Volunteer 1 ... 115
7.2. Volunteer 2 ... 116
7.3. Volunteer 3 ... 116
7.4. Volunteer 4 ... 118
7.5. Volunteer 5 ... 119
7.6. Observations ... 119
8. Future Improvements ... 120
8.1. Insertion of a neural network for remaining leads ... 120

8.2. Devices minimization and components update 120
8.3. Movement detections systems 120
8.4. PPG sensor substitution 120

List of figures

Figure 1 Heart simplified structure. [2] 1
Figure 2 Myocardium zoomed view. [3] 2
Figure 3 Bundle Branch Blocks and Hemiblocks scheme. [4] 3
Figure 4 Typical ECG Signal. 7
Figure 5 Einthoven's Triangle. 8
Figure 6 Precordial leads visualization.[5] 10
Figure 7 ECG Paper grid layout.[6] 10
Figure 8 Lead 1 on ECG paper. 11
Figure 9 *Mortara ELI 230.*[7] 11
Figure 10 *Cardioline ECG 200L.*[8] 11
Figure 11 A Holter monitoring device model.[9] 12
Figure 12 A KardiaMobile 1L. [10] 13
Figure 13 An Apple Watch with its native App. [11] 13
Figure 14 ECG acquisition. [12] 13
Figure 15 Logo of the thesis project. 14
Figure 16 Top Layer. 15
Figure 17 Bottom layer. 15
Figure 18 Top Layer 3D view. 16
Figure 19 Bottom layer 3D view. 16
Figure 20 SPI response pattern of the MCP3564R [13]. 17
Figure 21 SPI response pattern to a reset command after the fix. 17
Figure 22 *CONFIG0* register bits organization in the MCP3564. [14] 18
Figure 23 *CONFIG0* register bits organization in the MCP3564R.[13] 18
Figure 24 A system-level block diagram of the Master device. 20
Figure 25 A comprehensive power management unit schematic. 22
Figure 26 Photos of the battery and the matching connector. 23
Figure 27 MAX1555EZK 23
Figure 28 SLW-66527511-SMT-TR sliding switch [15] 24
Figure 29 MAX1759EUB 24
Figure 30 BD2242G-GTR 25
Figure 31 REF2025AISDDCR 25
Figure 32 Analog front-end schematic. 26
Figure 33 Copper electrode 27
Figure 34 Connectors for electrodes 27
Figure 35 INA826AIDR 28
Figure 36 OPA4330AIDR 29
Figure 37 A schematic of the ADC and the related circuitry. 31
Figure 38 MCP3564RT-E/ST 32
Figure 39 625L3I008M00000 33
Figure 40 PPG acquisition system diagram. The BLE link is depicted with a blue dotted arrow. The communication between the microcontroller cores is depicted as a double-ended red arrow. 33
Figure 41 A schematic of the PPG sensor and the related auxiliary components. 34
Figure 42 MAXM86161EFD+T 35
Figure 43 The Master device eripherals. 36
Figure 44 MLPF-WB55-01E3 36
Figure 45 EVQ-PUJ02K 37

Figure 46 EAST1616RGBA8 37
Figure 47 USB4085-GF-A package [16] 37
Figure 48 STM32WB30 microcontroller simplified architecture [17]. 38
Figure 49 The microcontroller schematic. 39
Figure 50 STM32WB30CEU5A 40
Figure 51 FA-128 32.0000MF10Z-AJ3 40
Figure 52 The CM8V-T1A-32.768kHz-9pF-20PPM-TB-QC package, top and bottom view [18] 41
Figure 53 PCB layers 43
Figure 54 3D model of the Master device PCB 44
Figure 55 Assembled Master device PCB 45
Figure 56 PCB enclosure, bottom half, six principal views 45
Figure 57 PCB enclosure, top half, six principal views 46
Figure 58 PCB enclosure, 3D view 46
Figure 59 Final assembled Master device 47
Figure 60 *TENS* 3.5 mm jack cable used for the thesis project.[19] 49
Figure 61 Jack port *SJ2-3594A-SMT-TR* used for the SLVECG PCB.[20] 49
Figure 62 *SJ2-3594A-SMT-TR* Pins layout.[20] 50
Figure 63 Analog Front-End of the slave device: amplifiers and hardware low-pass filter. 50
Figure 64 ADC section of the Slave device. 51
Figure 65 Microcontroller mapping of the Slave device. 51
Figure 66 Power management of the Slave device. 52
Figure 67 Peripherals of the slave device. 53
Figure 68 Top Layer. 57
Figure 69 Ground layer. 57
Figure 70 Voltages Layer. 57
Figure 71 Bottom layer. 57
Figure 72 Top layer 3D View. 58
Figure 73 Bottom layer 3D View. 58
Figure 74 Assembled PCB View, front. 58
Figure 75 Assembled PCB View, back. 58
Figure 76 Case 3D View. 59
Figure 77 Final prototype view. 59
Figure 78 SPI configuration with a single peripheral. 61
Figure 79 Example of an SPI transaction, waveforms. [21] 62
Figure 80 A generalized schematic of a physical implementation of I²C interface. 63
Figure 81 A timing diagram of a generalized I2C transaction. Start, Repeated Start and Stop conditions are highlighted in red. 64
Figure 82 Semantic structures of the I²C transactions supported by the MAXM86161. Start, Repeated Start and Stop conditions are represented as S, SR and P, respectively. 64
Figure 83 Characteristics organization of a generic BLE service. 65
Figure 84 Example of BLE GATT transactions. 66
Figure 85 main.c flow of pulsECG. 68
Figure 86 main.c flow of SLVECG. 68
Figure 87 Output format of the MCP3564R for this project. 69
Figure 88 MCP3564R Initialization task flow. 70
Figure 89 ECG Acquisition flow, Devices side. 73
Figure 90 The state diagram of the FSM responsible for the PPG acquisition. 76
Figure 91 The circular buffer for the PPG data samples and its access to by the sequencer and the FSM. 77

Figure 92 App icon style. 79
Figure 93 Final icon result. 79
Figure 94 App colors palette. [22] 79
Figure 95 Appbar. 80
Figure 96 Navigation bar. 80
Figure 97 Guide Page Snapshot. 81
Figure 98 Bluetooth Page, scanning for devices. 81
Figure 99 Connection to pulsECG. 82
Figure 100 Connection to SLVECG. 82
Figure 101 Connection Completed. 82
Figure 102 Acquisitions Page, no selected function. 83
Figure 103 Acquisition countdown. 84
Figure 104 Real-time processing of a received notification, pulsECG device case. 85
Figure 105 Real-time display of Lead I, Lead II and V_2. 85
Figure 106 ECG Acquisition workflow, App side. 86
Figure 107 ECG Debug Menu. 87
Figure 108 FFT of Lead I and lead V_2. 87
Figure 109 Acquired ECG signals. 88
Figure 110 Reconstructed ECG signals. 88
Figure 111 Reconstructed ECG signals, scrolled view. 88
Figure 112 First page of a generated ECG Report. 89
Figure 113 The block diagram of the discrete time-domain filtering of the primary pipeline. 91
Figure 114 The primary pipeline effect on the Red and Infrared channels. The plot is centered on three extrasystoles, which despite filtering retain morphology of a PPG signal. 92
Figure 115 The block diagram of the discrete time-domain filtering of the secondary pipeline. The detailed internal structure is explicitly shown only for the initial biquadratic stage. The subsequent three stages feature an identical schematic topology and differ only by the coefficient values, and are therefore depicted abstractly to preserve visual clarity. 93
Figure 116 The secondary pipeline effect on the Red and Infrared channels. Two cardiac cycles were chosen to depict correspondence between the valley in the MD-filtered data to the end of the dicrotic notch in the raw data with green circles. 94
Figure 117 Triangular structure of the Infrared waveform with the identified bounding valleys (V_1, V_2) and the systolic peak (P_1) for a single cardiac cycle from the reference dataset. The vertical projection of the P1 onto the baseline V_1V_2 defines the magnitude of the AC component of the waveform. The DC component magnitude corresponds to the Y-coordinate of the projected point. 96
Figure 118 Pulse oximeter used for the SpO_2 curve coefficients calibration. [23] 97
Figure 119 Mapping from the standard deviation of the IR signal into the signal stability parameter. 98
Figure 120 Results page with various combinations of active plot options. Due to the signals being bandpass-filtered, they appear superimposed due to the baseline being removed. 99
Figure 121 The diagram of the FSM governing the signal acquisition. 100
Figure 122 The PPG page when FSM is in the Acquisition state. 102
Figure 123 Settings Page: both devices disconnected. 103
Figure 124 Settings Page: both devices connected. 103
Figure 125 Ag/AgCl electrode. [24] 105

Figure 126 Real-time acquisition. 106
Figure 127 Extrasystole in real-time acquisition. 109
Figure 128 112
Figure 129 112
Figure 130 113
Figure 131 113
Figure 132 Measured IR and Red waveforms and metrics. 115
Figure 133 Measured IR and Red waveforms and metrics. 116
Figure 134 Measured IR and Red waveforms and metrics. 117
Figure 135 Measured IR and Red waveforms and metrics. 118
Figure 136 Measured IR and Red waveforms and metrics. 119
Figure 137 Snap connectors for Ag/AgCl electrodes. [25] 120

List of tables

Table 1 Electrical and physical characteristics of the battery [26] 22
Table 2 Electrical and physical characteristics of the charger [27] 23
Table 3 Electrical and physical characteristics of the voltage regulator [28] 24
Table 4 Electrical and physical characteristics of the power switch [29] 25
Table 5 Electrical and physical characteristics of the voltage reference [30] 25
Table 6 Electrical and physical characteristics of the connector and the associated mating cable [31], [32] 28
Table 7 Electrical and physical characteristics of the INA [33] 28
Table 8 Electrical and physical characteristics of OPA4330AIDR [34] 29
Table 9 Comparison of various sampling modes of the MCP3564R 30
Table 10 Electrical and physical characteristics of the ADC [35] 32
Table 11 Electrical and physical characteristics of the ADC oscillator [36] 33
Table 12 Electrical and physical characteristics of the PPG sensor [37] 34
Table 13 All possible LED configurations of the Master device and their meaning. 35
Table 14 Electrical and physical characteristics of the integrated filter [38] 36
Table 15 Electrical and physical characteristics of the RGB LED [39] 37
Table 16 Electrical and physical characteristics of the microcontroller 39
Table 17 Master device PCB stackup: table and cross-section schematic (not to scale) .41
Table 18 Master device PCB order parameters 42
Table 19 Master device stencil order parameters 42
Table 20 Trace width calculation parameters for the RF signals 48
Table 21 Slave device PCB stackup: table and cross-section schematic (not to scale) . . 54
Table 22 Slave device PCB order parameters. 55
Table 23 Slave device stencil order parameters. 56
Table 24 Payload sizes depending on the GATT Operation.[40] 66
Table 25 Seuqencer tasks related to the ECG acquisition 70
Table 26 BLE GATT entries used for ECG data transfer, pulsECG device 71
Table 27 BLE GATT entries used for ECG data transfer, SLVECG device 71
Table 28 Seuqencer tasks related to the PPG sensor 74
Table 29 BLE GATT entries used for PPG data transfer 74
Table 30 MAXM86161 register initialization values 74
Table 31 Battery Level Lookup Table. 104

Glossary

Chapter 1

Introduction

1.1. The heart structure

The heart is the most important muscle within the human body. It is mainly composed by *Myocardial* tissue, or the ***myocardium***, which can be divided into *working myocardium* and *specific myocardium* (Figure 2). The working myocardium is almost entirely composed by muscle cells forming a thick wall structure for ventricles and atria, and its task is pumping blood throughout the body. The specific myocardium, instead, is responsible of generating and propagating *electrical signals* that constitute a heartbeat. Therefore, the specific myocardium tissue is composed by conduction cells, also called *Purkinje fibres*. Through the coordinated action of its atria, ventricles, and valves, the heart produces a rhythmic contraction that pumps blood to the rest of the body.

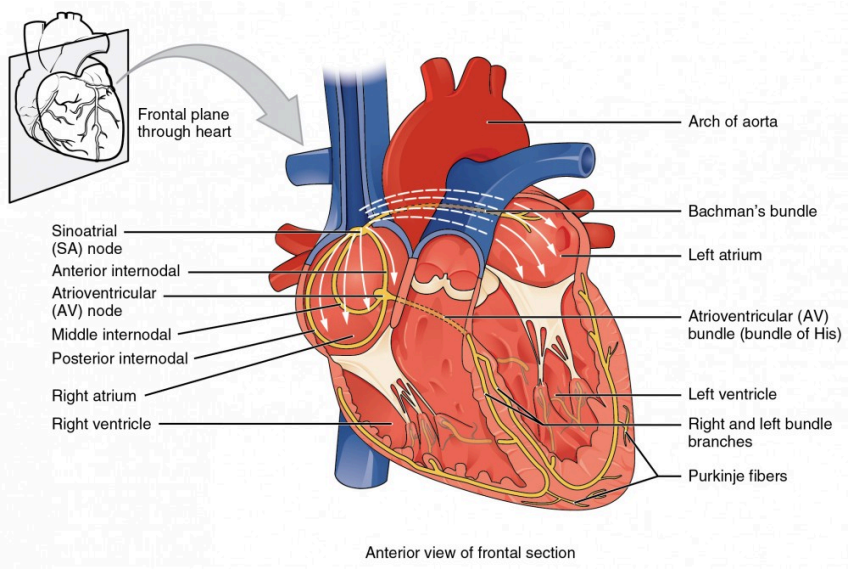


Figure 1: Heart simplified structure. [2]

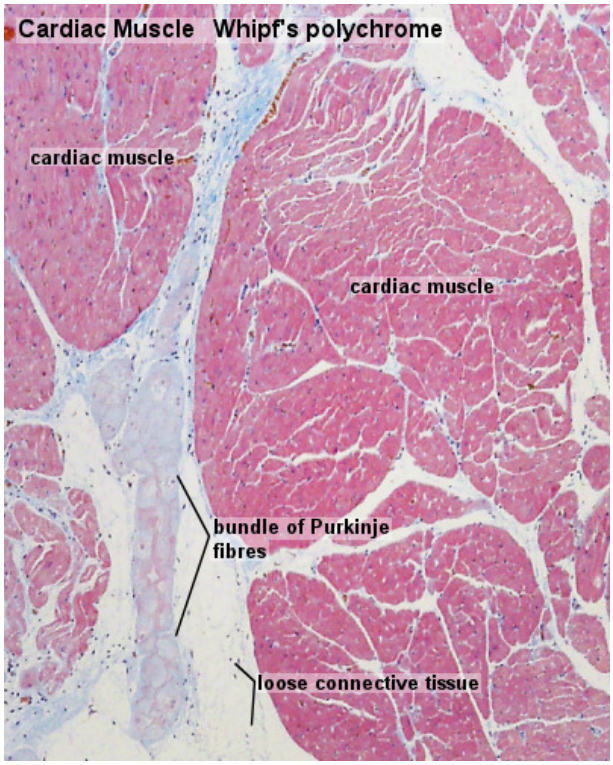


Figure 2: Myocardium zoomed view. [3]

1.2. Cardiovascular diseases

With the previous concepts in mind, a distinction between several pathologies can be made:

- Muscle portion pathologies such as Myocarditis and myocardial infarction (heart attack).
- Blood vessels pathologies: Coronary Heart Disease (*CHD*) i.e., blockage of vessels feeding blood to the heart, brain, or arms and legs (*peripheral arterial diseases*). Such pathologies often lead to severe conditions like strokes or heart attacks, given the poor flow of blood.
- **Arrhythmias**: slower, faster, or irregular rhythm of the patient's heartbeat. More precisely, arrhythmias can be divided into *bradyarrhythmias* and *tachyarrhythmias*.

1.2.1. Bradyarrhythmias

Bradyarrhythmias cause a slowed heartbeat rhythm. Several variations of this condition exist:

- *Sinus Bradycardia*: the affected patient's average rhythm is around 60 bpm or less, reaching 50 bpm or fewer in some cases. Overall, this condition does not affect the morphology of the *QRS* complex of the patient's ECG.
- *Sinoatrial (SA) block*: electrical impulses discharged in the sinoatrial node are conducted to the atria with a delay or are blocked entirely.
- *Atrioventricular (AV) block*: such blocks can be distinguished into three degrees according to the electrophysiological characteristics:
  - First-degree AV block: the conduction time from the atria to the ventricles through the AV node is prolonged consequently giving a prolonged PR interval.
  - Second-degree AV block: can be subdivided into *Mobitz Type 1* and *Mobitz Type 2*. Type 1 manifests as a gradually increasing blockage (known as *Wenckebach block*) of the electrical pulses until a ventricular beat is dropped, whereas Type 2 occurs sporadically and without the occurring of Wenckeback blocks.
  - Third-degree AV block: no electrical pulses are conducted from the atria to the ventricles. Given its severe effect, it is also called **complete heart block** or **complete atrioventricular block**.

- **Bundle Branch Block (BBB)**: a block of a *bundle branch* (seen in Figure 1) which propagates depolarization signals through the ventricles. A BBB can be either complete or incomplete.
  - Right Bundle Branch Block (RBBB): it affects the bundle branch responsible for propagating the depolarization signal to the right ventricle.
  - Left Bundle Branch Block (LBBB): it affects the left bundle branch which propagates electrical signals to the left ventricle.
- **Fascicular Block**: Given the fork-like structure of the left bundle branch (which can be seen in Figure 3), a fascicular block affects one of the structural branches called **fascicles**. A Left Posterior Fascicular Block (*LPFB*) affects the left posterior fascicle, whereas a Left Anterior Fascicular Block (*LAFB*) affects the left anterior fascicle. A fascicular block is also known as a *hemiblock*.

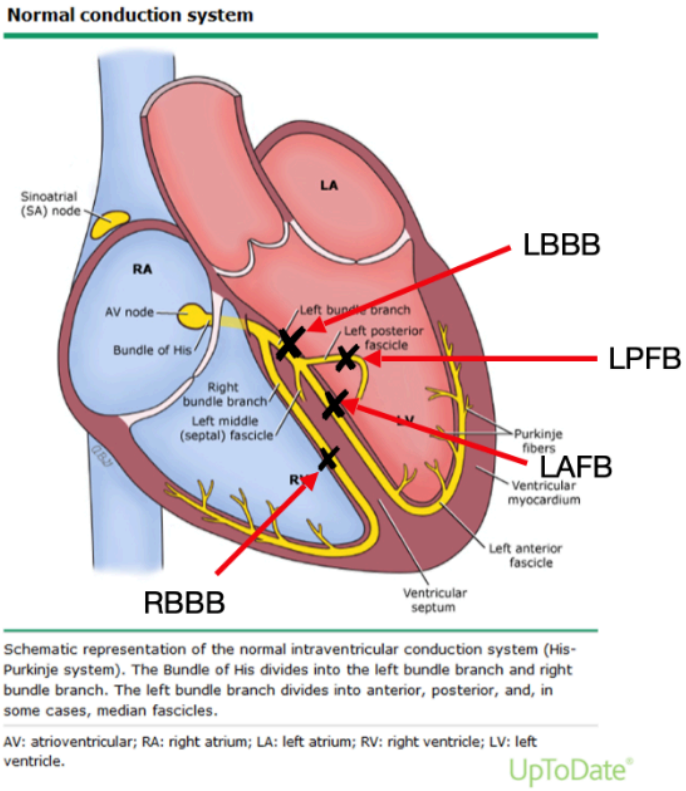


Figure 3: Bundle Branch Blocks and Hemiblocks scheme. [4]

1.2.2. Tachyarrhythmias

Tachyarrhythmias cause an acceleration of the heartbeat rhythm, reaching 100 bpm or greater. Tachyarrhythmias are distinguished between *Supraventricular tachycardias* (originating above the ventricles) and *Ventricular tachycardias* (originating within the ventricles).

Supraventricular tachycardias include:

- *Sinus Tachycardia*: electrical signals from the heart's sinoatrial (*SA*) node instruct the heart to beat faster than normal. This is commonly caused by physiological stressors like fear, exercise, fever, or dehydration.
- *Paroxysmal Supraventricular Tachycardia (PSVT)*: fast-travelling electrical impulses generated above the ventricles, causing a rapid heartbeat rhythm. Such events start and end abruptly. In most cases, these pulses are trapped within a specific reentrant loop, for instance:
  - *Sinus Nodal Reentrant Tachycardia (SNRT)*: signals are trapped in a looping path (hence the name *reentrant*) within or immediately adjacent to the sinus node.

  - *Atrioventricular Nodal Reentrant Tachycardia (AVNRT)*: the loop is formed inside the atrioventricular node using fast and slow pathways.
- *Supraventricular Extrasystole (PAC)*: the result of a premature activation of the atria. They can present as isolated extra heartbeats (felt as skipped beats) or in runs.
- **Atrial Fibrillation (AFib)**: diagnosed by a completely chaotic and unpredictable rhythm pattern. The atria do not contract properly due to disorganized, high-frequency electrical signals.
- **Atrial Flutter**: caused by a rapid, organized macro-reentrant loop around the atria, reaching atrial rates of 250 to 350 bpm. To protect the ventricles from these extreme speeds, the AV node acts as a filter, allowing only every second, third, or fourth beat to pass (creating a conduction **Ratio**). For instance, a 2:1 ratio halves the ventricular rate to a steady 150 bpm. The distinctive trait of atrial flutter is the **sawtooth-like** pattern (F-waves) recognizable on the patient's ECG. Atrial flutter is divided into **typical** (looping through the **Cavotricuspid Isthmus - CTI** in the right atrium) and **atypical** (occurring in other atrial regions).

Among ventricular tachycardias, instead, there are:
- *Ventricular Extrasystoles (PVC)*: ventricular extrasystoles consist in a premature activation of ventricles, giving isolated episodes of extra beats, on the same manner of supraventricular extrasystoles.
- *Ventricular Tachycardia*: often referred as *VT*, is a disease focused on the heart ventricles, where more than one ventricle continuously operate, they open and close faster than normal not giving a proper blood pump to the rest of the body. The result of the exaggerated working speed of ventricles leads to rates ranging from 150 to 250 bpm.
- *Ventricular Flutter*: on a similar way of atrial flutter, such disease affects the ventricular region creating a loop for electrical signals on the lower chambers of the heart. Being ventricles the affected region and the high achieved rates (200 to 350 bpm), the ventricular flutter status often degenerates onto a ventricular fibrillation within minutes after a flutter episode.
- **Ventricular Fibrillation**: it is considered as the most lethal heart rhtyhm disease existing, given the complete disorder and unpredictability of the heart rate during the disease manifestation. During a ventricular fibrillation, the heart rate achieves extremely abnormal speeds (up to 300 bpm), leading to cardiac arrest and eventually death if the patient is not immediately sustained by medical intervention.

1.3. Impact of CVDs on the population

According to the latest data from the *World Health Organization* (WHO) and the *American Heart Association* (AHA) 2026 Update, the global impact of CVD is staggering: approximately 19.8 to 20 million deaths occur annually due to CVD, accounting for roughly 32% of deaths globally. Of such a percentage, 85 % is covered by heart strokes and heart attacks. CVDs deaths transcend geographic and socioeconomic boundaries: over 3 out of 4 deaths by CVDs occur in poor and middle-placed countries, and cover more than 38% of premature deaths (deaths occurring before the age of 70 years). High systolic blood pressure remains the single largest contributor to CVD mortality (responsible for 10.8 million deaths), followed by high BMI and high LDL cholesterol. Over 612 million people are currently living with some form of cardiovascular condition.

The annual global cost of CVD management and lost productivity is measured in the trillions, with the U.S. alone exceeding 417 billion dollars annually. Modern cardiology focuses on identifying and managing "intermediate" risk factors before they escalate into major events:
- Physiological: Hypertension (high blood pressure), diabetes (high blood glucose), and hyperlipidemia (high cholesterol).
- Behavioral: Tobacco use (including a rising concern over nicotine/vaping), physical inactivity, and unhealthy diets high in sodium.
- Environmental: Increasingly recognized in 2026, factors like air pollution and lead exposure are now cited as significant non-traditional drivers of CVD burden, particularly in low-to-middle-income countries.

1.4. The Shift Toward Preventive Cardiology

Given the increasing amount of affected people by CVDs and especially arrhythmias, the **European Heart Rhythm Association (EHRA)** has invited communities and healthcare systems to "Feel the Pulse"[41] on Pulse Day (March 1). It consisted in giving simple steps to raise awareness of these often neglected conditions but of severe nature. The EHRA attempt is part of the biggest focus in medicine on Preventive Cardiology. Such field invites people to take care and track their heart health outside hospital environments by also exploiting emergent technologies such AI diagnostics to Digital Health system & Wearable devices. The latter ones, in form of smartwatches and clinical-grade wearables, can even detect silent arrhythmias like atrial fibrillations on early stages by constantly **measuring the patient's ECG** and other cardiovascular health parameters, such as peripheral oxygen saturation.

1.5. SpO_2 metric

Peripheral oxygen saturation (SpO_2) reflects the relative amount of oxygen in peripheral blood vessels. The monitoring of this parameter became particularly critical during the COVID-19 pandemic due to widespread pulmonary complications that induced low blood oxygen levels (hypoxemia). Crucially, hypoxemia often does not manifest with obvious clinical symptoms, such as dyspnea or cyanosis, until the oxygen level becomes dangerously low. Additional scenarios where SpO_2 monitoring is vital include workout fatigue estimation, sleep apnea detection (via nocturnal monitoring to identify cessation of breathing), and operations in extreme environments, such as decompression ascents during deep-sea diving or firefighting where ambient oxygen is depleted by combustion.

From a mathematical perspective, SpO_2 is the ratio of hemoglobin bound with oxygen to the total hemoglobin level in capillary blood:

$$\mathrm{SpO_2} = 100 \times \frac{C[\mathrm{HbO_2}]}{C[\mathrm{HbO_2}] + C[\mathrm{RHb}]} \tag{1}$$

where $C[\mathrm{HbO_2}]$ is the concentration of oxyhemoglobin, or O_2-bound hemoglobin, and $C[\mathrm{RHb}]$ is deoxy-hemoglobin, which is deprived of oxygen.

The concentrations of these two hemoglobin species affect the monochromatic light absorption, which can be expressed with Beer-Lambert law as:

$$I(\lambda) = I_0(\lambda) e^{-d \sum_i C_i \varepsilon_i(\lambda)} \tag{2}$$

where C_i is concentration of the i-th molecule species in the solution, d is the optical path length, and $\varepsilon_i(\lambda)$ is the molar extinction coefficient of that species at a specific wavelength λ.

Oxyhemoglobin and deoxyhemoglobin have absorption peaks in 500–1000 nm window, whereas water and other substances either don't absorb in this window or are in negligibly small concentrations. This allows to simplify the equation:

$$I(\lambda) = I_0(\lambda) e^{-d\left(C_{\mathrm{HbO_2}} \varepsilon_{\mathrm{HbO_2}}(\lambda) + C_{\mathrm{RHb}} \varepsilon_{\mathrm{RHb}}(\lambda)\right)} \tag{3}$$

The absorbance can be measured at two different wavelengths by photoplethysmography (PPG), which will produce a non-linear system of two equations with two unknowns. The system solution is usually approximated as a parabolic relationship between SpO_2 and R, known as ratio of ratios and calculated as:

$$R = \frac{\mathrm{AC_{Red}} \ / \ \mathrm{DC_{Red}}}{\mathrm{AC_{IR}} \ / \ \mathrm{DC_{IR}}} \tag{4}$$

The parabolic relationship is:

$$\mathrm{SpO_2} = aR^2 + bR + c \tag{5}$$

where a, b and c are empirical calibration constants unique to the specific optical acquisition system.

Finally, a universal baseline reference value for SpO_2 cannot be rigidly established due to it depending on many factors. For instance, the baseline values decrease with the elevation of the patient, with median values ranging from 96-98% on 2000 m to 98-99% on 154 m above sea level [42]. Under standard sea-level conditions, a range between **96% and 100%** is widely accepted as a clinical norm.

1.6. Electrocardiography Overview: the ECG

The entirety of cardiovascular diseases can be diagnosed and eventually treated by observing a patient's electrocardiogram (or **ECG**), given its repeated structure among each heartbeat. Therefore, diving into technological implementations and details requires to give an overview on ECG signals first.

1.6.1. ECG signal format

An ECG signal represents the time evolution of the heart's electrical activity, i.e. the voltage between two points across the human body. A typical ECG signal can be seen as a composition of several waves:

- **P Wave**: it represents the depolarization of the *atria* of the heart, it can be seen as a small and positive deflection from the *baseline* (0 V);
- **Q Wave**: negative deflection with respect to the baseline, it's part of the QRS Complex;
- **R Wave**: the highest and narrowest peak present on the ECG signal, part of QRS Complex as well;
- **S Wave**: another negative deflection, greater in modulus than the Q wave, and final component of the QRS Complex;
- **QRS Complex**: the union of the previously cited Q, R, and S waves. It's meaningful to observe as it shows the ventricular polarization;
- **T Wave**: it represents ventricular repolarization and it's shown as a positive deflection with respect to the baseline;

One can also define:

- **PR Segment**: the baseline distance between the end of the P wave and the beginning of the Q wave;
- **PR Interval**: the length from the starting points of the P wave and the Q wave, respectively;
- **QT Interval**: it represents the interval between the starting point of the Q wave and the end of the T wave;
- **ST Segment**: covers the distance from the ending of the S segment to the starting point of the T wave;

Given definitions within an ECG signal can be observed in Figure 4.

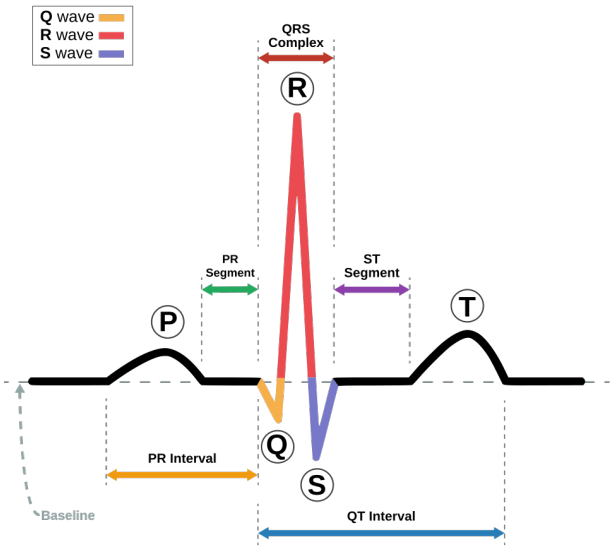


Figure 4: Typical ECG Signal.

1.6.2. ECG signal leads

The ECG signal can be observed from various perspectives of the heart. As a consequence, the ECG signal is usually studied in terms of **Leads**, giving a wider observation window for detecting diseases. In Electrocardiography, it's common to study and analyze the heart electrical activity from two planes

perspective, a vertical and a horizontal one, intersected with each other. The former plane, usually referred as the **Einthoven's Triangle**, can be pictured as an upside-down triangle having the heart on the center. The three points connecting to the triangle are respectively:

- **RA**: Right Arm;
- **LA**: Left Arm;
- **LL**: Left Leg;

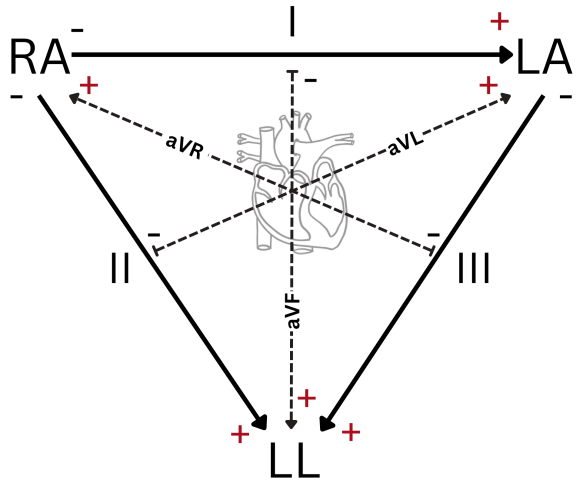


Figure 5: Einthoven's Triangle.

The sides of the triangle, called *Bipolar Leads*, represent a voltage difference between each point. In particular they are defined as:

- **Lead I** : voltage difference between Left Arm and Right Arm i.e. *LA-RA*;
- **Lead II** : voltage difference between Left Leg and Right Arm i.e. *LL-RA*;
- **Lead III** : voltage difference between Left Leg and Left Arm i.e. *LL-LA*;

There exists the **Einthoven's Rule** which states that:

$$\mathbf{II} = \mathbf{I} + \mathbf{III} \quad \text{or equivalently} \quad \mathbf{III} = \mathbf{II} - \mathbf{I} \tag{6}$$

Furthermore, as shown in Figure 5, there are leads placed with a certain angle with respect to the center of the heart (also called ***Wilson Central Terminal*** or **WCT**). It's important to mention that the WCT acts as a *virtual* electrode. Observing the heart from vertices of the Einthoven's triangle to the center of the heart (WCT) introduces other leads called *augmented leads*, and they are:

- **aVR**: stands for augmented Vector Right, and it's positioned with a $-150°$ degree angle, the observation point is the right shoulder;
- **aVL**: stands for augmented Vector Left, and it's positioned with a $-30°$ degree angle, the observation point is the left shoulder;
- **aVF**: stands for augmented Vector Foot, and it's positioned with a $+90°$ degree angle, the observation point is the left foot;

In this way, a *hexaxial* system is completed since the frontal/vertical plane is also divided into sections having a 30° amplitude. It is necessary to mention that augmented leads, unlike leads I, II and III do not require to be observed as a potential difference within two points but rather from a specific point with a relative reference i.e. the WCT. For such reason, augmented leads are part of the *Unipolar* leads. Augmented leads can be computed using the **Goldberger's Formulas**

$$\mathbf{aVR} = \mathbf{RA} - \frac{\mathbf{LA} + \mathbf{LL}}{\mathbf{2}} \tag{7}$$

$$\mathbf{aVL} = \mathbf{LA} - \frac{\mathbf{RA} + \mathbf{LL}}{\mathbf{2}} \tag{8}$$

$$\mathbf{aVF} = \mathbf{LL} - \frac{\mathbf{RA} + \mathbf{LA}}{\mathbf{2}} \tag{9}$$

But they can also be related to the Bipolar leads by recalling their definition, thus obtaining:

$$\mathbf{aVR} = -\frac{\mathbf{I} + \mathbf{II}}{\mathbf{2}} \tag{10}$$

$$\mathbf{aVL} = \frac{\mathbf{I} - \mathbf{III}}{\mathbf{2}} = \mathbf{I} - \frac{\mathbf{II}}{\mathbf{2}} \tag{11}$$

$$\mathbf{aVF} = \mathbf{II} - \frac{\mathbf{I}}{\mathbf{2}} = \frac{\mathbf{II} + \mathbf{III}}{\mathbf{2}} \tag{12}$$

The latter relations show the feasibility to measure leads I, II, III, aVR, aVL and aVF placing electrodes on the right arm (RA), left arm (LA), and left leg (LL) only.

When the human body is observed from the transversal/horizontal plane, instead, electrical pulses moving towards the sternum or the spinal column can be analyzed.
This point of observation introduces six more unipolar leads, called *Precordial* leads, which are:

- $\boldsymbol{V_1}$: placed on the right side of the sternum, at the fourth intercostal space;
- $\boldsymbol{V_2}$: placed on the left side of the sternum, at the fourth intercostal space;
- $\boldsymbol{V_3}$: placed between V_2 and V_4 on the fifth costal cartilage;
- $\boldsymbol{V_4}$: placed on the left midclavicular line, at the fifth intercostal space;
- $\boldsymbol{V_5}$: placed on the left anterior axillary line, at the same level of V_4;
- $\boldsymbol{V_6}$: placed on the left midaxillary line, at the same level of V_4;

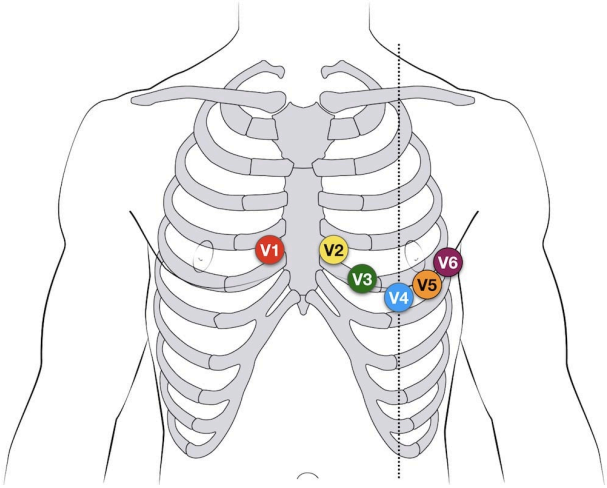


Figure 6: Precordial leads visualization.[5]

1.6.3. Visualizing ECG signals: the ECG paper

In the cardiology field, ECG signals are usually printed on a special grid-like paper to show their behavior over a certain period of time. Considering the grid of such paper, its role is to divide the paper into small squares of 1 *mm* each:

- The horizontal side represents 0.04 seconds;
- The vertical side represents 0.1 millivolts;

Every 5 small squares, both horizontally and vertically, a thicker line is marked, and it visually forms a bigger square of 5 mm per side which represents:

- 0.2 seconds horizontally;
- 0.5 millivolts vertically;

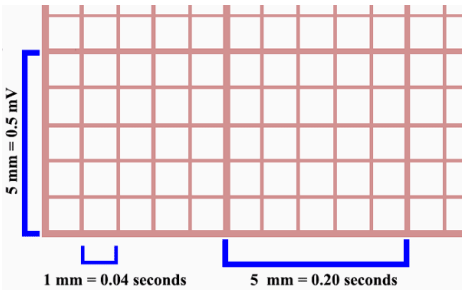


Figure 7: ECG Paper grid layout.[6]

A sequence of 5 big squares represents 1 second on the horizontal axis. Given the previous considerations, **the ECG signal printed on the paper moves with a speed of *25 mm/s***. An example of a printed lead on ECG paper is shown below:

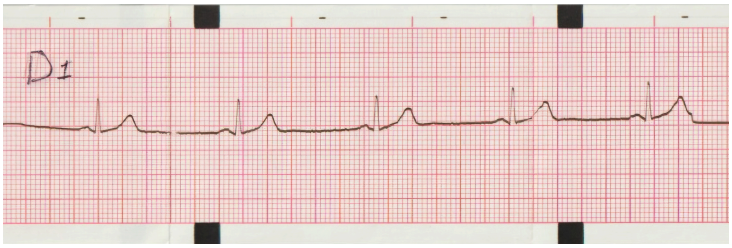


Figure 8: Lead 1 on ECG paper.

Therefore, ECG measurement devices often display the patient's ECG following the abovementioned guidelines.

1.7. Electronic measurement implementations

While instruments for ECG measurement exist since 1887, with the first one being developed by Einthoven himself [43] evolving into modern hospital-grade instrumentation afterwards. Nowadays, a wide range of monitoring devices exists on the market, from hospital-grade devices to non-invasive solutions for domestic usage.

1.7.1. Hospital-grade Monitors

Starting from hospital environments devices, they are designed to measure a reliable, complete 12-Lead patient's ECG. A set of 10 electrodes is attached to the patient's body : **four** on each limb (*RA, LA, RL, LL*) and **six** on the precordial region (V_1 to V_6) to perform the measurement. The electrodes are then connected to the machine which continously displays all 12 ECG waveforms, as well as blood oxygen levelSpO_2), blood pressure and respiration. All these medical informations can also be printed on paper, to give to the medical staff and cardiologists a practical report of the patient's health status. For the abovementioned reasons, such machines are quite complex to design, and therefore their average cost reaches a couple of thousand euros. As of July 2026, two major names in the field are **Mortara** and **Cardioline**. Given the cost, complexity and especially the size of these machines, their usage is often limited to hospital/ambulatory use.



Figure 9: *Mortara ELI 230.*[7]

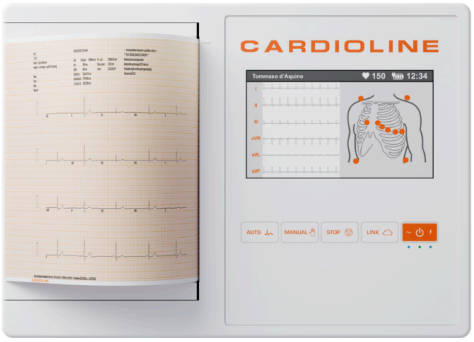


Figure 10: *Cardioline ECG 200L.*[8]

1.7.2. Holter

A known portable device is the **Holter**, which requires the patient to wear adhesive electrodes on limbs and chest linked to the device.

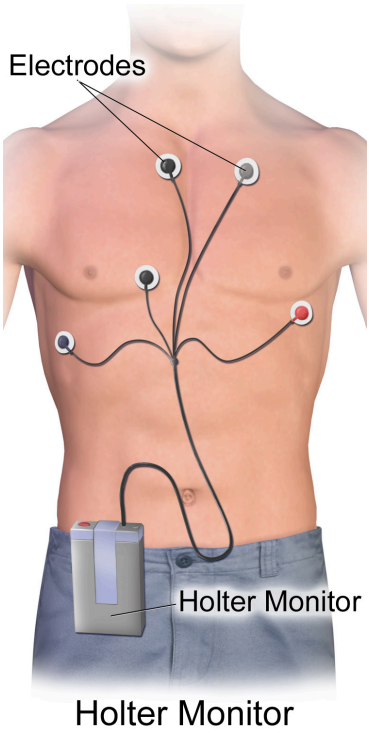


Figure 11: A Holter monitoring device model.[9]

A Holter grants a continuous observation of the patient's ECG signal for abnormalities in the heartbeat (and in case of their *pacemaker* status) also outside ambulatory environments, with ranging costs. However, depending on the usage conditions such as weather (humidity, temperature), the electrodes may fall off the patient's body affecting the measurement quality. Some patients skin may also become sensitive and irritated after a prolonged contact with the adhesive material of the electrodes. Furthermore, wearing a Holter device electrodes may affect the patient's lifestyle during the required measurement time window (usually 24 hours).

1.7.3. KardiaMobile family

The KardiaMobile family of devices, as per July 2026, offers two devices on the market:

- KardiaMobile 1L: device meant to measure Lead I by placing a finger on both ends of the device body.
- KardiaMobile 6L: a device born to measure all the hexaxial system Leads i.e. Leads I-III and aVR, aVL, aVF. The usage is analog to its predecessor, however including the left leg with a bottom electrode.

Both of these devices show the ECG within the associated smartphone app, the latter one can monitor atrial fibrillations, bradycardias, tachycardias and sinus rhytm.



Figure 12: A KardiaMobile 1L. [10]

The cost of both devices is relatively low. However, some diagnostic functions are blocked by a paywall, and the device cannot be used by subjects having a pacemaker since there can be interferences with their usage. In the end, the user needs to keep a steady contact with the device electrodes which can result in uncomfortable body positioning to artefacts on the ECG trace.

1.7.4. Smartwatches

Nowadays almost every *smartwatch* embeds the ECG measurement functionality. One electrode usually sits on the watch bottom part and the other on the side of the watch body granting a snug fit; the widely used device families are the **Apple Watch** and **Galaxy Watch**. Such devices register the patient's ECG Lead I for a short amount of time (around 30 seconds), generating a report with the recorded Lead directly on the associated smartphone app.

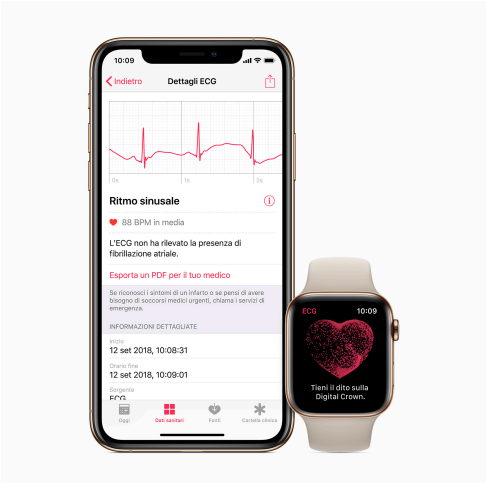


Figure 13: An Apple Watch with its native App. [11]

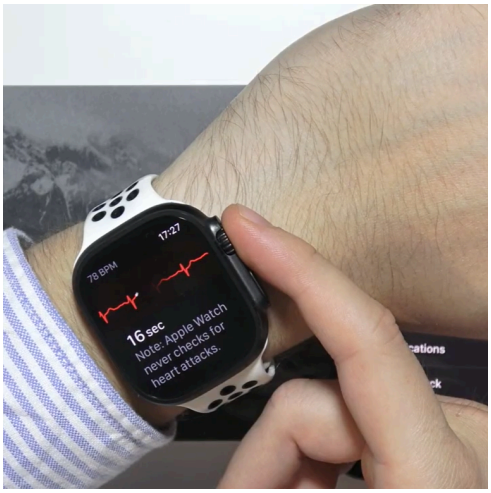


Figure 14: ECG acquisition. [12]

Despite their ease of use, portability, and the capability of flagging a general arrhythmias, these devices are designed for a general purpose usage and not a strictly medical one. Moreover, Lead I in cardiology is not often used to diagnose other conditions, Lead II is instead chosen for the greater view of the P wave.

1.7.5. 12-Lead ECG measurement with only 5 electrodes: pulsECG and SLVECG

In the current state of art, a complete 12-Lead ECG is performed by attaching 10 adhesive electrodes on the patient's body, limiting a reliable measurement to hospital-grade instrumentation only. Following the results of the study by Smith et al. (2021) [44], it has been demonstrated that by placing just five electrodes on the human body, it is possible to accurately reconstruct a full 12-lead ECG exploiting **advanced neural network processing**. These results served as the basis for this thesis project, which provides hardware devices and a smartphone application designed for easy extension to host such a neural network. The proposed methodology utilizes a five-electrode placement, consisting of four electrodes on the limbs and one precordial electrode at the V2 position, to generate seven initial leads: I, II, III, aVL, aVR, aVF, and V2. These seven leads serve as the primary inputs for a *Focus Time-Delay Neural Network* (*FTDNN*), which is specifically trained to derive the remaining five precordial leads: V1, V3, V4, V5, and V6. Validated using an archived medical database of 549 ECG recordings, the FTDNN achieved high quantitative performance, with reconstructed leads showing correlation values between **0.8609 and 0.9678 and low Root Mean Square Error (*RMSE*) values ranging from 123 μV to 245 μV.** The clinical significance of this approach lies in its ability to provide a "gold-standard" 12-lead output while minimizing the electrode placement errors and the time-consuming nature of traditional 12-lead setups.



Figure 15: Logo of the thesis project.

This study opens the door to this thesis project, which can effectively evolve into a reliable solution by using 2 devices for a total of 5 electrodes and a smartphone App, on which an AI-enhanced diagnostic tool can be planted. The first device, called *pulsECG* is endowed with 3 electrodes to measure Leads I-III and aVR, whereas the SLVECG device is meant to measure Lead V_2 referred to the Right Leg (RL) using 2 adhesive electrodes for a total of 5.

Chapter 2

Development process

The thesis project started with a given prototype design, which has been assembled twice, to allow the measurement of the wanted leads and to eventually test the Bluetooth interconnection feasibility.

2.1. Inital Prototype description

2.1.1. Board Overview

The first analyzed prototype was a two-layered *FR-4* board, with the top layer containing all the components of the circuit with the exception of the optional ones for the temperature sensor, that have been placed on the bottom layer. The device development has started with the given PCB and the corresponding firmware. The prototype acquires the limb leads I and II with 3 electrodes that need to be positioned at right arm (RA), left arm (LA), and left leg (LL) of the patient. The lead III and the leads aVR, aVF, aVL are reconstructed in software using the Einthoven's triangle and Goldberg's central terminal concept, as previously mentioned.
The signal from the electrodes is amplified by two instrumentation amplifiers (INA826AIDR) and filtered with low pass filters implemented with a quad operational amplifier (OPA433A0). The leads are then sampled by a 24-bit ADC (MCP3564R), read by the microcontroller over SPI and sent to the end device over Bluetooth Low Energy. The schematic and layout of the PCB prototype were developed in KiCAD, therefore it has been decided to use it for this thesis project.

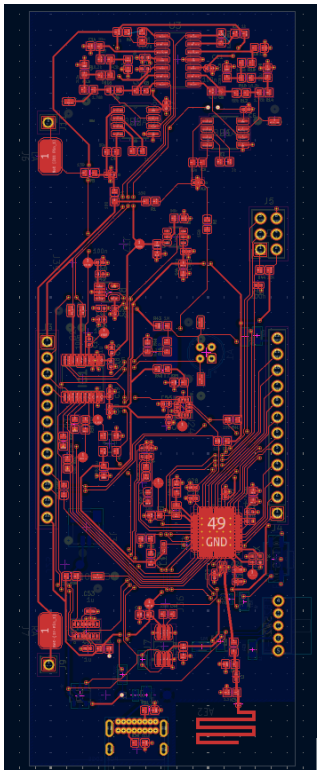
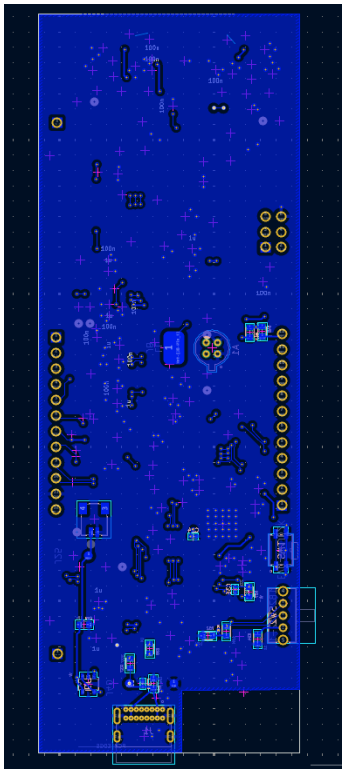


Figure 16: Top Layer.


Figure 17: Bottom layer.

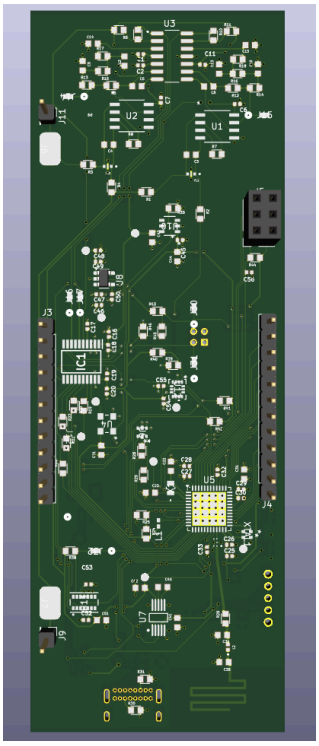


Figure 18: Top Layer 3D view.

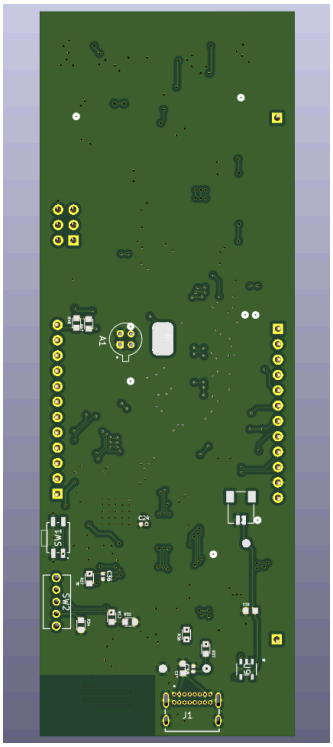


Figure 19: Bottom layer 3D view.

The first step of the development consisted in reviewing the PCB prototype, testing its performance and evaluating possible ways of improvement.

2.2. ADC part number change

A discrepancy between the actual and nominal part numbers of the ADC was identified. The component was recorded as MCP3564 [14], whereas the actual part was the MCP3564R variant. The only difference between the two devices is the presence of an internal reference voltage generator in the MCP3564R. Consequently, one bit of the configuration register *CONFIG0* of MCP3564R is reserved for selection of the internal reference [13]. The prototype firmware was developed for the nominal model and hence programmed this bit with an incorrect value, leading to the ADC defaulting to the internal reference. To display the response of the ADC, puTTY has been used via the *UART* interface of the microcontroller, which was configured via firmware to print the ADC codes after 10 seconds of conversion. However, the result of the register setting incongruence was shown as ADC codes being zero.
To understand the root cause of this wrong behavior, it has been necessary to observe the SPI transactions waveforms via an oscilloscope. The MCP354R[13] datasheet reports the response pattern of the device to a normal command sent via SPI:

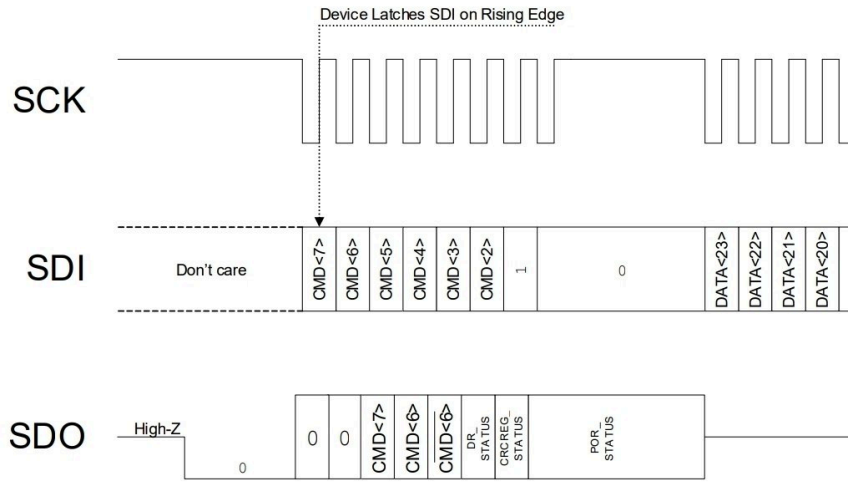


Figure 20: SPI response pattern of the MCP3564R [13].

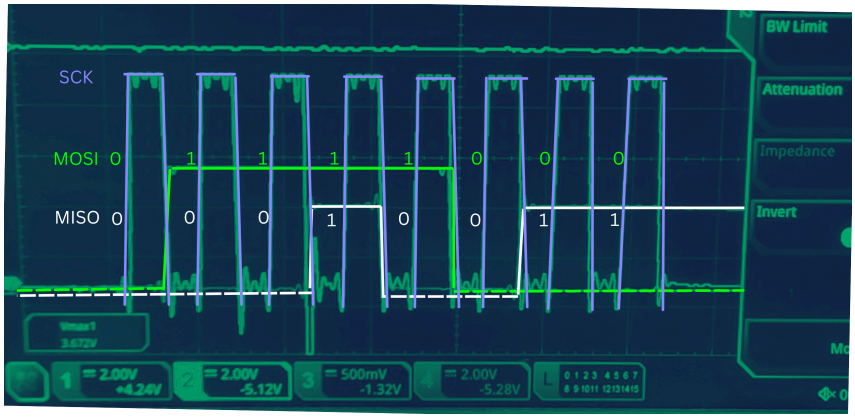


Figure 21: SPI response pattern to a reset command after the fix.

Analyzing the SPI waveforms of the prototype has revealed that the device was not responding to the commands sent by the microcontroller, which was consistent with the ADC codes being zero. Further testing on each configurable register of the MCP3564R revealed that the device was responding only to "fast" commands such as a reset command Figure 21, which do not require the configuration of the device itself for an acquisition. This observation led to the analysis of each of the configuration registers, which revealed the incongruence in the response waveform for the *CONFIG0* register setup: the obsolete firmware was indeed writing 0b **01** 000101, since for the MCP3564 the first two bits were marked as "*don't care*" except for a full-shutdown command (0b 00 000000).

REGISTER 8-2: CONFIG0: CONFIGURATION REGISTER 0

R/W-1	R/W-1	R/W-0	R/W-0	R/W-0	R/W-0	R/W-0	R/W-0
CONFIG0[7:6]		CLK_SEL[1:0]		CS_SEL[1:0]		ADC_MODE[1:0]	
bit 7							bit 0

Legend:			
R = Readable bit	W = Writable bit	U = Unimplemented bit, read as '0'	
-n = Value at POR	'1' = Bit is set	'0' = Bit is cleared	x = Bit is unknown

bit 7-6 **CONFIG0[7:6]**: Full Shutdown Mode Enable
These bits are writable but have no effect except that they force Full Shutdown mode when they are set to '00' and when all other CONFIG0 bits are set to '0'.

bit 5-4 **CLK_SEL[1:0]**: Clock Selection
11 = Internal clock is selected and AMCLK is present on the analog master clock output pin
10 = Internal clock is selected and no clock output is present on the CLK pin
01 = External digital clock
00 = External digital clock (default)

bit 3-2 **CS_SEL[1:0]**: Current Source/Sink Selection Bits for Sensor Bias (source on V_{IN}+/sink on V_{IN}-)
11 = 15 µA is applied to the ADC inputs
10 = 3.7 µA is applied to the ADC inputs
01 = 0.9 µA is applied to the ADC inputs
00 = No current source is applied to the ADC inputs (default)

bit 1-0 **ADC_MODE[1:0]**: ADC Operating Mode Selection
11 = ADC Conversion mode
10 = ADC Standby mode
01 = ADC Shutdown mode
00 = ADC Shutdown mode (default)

Figure 22: *CONFIG0* register bits organization in the MCP3564. [14]

REGISTER 8-2: CONFIG0 REGISTER

R/W-1	R/W-1	R/W-0	R/W-0	R/W-0	R/W-0	R/W-0	R/W-0
VREF_SEL	CONFIG0[6]	CLK_SEL[1:0]		CS_SEL[1:0]		ADC_MODE[1:0]	
bit 7							bit 0

Legend:			
R = Readable bit	W = Writable bit	U = Unimplemented bit, read as '0'	
-n = Value at POR	'1' = Bit is set	'0' = Bit is cleared	x = Bit is unknown

bit 7 **VREF_SEL:** Internal Voltage Reference Bit
1 = Internal voltage reference is selected and buffered internally. REFIN+/OUT pin voltage is set at 2.4V (default).
0 = External Voltage reference is selected and not buffered internally. The internal voltage reference buffer is shut down.

bit 6 **CONFIG0[6]:** If CONFIG0 = 0x0, the device goes into Partial Shutdown mode. This bit does not have any other function.

bit 5-4 **CLK_SEL[1:0]**: Clock Selection
11 = Internal clock is selected and AMCLK is present on the analog master clock output pin.
10 = Internal clock is selected and no clock output is present on the CLK pin.
01 = External digital clock
00 = External digital clock (default)

bit 3-2 **CS_SEL[1:0]**: Current Source/Sink Selection Bits for Sensor Bias (source on V_{IN+}/Sink on V_{IN-})
11 = 15 µA is applied to the ADC inputs
10 = 3.7 µA is applied to the ADC inputs
01 = 0.9 µA is applied to the ADC inputs
00 = No current source is applied to the ADC inputs (default)

bit 1-0 **ADC_MODE[1:0]**: ADC Operating Mode Selection
11 = ADC Conversion mode
10 = ADC Standby mode
01 = ADC Shutdown mode
00 = ADC Shutdown mode (default)

Figure 23: *CONFIG0* register bits organization in the MCP3564R.[13]

For the MCP3564R, the sequence should have been 0b **00** 000000, that corresponds to the selection of the external reference i.e. the *REF2025* that generates the 3.3 V reference voltage for the MCP3564R conversions. Changing the Voltage Reference Selector bit inside *CONFIG0* register finally allowed the MCP3564R to operate as originally intended: the SPI waveforms confirmed the resolution of the issue for the previous component, and the ADC codes were shown in the debugging terminal.

2.3. INA bias resistors

The instrumentation amplifiers required bias resistors to set the correct bias point. The prototype lacked these resistors, which resulted in floating common mode voltage on the input, which quickly saturated to the rails due to the bias currents charging the input capacitances of the amplifiers. This was discovered by noticing that the signal was being acquired only in setups which completed the return path of the bias currents of the amplifiers, for instance connecting one of the electrodes to ground. The study of the datasheet of the amplifiers confirmed the necessity of the bias resistors.

The value of the resistors was chosen to be much bigger than the generator resistance to decrease the loading error. Since the differential source resistance in dry skin conditions is of the order of 10-100kΩ, it was decided to use 8.2MΩ bias resistors, which corresponded to the worst case loading error of 0.6%.

$$\begin{aligned} \varepsilon_V = \frac{V_{\text{source}} - V_{\text{in}}}{V_{\text{source}}} = \\ = \frac{V_{\text{source}}}{V_{\text{source}}} - \frac{V_{\text{source}}}{V_{\text{source}}} \frac{2R_{\text{bias}}}{2R_{\text{bias}} + R_{\text{source}}} = \\ = 1 - \frac{2R_{\text{bias}}}{2R_{\text{bias}} + R_{\text{source}}} = \\ = 0.006 = \\ = 0.6\% \end{aligned} \tag{13}$$

2.4. Routing anomalies

The prototype presented a layout discrepancy that consisted in a trace erroneously connecting a the gain-setting resistor to the output of OPA4330 on both input signal branches. This error was temporarily resolved by severing the trace and installing a jumper wire to restore the intended connection. Later the intended connection was permanently implemented in new PCB designs.

2.5. Other signals acquisition

The PCB featured sensors for capturing other signals relevant to physiological monitoring, such as photoplethysmogram (PPG), temperature and motion data. However, in the subsequent designs only the PPG sensor was retained and moved to a more convenient location, while the remaining sensors were removed.

2.6. Reset pushbutton

It was decided to use the already present pushbutton for a hardware reset of the device.

2.7. RF debugging

Knowing that the antenna can be troublesome and could require debugging to measure transmission power and harmonics, a decision was made to add a second branch after the integrated antenna filter that would be terminated with a uFL connector, allowing for a connection with a VNA or a spectrum analyzer. This insertion has been eventually performed solely on the Master device.

2.8. LED indicators

The prototype already featured an RGB LED communicating the internal state of the device to the user. With the green color being reserved for battery charge indication, the remaining two colors were insufficient, and it was decided to add another RGB LED fully dedicated to the indication of the Bluetooth link status.

Chapter 3

Final Devices Composition

The final iteration of the design yielded two PCBs, one for each device. This chapter overviews features of the Master and Slave PCB designs.

3.1. Master device ("pulsECG")

The design of the Master device retains the general features outlined above and presents some particular features arising from its application as a left wrist-wearable device. These features are discussed in details below.

Its ECG analog front-end functions similarly to the prototype and acquires limb leads using the same three electrodes: the right arm (RA), the left arm (LA) and the left leg (LL). The differential voltages LA-RA and LL-RA are amplified by INA826 and filtered by OPA8330, then sampled by MCP3564R using two differential channels. In addition to the ECG circuitry, the device features a PPG sensor for SpO_2 measurements.

The form factor of the Master device was optimized by placing the components close to each other, which reduced the PCB size.

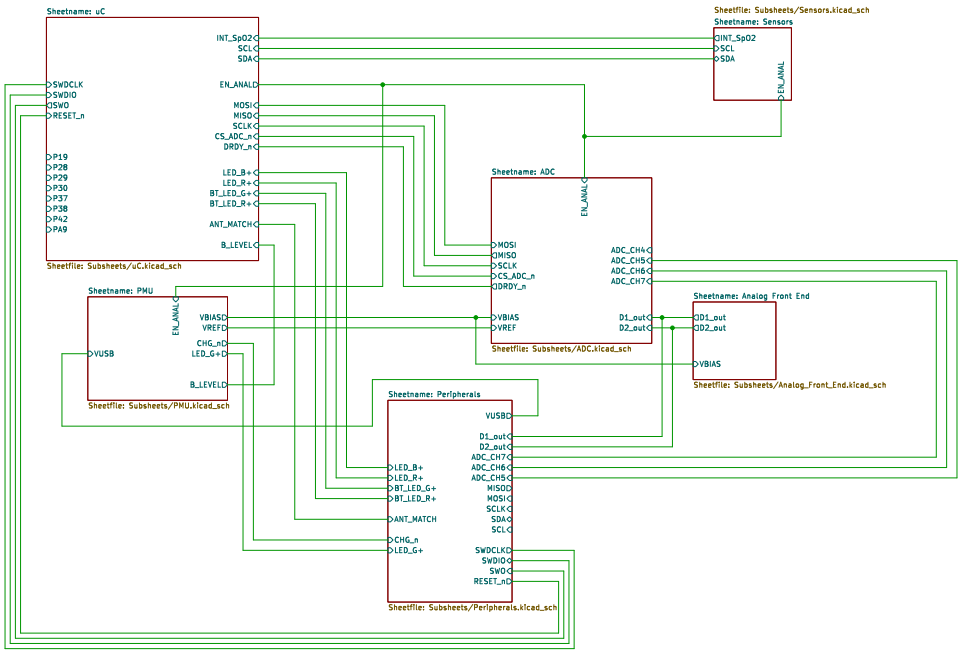


Figure 24: A system-level block diagram of the Master device.

3.1.1 Circuit overview

The subsequent sections explain the hardware architecture and operation of the Master device, following the division into functional blocks implemented within the KiCad schematic. Each major component features are outlined at the end of the relevant section.

Power management

The device is powered by a rechargeable lithium-ion polymer (LiPo) battery with nominal voltage of 3.7V, connected to the system via a two-position SH connector. The charging process from the USB port is managed by a dedicated MAX1555 integrated circuit. The device can be completely shut down by disconnecting the battery from the circuit with a two-position sliding switch SW2. However, the battery remains connected to the MAX1555, which means it can be recharged even when the device is powered off.

Two distinct power domains can be identified: digital and analog, spatially isolated on the PCB to prevent propagation of the noise from high-frequency logic gate switching into the sensitive analog circuitry. The digital domain is supplied by a nominal voltage of $V_{\mathrm{DD}} = 3.3$ V generated by a MAX1759 charge pump.

A firmware-controlled BD2242G power switch can be activated to connect V_{DDA} to the primary power rail V_{DD} and therefore supply the analog circuitry. To minimize quiescent power consumption and conserve energy, the switch is turned off by the microcontroller when the analog front-end and the PPG sensor are not active, which leads to a forced shutdown of all analog parts.

In addition to the V_{DDA} power rail, the analog domain utilizes two precise voltages are generated by REF2025 low-drift voltage reference. In particular, a $V_{\mathrm{REF}} = 2.5$ V is employed by the ADC as a full-scale voltage, and $V_{\mathrm{BIAS}} = 1.25$ V is used as a stable mid-rail reference for the ADC differential channels and for the OPA.

The comprehensive schematic of the power management unit is illustrated in Figure 25.

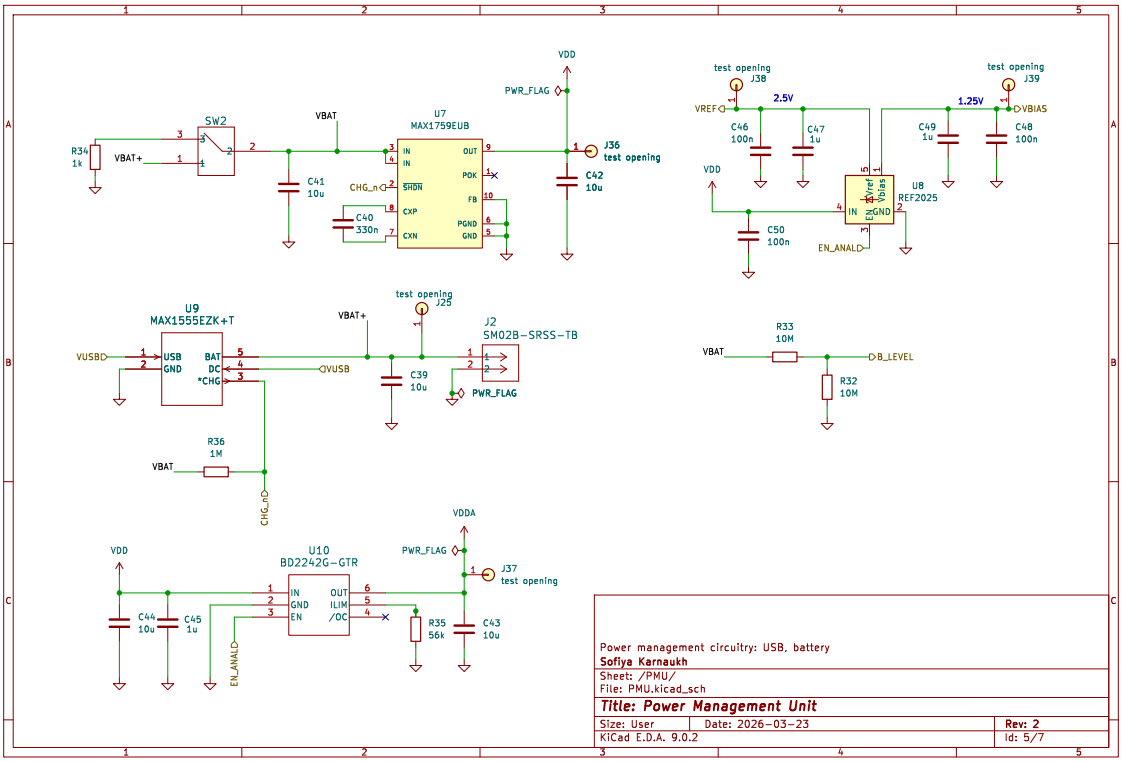


Figure 25: A comprehensive power management unit schematic.

HPL402323-2C

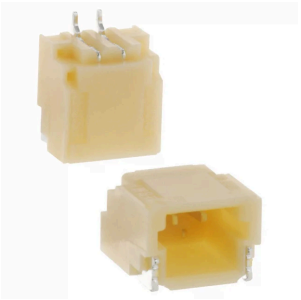
The LiPo battery satisfies strict space constraints of the Master device, at the same time meeting the capacity and peak current demands of the system. It is equipped with a wire terminated by a two-position header and an integrated Protection Circuit Module (PCM) which manages overcharge, over-discharge and short-circuit events.

Table 1: Electrical and physical characteristics of the battery [26]

Feature	**Value**
Nominal operating voltage	3.7 V
Nominal rated capacity	190 mAh
Maximum continuous charge rate	1C
Maximum continuous discharge rate	2C
Physical dimensions	4.0 mm x 23 mm x 23 mm



(a) HPL402323-2C LiPo cell



(b) SM02B-SRSS-TB battery connector [45]

Figure 26: Photos of the battery and the matching connector.

MAX1555EZK+T

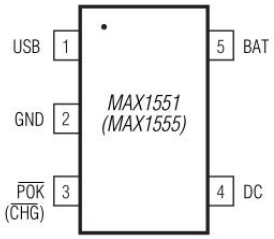
The MAX1555EZK+T manages charging process of a single-cell lithium-ion battery from USB or AC adapter sources with voltage ranging from 3.7 V to 6 V. A deeply depleted cell will be initially charged in prequalification or trickle charging (TC) mode until the voltage reaches a threshold value, after which the chip enters constant current (CC) mode until the regulation voltage of 4.2 V is reached. At the end of the charging process, the device enters costant voltage (CV) mode to maintain the voltage level and lets the current decrease exponentially.

Table 2: Electrical and physical characteristics of the charger [27]

Feature	**Value**
Package	SOT23-5
Prequalification threshold and current	3 V / 40 mA
Maximum DC charging current	340 mA
Minimum battery regulation voltage	4.141 V



(a) MAX1555EZK+T package [46]



(b) MAX1555EZK+T pinout

Figure 27: MAX1555EZK

SLW-66527511-SMT-TR

The SLW-66527511-SMT-TR two-position sliding switch in Figure 28 was selected due to its small form factor and surface mount technology, which eliminates through-hole pin protrusions on the back side of the device that would be observed with a through-hole component.



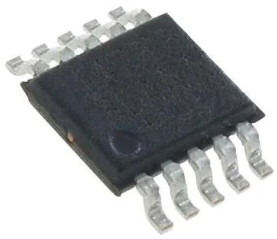
Figure 28: SLW-66527511-SMT-TR sliding switch [15]

MAX1759EUB

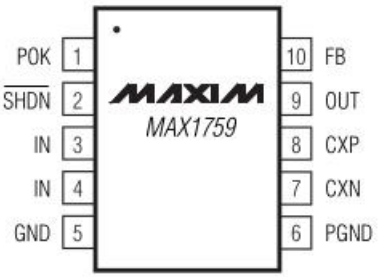
The MAX1759EUB is a charge pump that generates an adjustable regulated voltage from a 1.6–5.5 V input. Contrary to classical buck-boost switching converters, this architecture requires only three external capacitors, in particular the charge pump capacitor C_x and decoupling capacitors C_{in} and C_{out}.

Table 3: Electrical and physical characteristics of the voltage regulator [28]

Feature	**Value**
Package	10-pin µMAX
Topology	Charge pump
Quiescent current	50–100 µA
Input voltage range	1.6–5.5 V
Output voltage adjustment range	2.5–5.5 V
Maximum output current	100 mA



(a) MAX1759EUB package [47]



(b) MAX1759EUB pinout

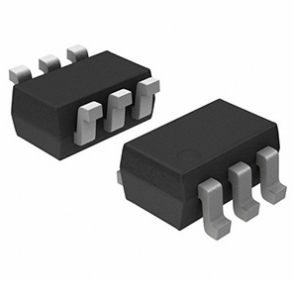
Figure 29: MAX1759EUB

BD2242G-GTR

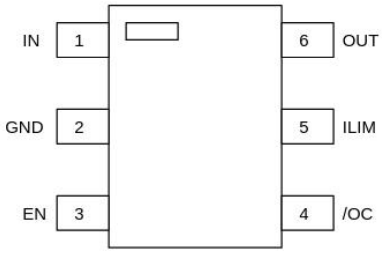
This integrated circuit is an N-channel MOSFET high-side power switch controlled by active high enable signal, which in the current application is driven by a microcontroller. It features an overcurrent protection mechanism, with the current threshold being adjustable by a resistor. In the present application the threshold was set to 374.8 mA by a 56 kΩ resistor.

Table 4: Electrical and physical characteristics of the power switch [29]

Feature	**Value**
Package	SSOP6
Input voltage range	2.8–3.5 V
Current limit adjustable threshold	212-1696 mA
Maximum standby current	5 µA
On resistance	89 mΩ



(a) BD2242G package



(b) BD2242G pinout

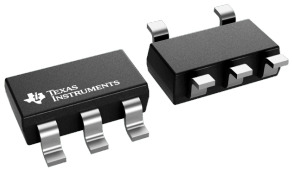
Figure 30: BD2242G-GTR

REF2025AISDDCR

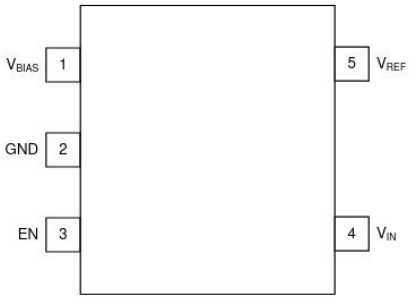
REF2025 is a low-power, low drift, high accuracy voltage reference with two outputs, V_{REF} and $V_{\text{BIAS}} = \frac{1}{2}V_{\text{REF}}$.

Table 5: Electrical and physical characteristics of the voltage reference [30]

Feature	**Value**
Package	SOT23-5
Topology	Bandgap voltage reference
Quiescent current	360 µA
Input voltage range	2.5–5.5 V
Primary voltage output	2.5 V
Secondary voltage output	1.25 V
Temperature drift	8 ppm/°C
Initial accuracy	0.05%
Maximum output current	±20 mA



(a) REF2025AISDDCR package [48]



(b) REF2025AISDDCR pinout

Figure 31: REF2025AISDDCR

Analog Front-End

The schematic of the conditioning circuitry of the two ECG leads is reported in Figure 32. The ECG signal is trasmitted through copper electrodes to the instrumentation amplifiers INA826AIDR, then filtered and amplified by OPA4330AIDR.

The inputs of the first INA826 were inverted with respect to the prototype for topological reasons. In particular, to allow for size reduction, the LA and RA electrodes needed to be placed in the center of the board, and the trace connecting the LA electrode to the INA would inevitably intersect one of the two traces connecting RA to both INAs. By swapping the inputs of the first INA, it became possible to avoid such intersection and hence optimize the routing. The inversion was compensated later in the digital domain by multiplying the first-channel readings by -1.

The LL electrode was moved off-board and connected to the board via a flat cable to facilitate its positioning on the left leg during the ECG measurement. The flat cable is depicted in Figure 32 as a rectangle.

Finally, the bias resistors are added to the INA inputs to stabilize the operating point of the amplifiers.

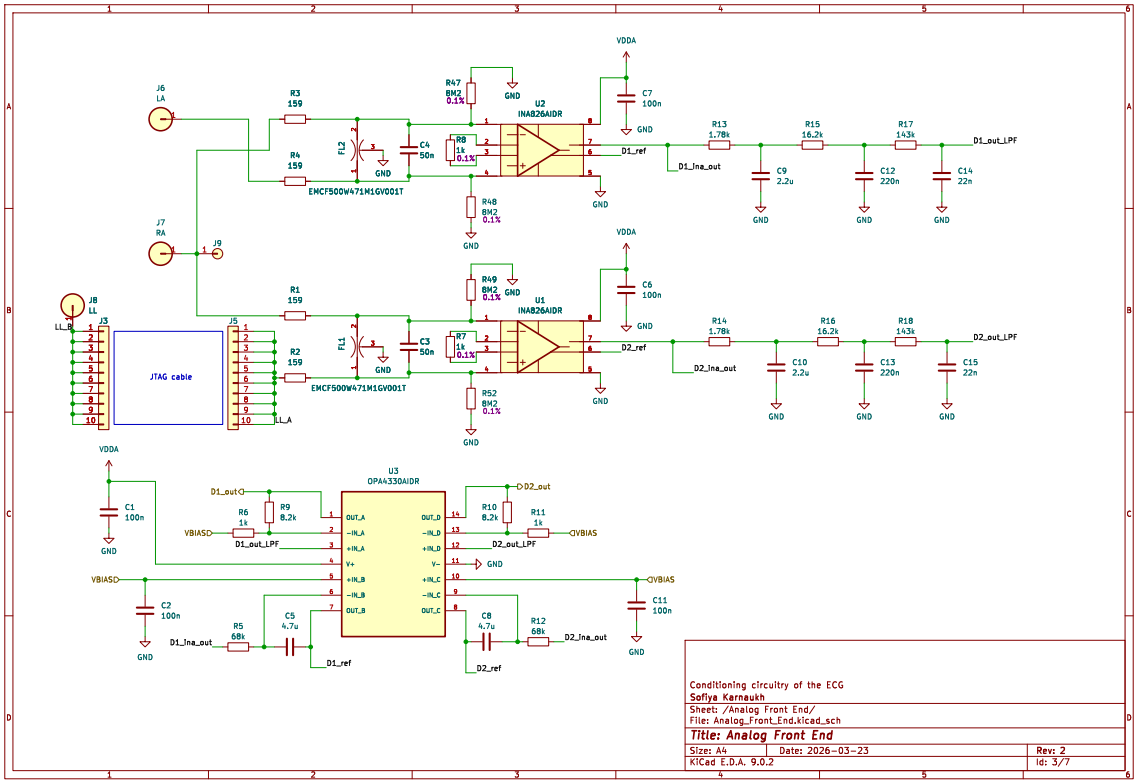
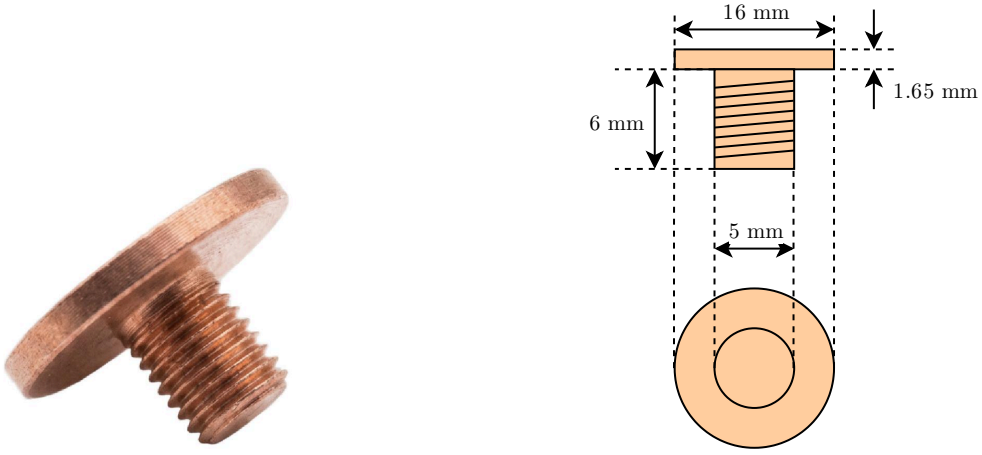


Figure 32: Analog front-end schematic.

Electrodes

Copper electrodes were used in the present design to replicate the validated performance of the original prototype.



(a) Side view (b) Physical dimensions

Figure 33: Copper electrode

331171302030

The 331171302030 is a gold plated spring finger connector used to ensure flexible connection between the RA electrode and the PCB. The need in such a connection arose from the destructive effects of the RA electrode being soldered directly to a pad on the PCB: due to the tangential component of the force applied by finger during acquisition, the pad often detached from the FR4 substrate after some weeks of use.

The spring connector partially transforms the tangential force component into the shear force applied to the string.

The gold on the contact ensures negligible contact resistance between the electrode and the connector.



(a) 331171302030 [49] (b) FFSD-05-D-06.00-01-N (c) FTSH-105-01-F-DV-K-P-TR [50]

Figure 34: Connectors for electrodes

FFSD-05-D-06.00-01-N and FTSH-105-01-F-DV-K-P-TR

The FFSD-05-D-06.00-01-N is a ribbon cable interconnecting the LL and the board. This type of cable was preferred over to a flat flexible cable (FFC), as the latter is more be prone to damages after continuous use involving regular cable bending.

Two SMD headers FTSH-105-01-F-DV-K-P-TR are used along with the cable, one of them being soldered directly to the electrode. Gold contact finish of both the cable and the connectors helps to reduce contact resistance.

Table 6: Electrical and physical characteristics of the connector and the associated mating cable [31], [32]

Feature	**Value**
Mounting	SMD
Number of positions	10
Number of rows	2
Pitch	1.27 mm
Contact finish	Gold

INA826AIDR

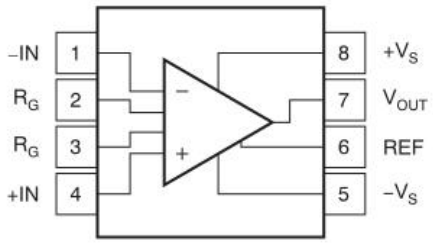
The INA826AIDR is an instrumentation amplifier chosen for its low power consumption, excellent common-mode rejection ratio and presence of two differential channels.

Table 7: Electrical and physical characteristics of the INA [33]

Feature	**Value**
Package	SOIC
Quiescent current	200 µA
Supply voltage	36 V
Gain adjustable range	1-1000 V/V
Power supply rejection ratio	130 dB at G = 10
Common mode rejection ratio	104 dB at G = 10
Input offset voltage	150 µV (max.)
Input impedance	100 kΩ
Input bias current	35 nA (typ.)
Slew rate	1 V/μs
Bandwidth	1 MHz at $G = 1$; 60 kHz at $G = 100$
Input voltage noise density	8 nV/$\sqrt{\text{Hz}}$ at $G \geq 100$ at $f = 1$ kHz



(a) INA826AIDR package



(b) INA826AIDR pinout

Figure 35: INA826AIDR

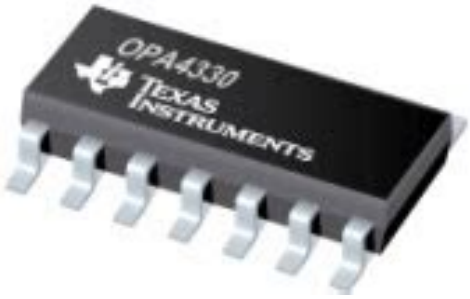
OPA4330AIDR

The OPA4330AIDR is composed of four CMOS operation amplifiers (op-amps) that offer zero drift, low offset voltage, rail-to-rail input and output while maintaining acceptably low power consumption.

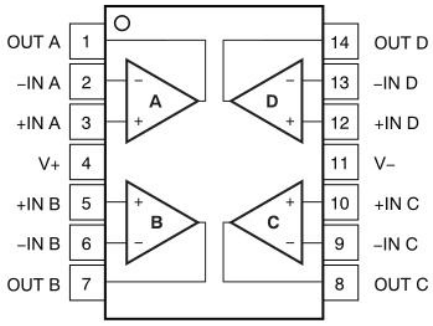
Two of the op-amps constitute servo loops for the INAs to reduce low-frequency wandering. The other two are used to amplify the low-pass-filtered ECG signals.

Table 8: Electrical and physical characteristics of OPA4330AIDR [34]

Feature	**Value**
Package	SOIC
Topology	Zero-drift chopper op-amp
Quiescent current	140 µA (max.)
Supply voltage	1.8–5.5 V
Input and output voltage range	Rail-to-rail
Open-loop voltage gain	115 dB (typ.)
Common mode rejection ratio	115 dB (typ.)
Input offset voltage	50 µV (max.)
Input bias current	70 pA (typ.)
Input voltage noise	1.1 μV_{pp}



(a) OPA4330AIDR package [51]



(b) OPA4330AIDR pinout

Figure 36: OPA4330AIDR

ADC

The conditioned ECG signals are sampled differentially by an MCP3564R analog-to-digital converter (ADC), using V_{BIAS} as the mid-rail reference voltage. Figure 37 reports the schematic illustrating the interconnection of the MCP3564R and the related auxiliary components. One of the such components is the 625L3I008M00000 crystal used by the ADC as a master clock signal.

The sampling rate of the ADC is governed by the selected conversion mode, which can be configured as either one-shot mode or continuous mode. For both modes, the SCAN option can be enabled. This option allows the ADC to cycle autonomously between the channels selected in the internal `SCAN` register. Since the design of the Master device requires periodic sampling of two separate channels for two-lead ECG acquisition, the continuous conversion mode with SCAN option was chosen. Based on these design requirements, all modes are compared in Table 9.

Table 9: Comparison of various sampling modes of the MCP3564R

Mode	Minimal time between conversions	Microcontroller code penalty
One-shot No scan	T_{conv}	High: microcontroller must manage timing and channel selection via `MUX` register
Continuous No scan	1 / DRCLK (fully pipelined)	Low: timing is managed by the ADC, but it can only sample from the same channel
One-shot Scan	T_{conv}	Medium: microcontroller manages timing
Continuous Scan	T_{conv}	Low: the ADC manages both timing and channel rotation

For the selected conversion mode, the sampling rate can be calculated as follows, using Equation 4-2 and Equation 5-4 from the datasheet [35]:

$$\begin{aligned} f_{\text{S}} &= \frac{1}{T_{\text{CONV}}} \\ &= \frac{\text{DMCLK}}{3\text{OSR}_3 + \text{OSR}_3(\text{OSR}_1 - 1)} \\ &= \frac{\text{MCLK}}{4 \text{ Prescale } (3\text{OSR}_3 + \text{OSR}_3(\text{OSR}_1 - 1))} \\ &= 8\frac{\text{Mhz}}{4 * 1 * (3 * 512 + 512 * (8 - 1))} \\ &= 390 \text{ Sa}/s \end{aligned} \tag{14}$$

where MCLK is the master clock frequency, OSR is the oversampling ratio stored in the CONFIG1 register, and Prescale is a programmable prescale coefficient from the same configuration register, which allows for a reduction of the sampling rate to suit specific application needs. The OSR values were taken from Table 5-6 of the datasheet [35]. It was also decided to not program delays between conversions and conversion cycles.

Due to two channels being sampled, the sampling rate per channel becomes:

$$f_{\text{S, channel}} = 195 \text{ Sa}/s \tag{15}$$

The samples are transmitted to the microcontroller over SPI. All lines comprising the SPI interface are terminated at the driver side with 100 Ω resistors to suppress ringing. Even though the current trace lengths are reduced in magnitude with respect to the prototype, the possibility to stabilize the SPI interface with the resistors was preserved intentionally.

Since the thermopile was omitted from the present design with respect to the prototype, the corresponding ADC inputs were left unconnected.

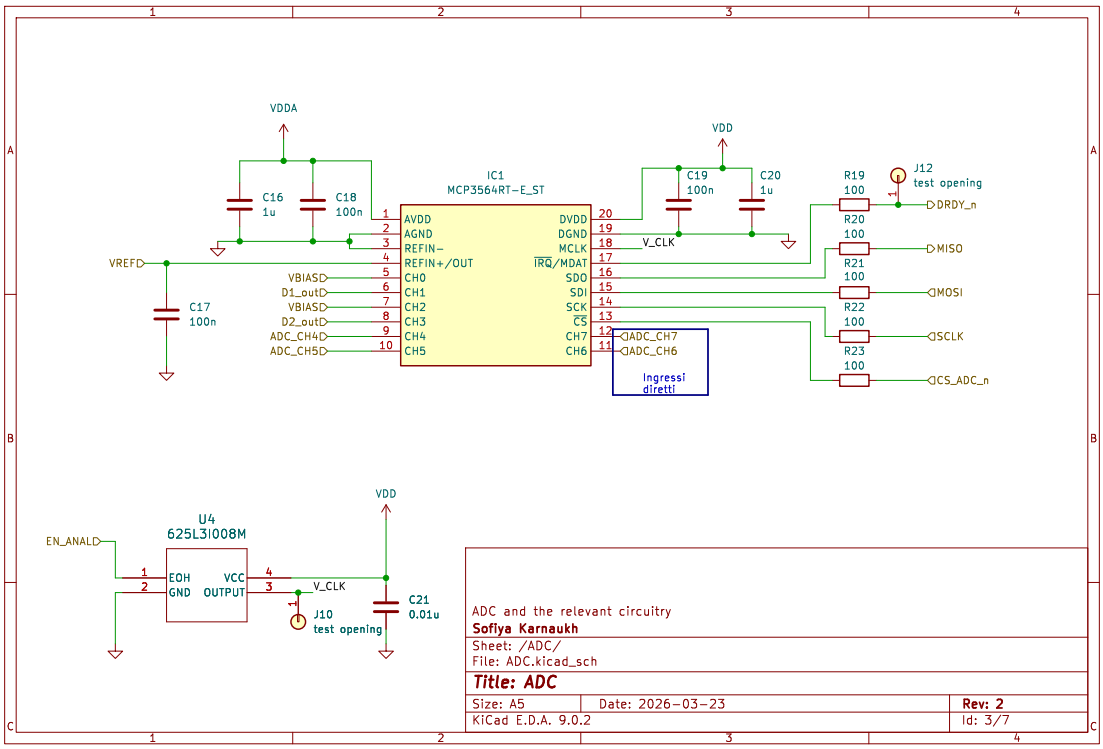


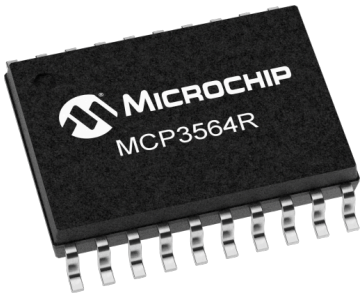
Figure 37: A schematic of the ADC and the related circuitry.

MCP3564RT-E/ST

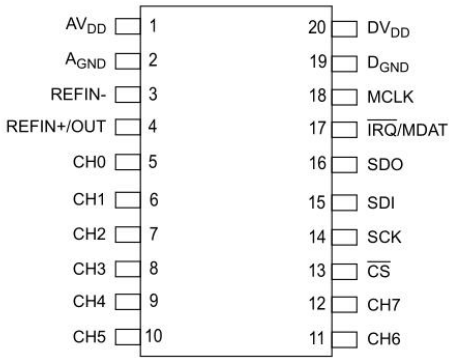
The MCP3564RT-E/ST is a low-noise, low-drift delta-sigma ADC operating on four input channels and producing 24-bit output. The analog and digital domains are powered on separately. The sampling parameters, such as data rate, oversampling ratio, and gain, can be customized programmatically.

Table 10: Electrical and physical characteristics of the ADC [35]

Feature	**Value**
Package	20-lead TSSOP
Topology	Sigma-delta
Digital interface	SPI
Current consumption	2.4 µA (max., full shutdown); 2.6 mA (max., operating)
AV_{DD} supply voltage	2.7–3.6 V
DV_{DD} supply voltage	1.8 V – $AV_{DD} + 0.1V$
Reference voltage range	0.6 V – AV_{DD}
Master clock frequency range	1–20 MHz
Programmable gain values	0.33x, 1x, 2x, 4x, 8x, 16x
RMS Effective Resolution	21.1 bits (Gain = 1, OSR = 4096)
Input-referred voltage noise	2.98 µVrms (Gain = 1, OSR = 4096)
Offset error and drift	0.85 µV, 16 nV/°C (max., Gain = 1)
Gain error and drift	3%, 2 ppm/°C (max., Gain = 1)
INL	7 ppm FSR (max., Gain = 1)
PSRR	110 dB (typ.)
CMRR	126 dB (typ.)



(a) MCP3564RT-E/ST package [52]



(b) MCP3564RT-E/ST pinout, top view (pads down)

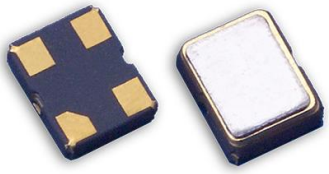
Figure 38: MCP3564RT-E/ST

625L3I008M00000

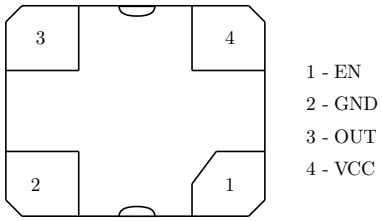
The 625L3I008M00000 low-voltage oscillator provides a frequency conformal with the accepted frequencies range from the MCP3564 specifications with ±50 ppm stability. Since its current consumption may arrive to 15 mA, the device features an Enable input to be able to be turned off when the ADC is not in use.

Table 11: Electrical and physical characteristics of the ADC oscillator [36]

Feature	**Value**
Package	20-lead TSSOP
Topology	Sigma-delta
Current consumption	15 mA (max.)
Supply voltage	2.97–3.63 V
Frequency	8 MHz
Frequency stability	±50 ppm



(a) 625L3I008M00000 package



(b) 625L3I008M00000 pinout, bottom view (pads up)

Figure 39: 625L3I008M00000

SpO_2 acquisition system

SpO_2 is measured by the with a complex system encompassing hardware, firmware, and software parts. The hardware aspect is discussed in the present section, the firmware will be seen in details in Chapter 4.5.3, and the software side is explained in Chapter 5.5.3.

The raw digital SpO_2 signal is acquired with a sensor. The data is read from the sensor by the microcontroller via an I²C interface and then sent in packets via Bluetooth to the end device. The elaboration of the data is performed on the user device for its computational power being superior to a microcontroller. The schematic of the acquisition system is represented in Figure 40.

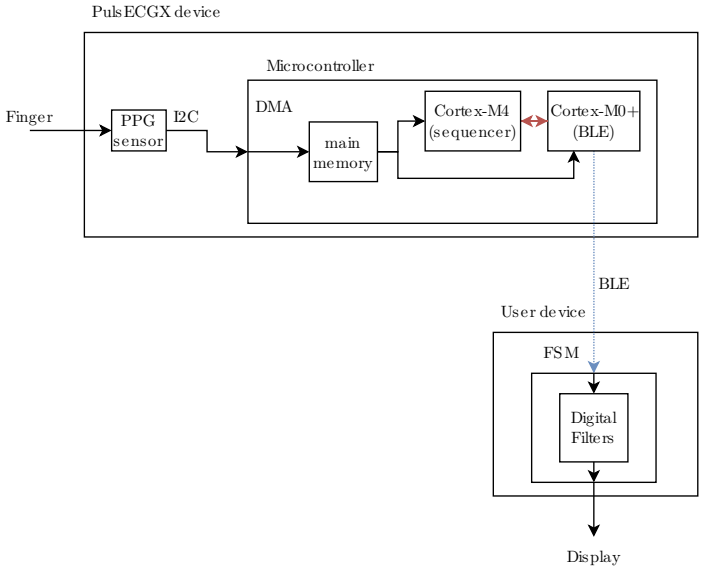


Figure 40: PPG acquisition system diagram. The BLE link is depicted with a blue dotted arrow. The communication between the microcontroller cores is depicted as a double-ended red arrow.

The chosen sensor is MAXM86161. It is a compact low power device, comprising a completely integrated optical acquisition system, namely the LEDs and a photodiode, an analog conditioning circuitry, an ADC and digital pre-processing algorithms: ambient light cancellation (ALC) circuit and picket fence detect and replace algorithm [53].

The component is compatible with the supply voltage of the device. Its communication with the microcontroller is implemented with I²C interface and an interrupt pin `INT_SpO2`. The complete schematic of the sensor and the related passive components is reported in Figure 41.

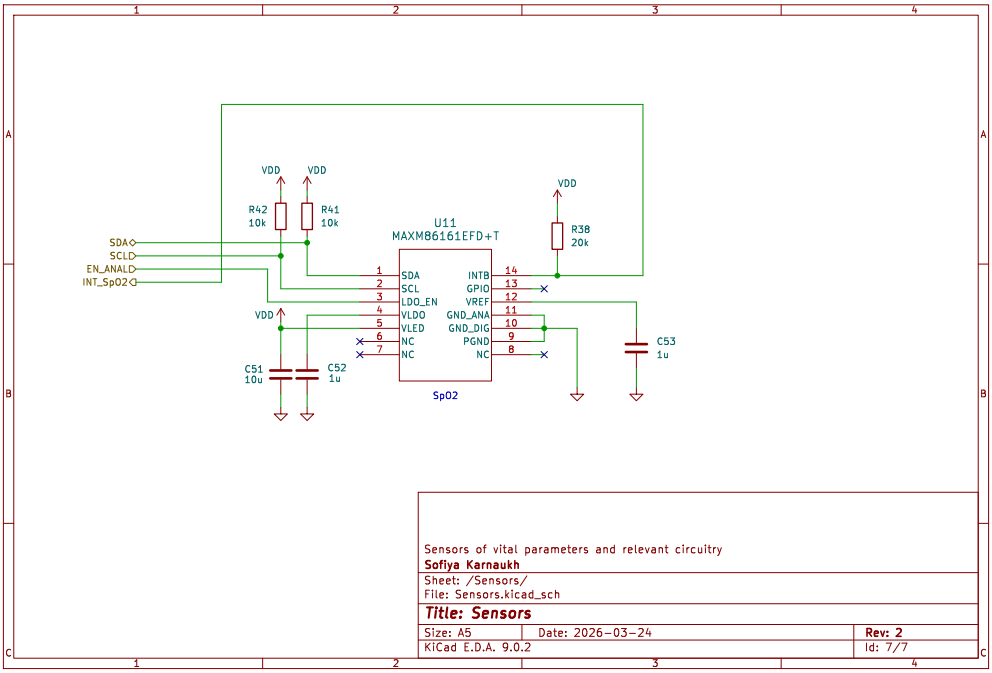


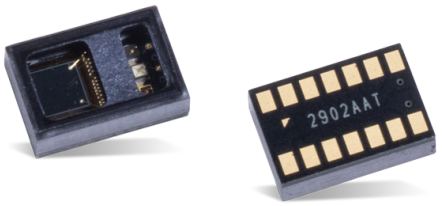
Figure 41: A schematic of the PPG sensor and the related auxiliary components.

MAXM86161EFD+T

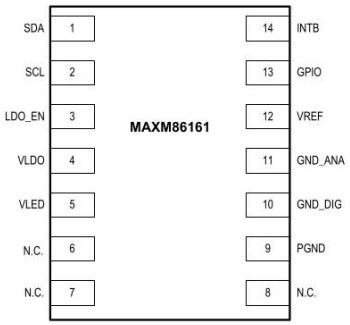
The sensor has a fully integrated optical system, which simplifies its use, as the LED driving and timing is performed by the sensor itself.

Table 12: Electrical and physical characteristics of the PPG sensor [37]

Feature	**Value**
Package	14-pin OLGA
Operating current	15 mA (max.)
Supply voltage	2.97–3.63 V
λ_{RED}	660 nm
λ_{IR}	880 nm



(a) MAXM86161EFD+T package [54]



(b) MAXM86161EFD+T pinout, top view (pads down)

Figure 42: MAXM86161EFD+T

Peripherals

The PCB integrates several peripherals. The user interface comprises the Reset tactile switch EVQ-PUJ02K, which allows for a manual reboot of the device, and two light-emitting diodes (LEDs) EAST1616RGBA8, which visually convey the internal state of the device to the user. All currently implemented LED configurations are reported below.

Table 13: All possible LED configurations of the Master device and their meaning.

LED configuration	Meaning
Green LED blinks once	The device has initiated a connection to the user device via BLE.
Blue LED is on	The device is actively transmitting ECG data over BLE to the user device.
Blue LED and red LED blink once simultaneously	The device is turning on.
Red LED is on	The PPG sensor data queue is full, the microcontroller cannot keep up with reading data.

The legacy male pin headers providing access to major signals served solely for the debugging of the prototype and were hence omitted from the present design. They were replaced with a single ten-position surface mount (SMD) micro-header dedicated exclusively to microcontroller programming. It was decided to employ an SMD connector to prevent pins from protruding through the back side of the board, which is reserved for the PPG sensor and the LL electrode only and is supposed to stay close to the PCB enclosure.

Another important peripheral is the 2.4 GHz meander antenna designed following the recommendations provided by the STMicroelectronics [55]. It is accompanied by an integrated passive low-pass filter MLPF-WB55-01E3 matching the microcontroller's power amplifier to 50 Ω, a jumper to select the output between the antenna and the microscopic coaxial connector for spectrum analyzer, and one antenna matching network to adapt the 50 Ω to a complex conjugate of the antenna impedance, which at 2.4 GHz is approximately equal to 38.3 + j 3.6 Ω [55]. The implemented architecture follows the one proposed by an application note [56].

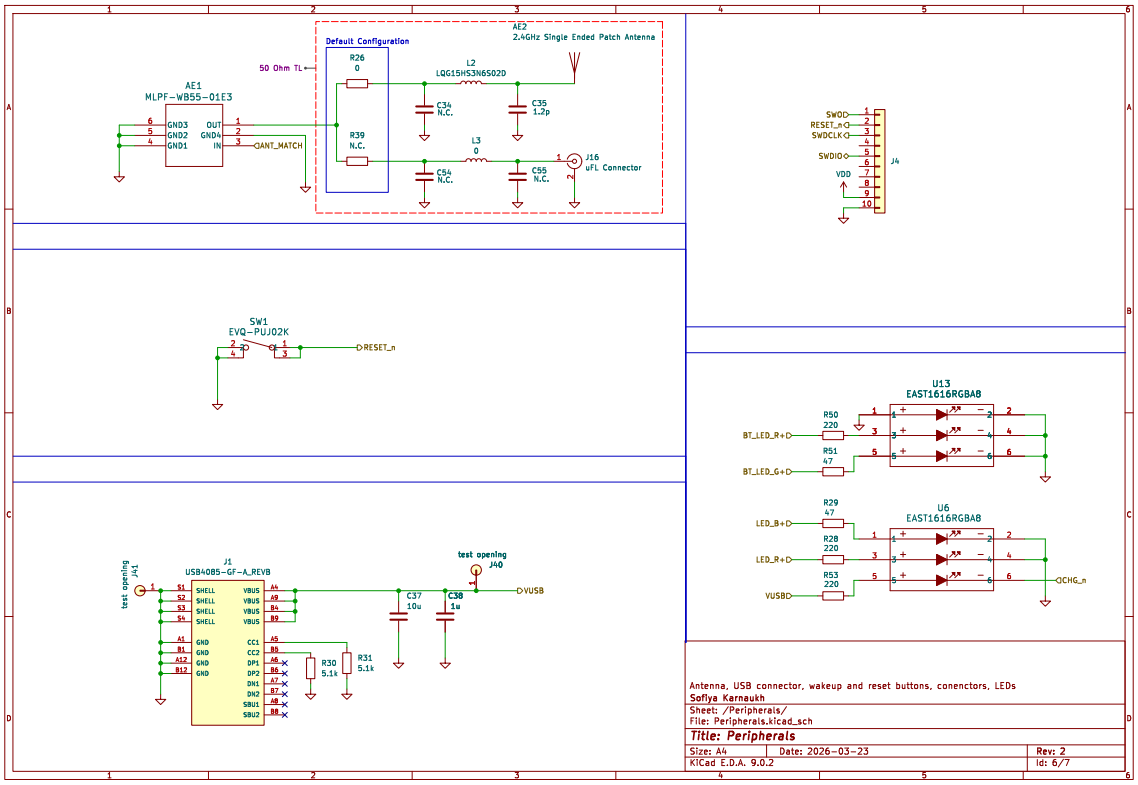


Figure 43: The Master device eripherals.

MLPF-WB55-01E3

The device is an integrated low-pass filter with proprietary architecture.

Table 14: Electrical and physical characteristics of the integrated filter [38]

Feature	**Value**
Package	Bumpless Chip Scale Package
Input impedance	Matched to the microcontroller
Output impedance	50 Ω



(a) Package (b) Pinout, top view (pads down)

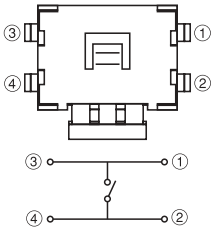
Figure 44: MLPF-WB55-01E3

EVQ-PUJ02K

This single-pole, single-throw tactile switch is used due to its small outline and SMD mounting technology. The horizontal position makes it accessible from the side of the device.



(a) Package [57]



(b) Pinout and circuit diagram, top view (pads down)

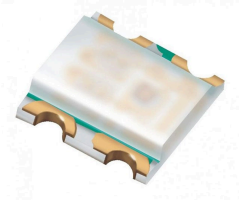
Figure 45: EVQ-PUJ02K

EAST1616RGBA8

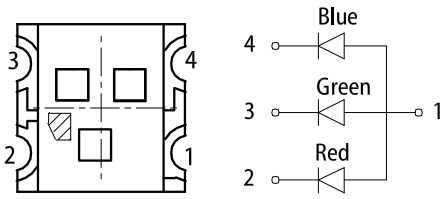
The EAST1616RGBA8 is a full-color LED, with each of three components being individually driven from a dedicated cathode pair of pins.

Table 15: Electrical and physical characteristics of the RGB LED [39]

Feature	**Value**
Package	6-pin SMD-B package
Dominant wavelengths (typ.) at $I_F = 20$ mA	621 nm (red), 525 nm (green), 465 nm (blue)
Forward voltages (typ.) at $I_F = 20$ mA	2 V (red), 3.3 V (green), 3.3 V (blue)



(a) Package



(b) Pinout and circuit diagram, top view (pads down)

Figure 46: EAST1616RGBA8

USB4085-GF-A

This part is a standard 24-pin USB-C female connector with top-mount through-hole mounting style.

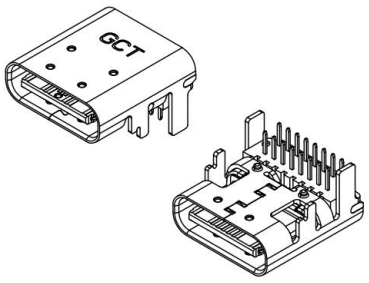


Figure 47: USB4085-GF-A package [16]

STM32WB30CEU5A

The microcontroller STM32WB30 is an ultra-low-power device that embeds two processors: an Arm Cortex-M0+ dedicated to a real-time low-level management of the radio interface, including advertising, connection events, and payload dispatch, and an Arm Cortex-M4, which is employed for the user application code and peripherals management. They communicate via an Inter-Processor Communication Channel (IPCC) and share a subsection of SRAM2 to exchange data. A simplified block diagram of the microcontroller is reported in Figure 48.

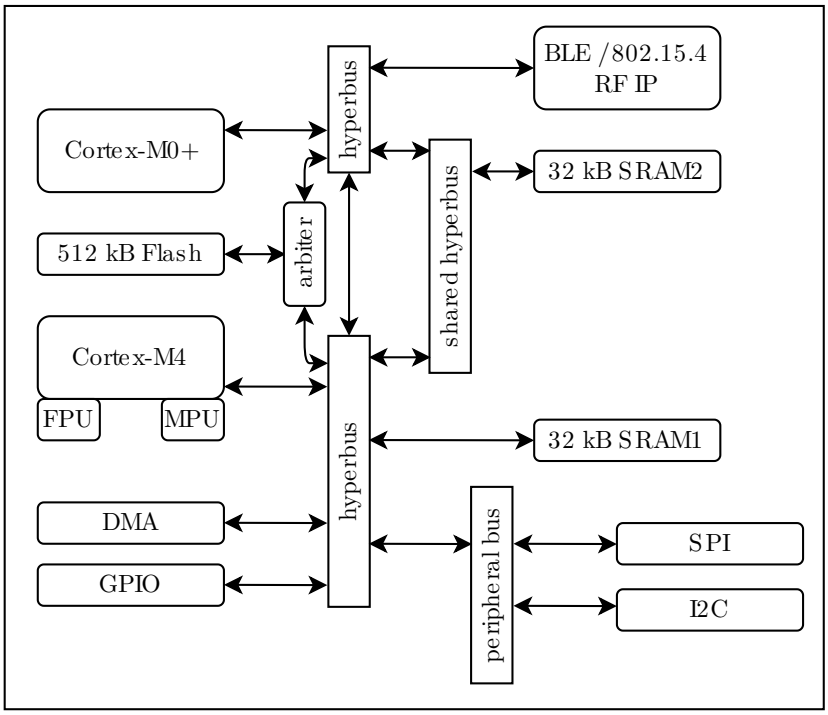


Figure 48: STM32WB30 microcontroller simplified architecture [17].

Two distinct processors operate at different frequencies, which creates need in two different oscillators to provide clock to the cores. In the present design, the RF core is clocked by a high-speed external (HSE) 32 MHz crystal, whereas the real time clock (RTC) of the user application core is supplied by a low-speed external (LSE) 32.768 kHz crystal, as indicated by the datasheet of the device.

The microcontroller peripherals were already introduced in Peripherals section, whereas the SPI and the I2C interfaces are discussed in detail in Chapter 4.3.1.

To program the present device, an ST-LINK from an STM32 Nucleo board was used. The programming is performed via a Serial Wire Debug (SWD) interface comprising three main signals: Serial Wire Data Input/Output (SWDIO), Serial Wire Clock (SWCLK), and Active-Low Reset (NRST). The programming requires the grounds of the target and the programmer to be interconnected. Additionally, the V_{DD} of the programmer can be used to power the Master device when the battery is not connected. These signals and voltages are supplied to the microcontroller via a flat cable paired to a micro-connector. Since the STM32 Nucleo board used for the programming featured standard-sized headers, a hybrid micro-to-standard flat cable was created for the programming purpose specifically.

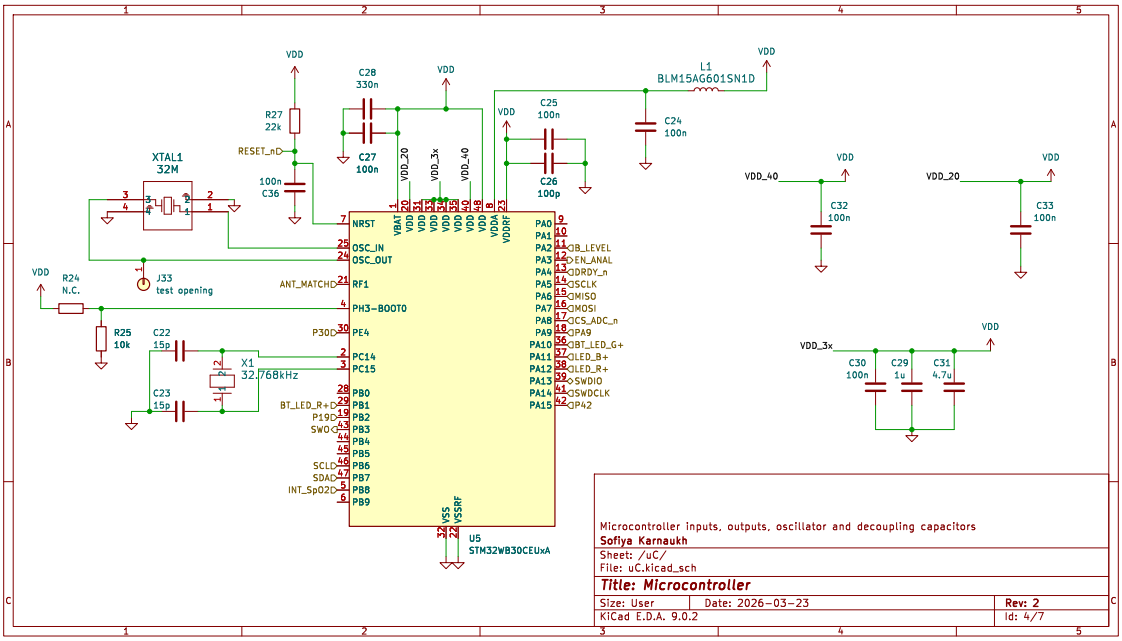


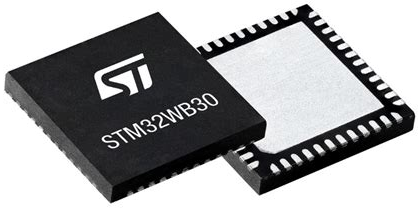
Figure 49: The microcontroller schematic.

Programming toolchain includes:

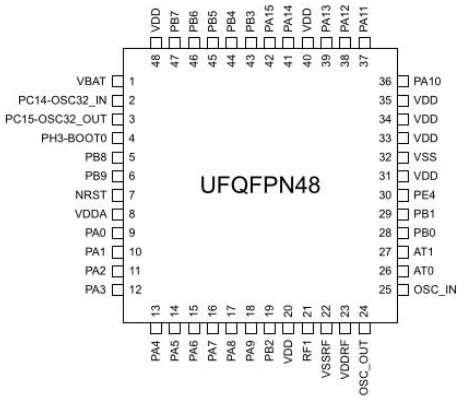
- ARM GCC compiler and associated tools;
- STM32CubeProgrammer / OpenOCD with ST-Link support for debugging;
- STM32CubeIDE for code editing;
- STM32CubeMX for code generation.

Table 16: Electrical and physical characteristics of the microcontroller

Feature	**Value**
Package	48-lead UFQFPN with exposed pad
Supply voltage	2.0-3.6 V
Current consumption	14 nA (shutdown mode)
CPU cores	Arm Cortex-M0+ (RF domain), Arm Cortex-M4 (RTC)
Flash memory	512 kB
SRAM	96 kB split in 3 blocks
GPIO count	30 pins
Communication peripherals	12-bit ADC, SPI, I²C, USART
Wireless interface	BLE 5.4 transceiver, Zigbee, Thread
DMA capabilities	1 controller, 7 channels
Clock sources	Internal RC oscillators, 32 MHz HSE crystal, 32.768 kHz LSE crystal



(a) Package [58]

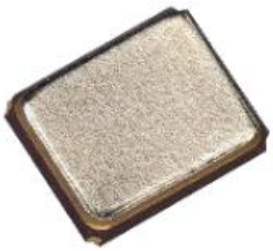


(b) Pinout, top view (pads down)

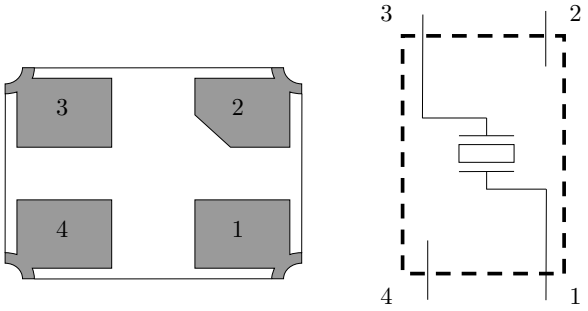
Figure 50: STM32WB30CEU5A

FA-128 32.0000MF10Z-AJ3

This high-quality quartz crystal resonator produces a fundamental tone at 32 MHz and comes in a 4-pad SMD package and is optimized for radio applications, featuring 8 pF load capacitance required by STM32WB30 (Table 48 of the datasheet) and a tight ±10 ppm tolerance.



(a) Package, top view [59]



(b) Pinout, top view (pads down)

Figure 51: FA-128 32.0000MF10Z-AJ3

CM8V-T1A-32.768kHz-9pF-20PPM-TB-QC

This device is a low-frequency quartz crystal with 9 pF load capacitance and ±20 ppm tolerance. Assuming the UFQFPN48 package has low stray capacitance of 2 pF associated with the LSE pins, and that the parasitic capacitance of traces to ground is negligible, it was established that 15 pF external capacitors need to be used in order for the crystal to see the target load capacitance:

$$\begin{aligned} C_L &= (C_{\mathrm{L1}} \parallel C_{\mathrm{L2}}) + C_{\mathrm{stray}} \\ C_{\mathrm{L1}} = C_{\mathrm{L2}} &= 2 \times \left(C_L - C_{\mathrm{stray}}\right) = 2 \times (9\ \mathrm{pF} - 2\ \mathrm{pF}) = 14\ \mathrm{pF} \approx 15\ \mathrm{pF} \end{aligned} \tag{16}$$



Figure 52: The CM8V-T1A-32.768kHz-9pF-20PPM-TB-QC package, top and bottom view [18]

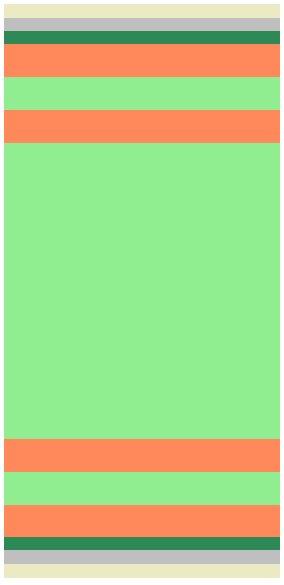
3.1.2 Board overview

The following sections report the board configuration, the enclosure and the assembly process description.

Board configuration

The Master device was implemented on four-layer FR-4 PCB with 1 Oz copper weight. The full layer stackup is reported in Table 17 and features Front, Internal 1, Internal 2 and Back copper layers. Most components are placed on the front layer, except for the LA electrode and PPG sensor, which are positioned on the back layer to interface directly with the user's left wrist. The internal In1 and In2 layers serve primarily as ground planes, providing return paths for signals routed on the respective adjacent surface layers.

Table 17: Master device PCB stackup: table and cross-section schematic (not to scale)

Layer	Material	Thickness	ε_R	Cross-section
F.Silkscreen				
F.Paste				
F.Mask		0.01 mm	3.3	
F.Cu	Copper	0.035 mm		
Dielectric 1	PrePreg FR4	0.2104 mm	4.5	
In1.Cu	Copper	0.0152 mm		
Dielectric 2	Core FR4	1.065 mm	4.5	
In2.Cu	Copper	0.0152 mm		
Dielectric 3	PrePreg FR4	0.2104 mm	4.5	
B.Cu	Copper	0.035 mm		
B.Mask		0.01 mm	3.3	
B.Paste				
B.Silkscreen				

The PCB was ordered for fabrication with the specifications reported in Table 18. Another order was placed for the corresponding solder stencil fabrication, according to the parameters indicated in Table 19.

Table 18: Master device PCB order parameters

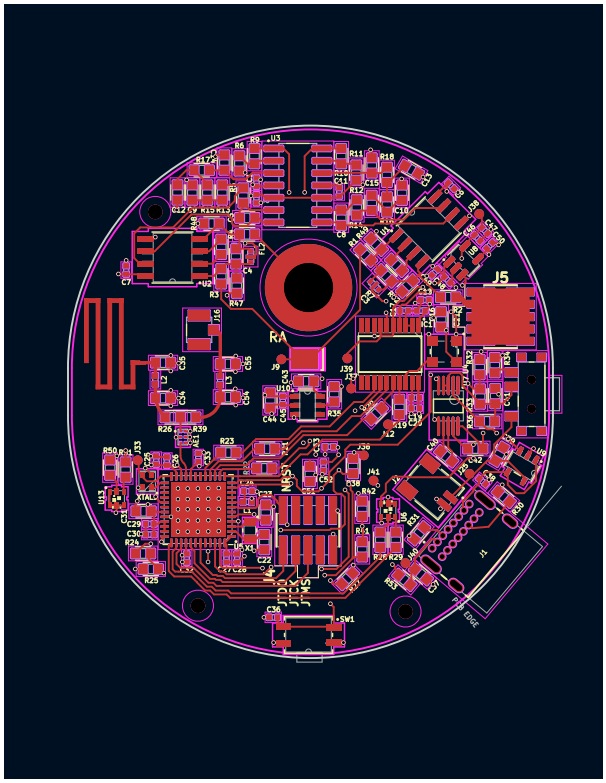
Parameter	Value	Parameter	Value
Dimensions	50 mm ∗ 54.9 mm	Electrical test	Flying probe fully test
PCB quantity	5	Castellated holes	No
Product type	Industrial/Consumer electronics	Press-fit hole	No
		Edge plating	No
Different design	1	Mark on PCB	No
Delivery format	Single PCB	Blind slot	No
PCB thickness	1.6 mm	Minimal via hole size/ diameter	0.3mm/(0.4/0.45mm)
Impedance control	No requirement		
PCB color	Green	Via plating method	Not specified
Silkscreen	White	4-wire Kelvin test	No
Material type	FR4 TG135	Paper between PCBs	No
Via Covering	Plugged	Appearance quality	IPC Class 2 standard
Surface finish	HASL	Confirm production file	Yes
Deburring/Edge rounding	No	Silkscreen technology	Ink-jet/Screen printing silkscreen
Outer copper weight	1 oz	Inspection report	No
Inner copper weight	0.5 oz	Board outline tolerance	±0.2mm (regular)
Specify layer sequence	No	UL marking	No
Specify stackup	No	Countersink hole	No
Layer stackup	No requirement[1]	Backdrill	No
Gold fingers	No		

Table 19: Master device stencil order parameters

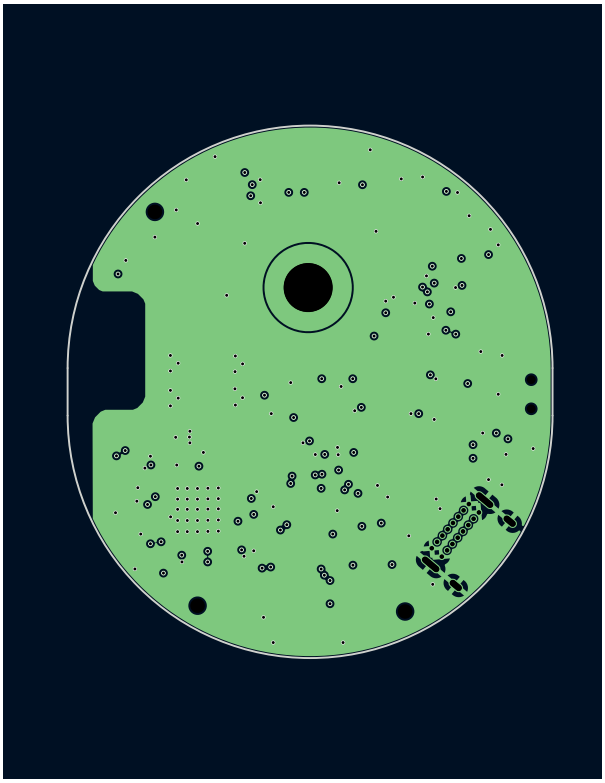
Parameter	Value	Parameter	Value
Framework	No	Polishing process	Sanding
Step stencil	No	Fiducials	No
Nano-coating	No	Confirm production file	Yes
Dimension	380 mm * 280 mm	Engrave text	No
Stencil side	Top	Ultrasonic-resistant adhesive	No
Stencil quantity	1		
Thickness	Not specified	Stencil process type	Solder paste stencil

The final layout and the generated 3D view in orthogonal projection are reported in Figure 53 and Figure 54, respectively.

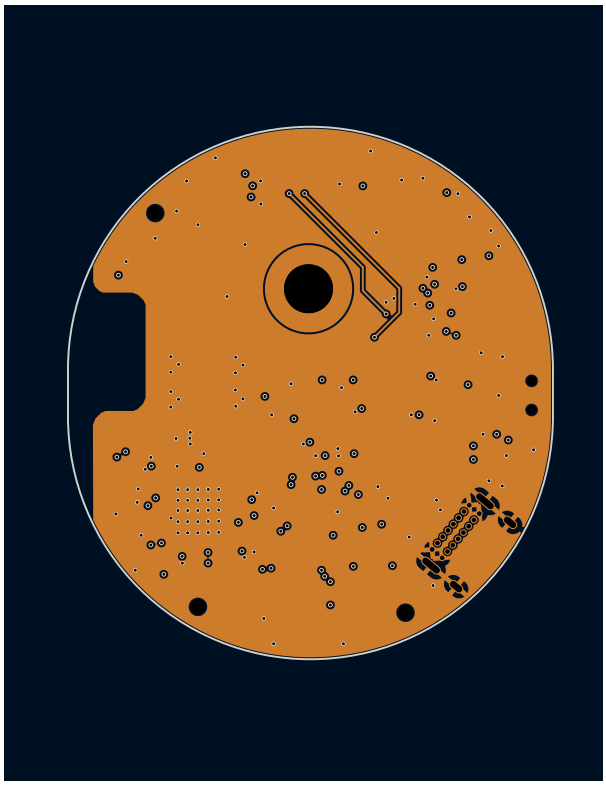
[1]While the PCB stackup is formally not specified, at the moment of the present work the manufacturer uses JLC04161H-7628 as the default stackup for four-layer (1-oz outer, 0.5-oz inner layer) PCBs.



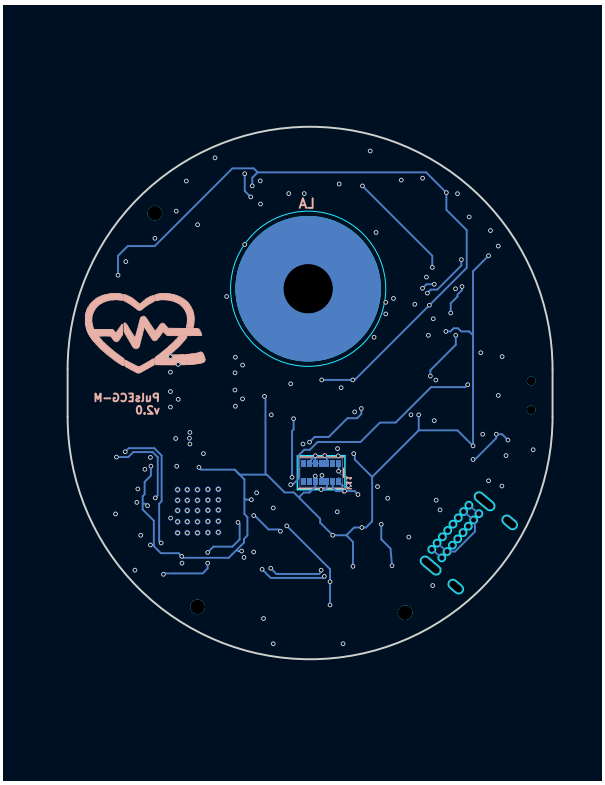
(a) Front layer



(b) In1 layer

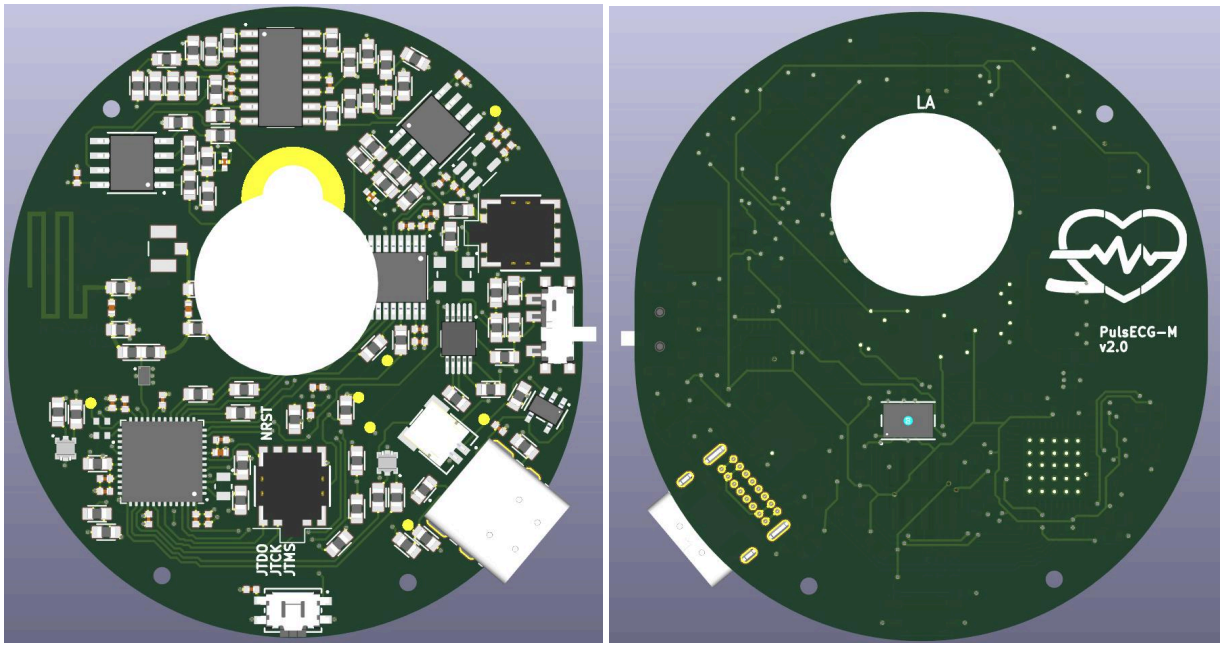


(c) In2 layer



(d) Back layer

Figure 53: PCB layers



(a) Top view

(b) Bottom view

(c) Side view

Figure 54: 3D model of the Master device PCB

PCB assembly

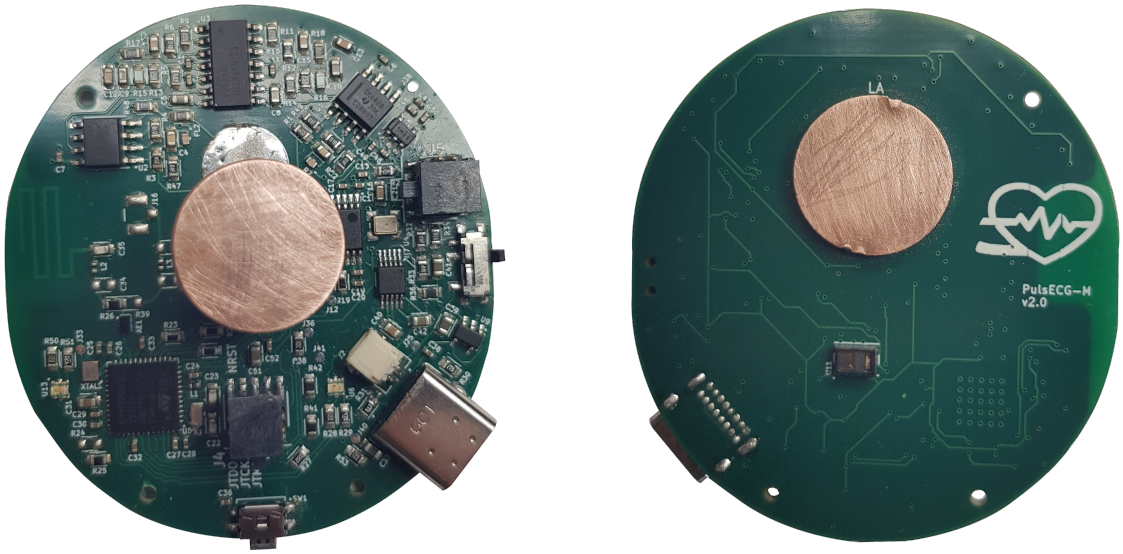
The Master device PCB was assembled on both sides with double reflow technique. Before attempting at the double reflow, the weight-to-pads-area ratio was calculated [60] to ensure that MAXM86161, the only component on the bottom side during the second reflow, would not detach under its own weight:

$$\frac{\text{Weight}}{\text{Solder joints area}} \approx \frac{0.015 \text{ g}}{14 \times 0.6 \text{ in} \times 0.4 \text{ in}} \approx 0.0089 \text{ g/in}^2 < 0.0471 \tag{17}$$

Since the ratio stays within the safe limit, it was decided to proceed. To assemble the bottom side, an old stencil from the prototype was used, and solder paste was tranferred to the footprint of the MAXM86161 sensor.

The SMD components were populated using a manual pick-and-place machine and then secured via a standard reflow soldering process.

The assembled Master PCB is reported in Figure 55.



(a) Top view. (b) Bottom view.

Figure 55: Assembled Master device PCB

PCB enclosure and final assembled device

The PCB enclosure was designed in Fusion 360 [61]. The design consists of the top and bottom parts connected with screws, with the PCB being placed in between, and is reported in Figure 56, Figure 57 and Figure 58.

The final assembled device is reported in Figure 59.

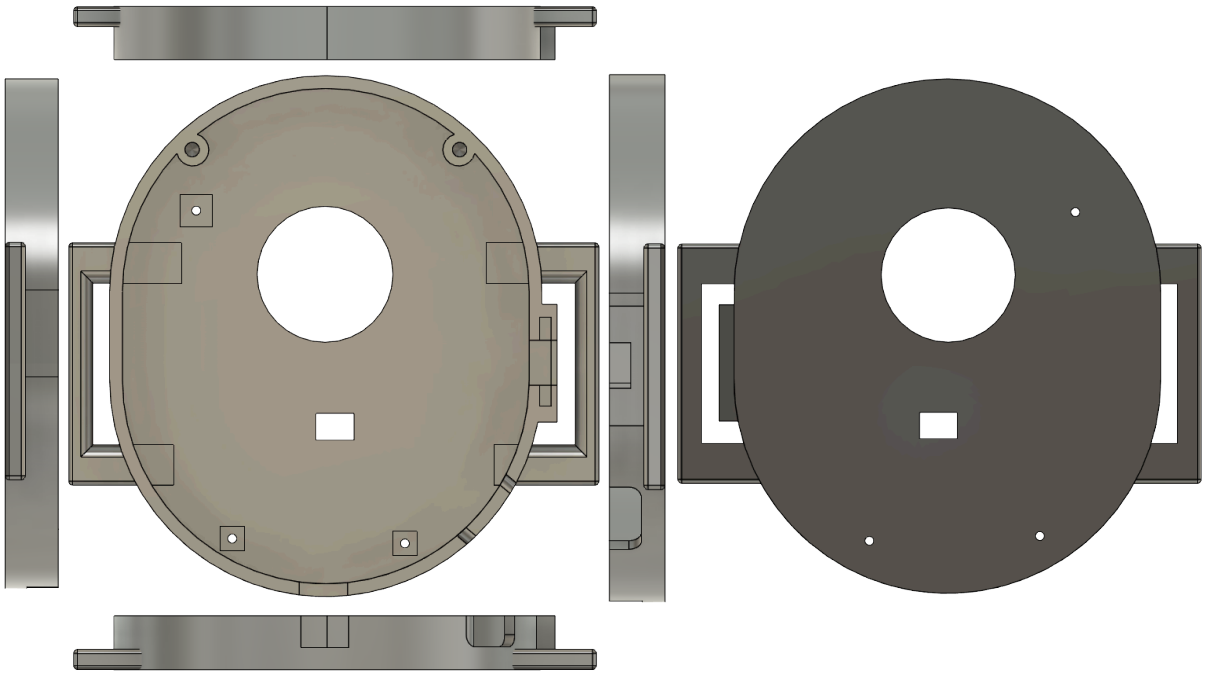


Figure 56: PCB enclosure, bottom half, six principal views

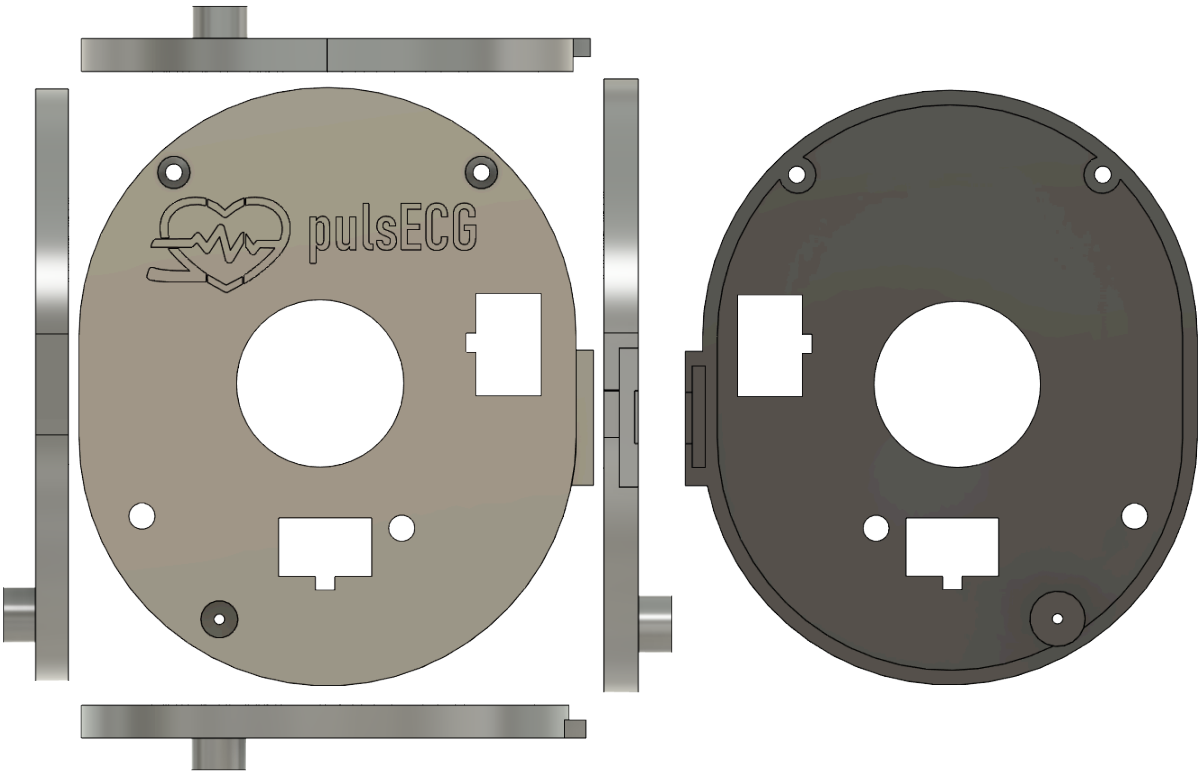


Figure 57: PCB enclosure, top half, six principal views

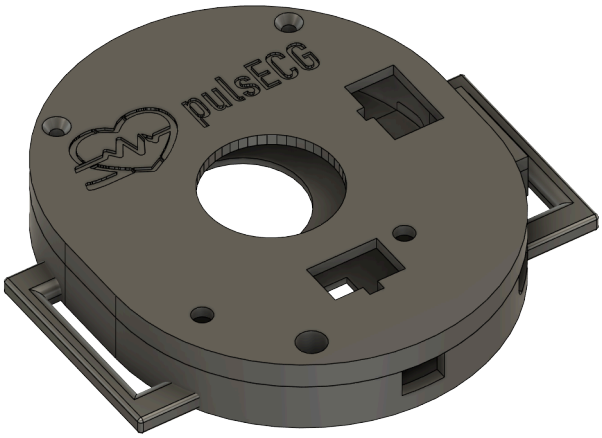


Figure 58: PCB enclosure, 3D view



Figure 59: Final assembled Master device

3.1.3 Layout overview

After the completion of the circuit schematic, the layout was created. The approach to the layout design is described in the following sections.

Electrodes attachment

During tests performed on the prototype it was discovered that poor soldering of the electrodes to the dedicated pads led to bad electric contact introducing noise to the signal and to mechanical damage caused by electrodes ripping the pads from the PCB surface after their prolonged usage.

The LA electrode is secured on the back of the PCB in a plated through hole. Its head is aligned with the pad on the back, while its shank is soldered to another pad on the front. This way a stable mechanical and electrical connection is established.

The RA electrode is glued to the case, and its shaft makes an electrical contact with a gold-plated spring finger on the front of the PCB upon assembly of the case. The gold plating provides a small contact resistance, which is crucial for small-amplitude signals like that of the ECG.

For the design to resemble that of the smartwatches, the connection of the INA826 to the LL electrode was implemented as a round flat cable, that would be incorporated in the buckle securing the device on the wrist. The round flat cable was preferred over a flat flexible cable, as the latter one is more prone to deterioration due to constant movement and distortion.

Domain separation

Considering that ECG signals exhibit very small amplitude ranging from 0.1 mV to 1 mV, they are very susceptible to electromagnetic interference (EMI) from adjacent traces. To maintain signal integrity and ensure a high signal-to-noise ratio, the layout was physically partitioned in analog, digital and radiofrequency domains. The analog domain hosts the circuitry necessary for ECG acquisition, while the digital domain contains the microcontroller and power management circuitry. A small region of the board was reserved for the RF signals.

Analog domain routing

The analog domain integrates the electrodes, INA826 instrumentation amplifiers, OPA4330 operational amplifiers, and the MCP3564 analog-to-digital converter.

The RA and LA electrodes are placed in the center of the board. For the RA, this placement facilitates the connection between the electrode and both INA, while for the LA it guarantees steady contact between the electrode and the wrist. The traces connecting the electrodes to the INA are made as short as possible. The INA themselves are rotated with the inputs toward the electrodes to facilitate routing. Given that the outputs carry an amplified signal, more robust and less susceptible to the EMI, such orientation of the amplifiers poses no risk, even though the outputs are routed partially under the components.

The passive components of the filters are arranged in a compact configuration around the OPA4330 to save space on the board. The conditioned signals of both ECG leads exit the operational amplifier form pins 1 and 14 of and are routed to the analog-to-digital converter on the second inner layer, which is shielded from the interferences originating from the front layer. Maintaining the signals on the top layer would inevitably lead to signal crossings requiring vias to be resolved. Furthermore, the parasitic resistance of a typical 0.3 mm via, being in milliohm range, is negligible compared to 260 kΩ differential input resistance of the converter. The parasitic inductance for such via is of the order of few nanohenry, which is insignificant at the frequencies of an ECG signal.

To minimize interference between the acquired signal and the digital outputs of the MCP3564, the converter is strategically placed at the boundary between two domains, with the analog inputs oriented towards the operational amplifier.

Digital domain routing

The decoupling capacitors and the oscillators accompanying the microcontroller, the ADC and the PPG sensor were placed as close as possible to the corresponding devices.

The SPI traces were routed in a bundle on the Front layer. In places where routing some of the signals on the bottom was unavoidable, stitching vias were placed to ensure that the return current travels along the corresponding signal trace.

Radiofrequency domain

To ensure the traces routing RF signals had 50 Ω characteristic impedance, the official calculator provided by the manufacturer JLCPCB [62] was used to calculate the correct trace width. The parameters used for the calculation, as well as the resulting trace width, are reported in Table 20. The implementation of the calculator is closed, and the exact closed-form equations and numerical methods are not reported.

Table 20: Trace width calculation parameters for the RF signals

Parameter	**Value**
Target impedance	50Ω
Type	Single Ended (Non coplanar)[2]
Signal layer	L1
Top reference layer	/
Bottom reference layer	L2
Trace spacing	/
Impedance trace to copper	/
Board stackup	JLC04161H-7628
Trace width	**0.3493 mm**

[2]This option corresponds to a microstrip.

All traces in the RF domain are routed with rounded corners in order to minimize impedance discontinuities associated with the angular corners and to reduce signal reflections.

The copper was removed from all layers under the meander antenna to not block the electromagnetic radiation and allow for the signal transmission.

3.2. Slave device ("SLVECG")

The second device measures the unipolar lead V_2 as a differential signal between the clinical V_2 signal location on the patient's chest and a reference on the right leg. To perform a measurement with this device, a pair of Adhesive electrodes is needed to be placed properly on the patient's chest. The electrodes are then connectable to the device via a *TENS* 3.5 mm jack cable [19]. The necessity to adopt such an acquisition method arose during the early prototypes testing phase, where some volunteers presented a chest morphology that a fixed distance pair of copper electrodes (whose pads are still available on the device) couldn't properly capture the lead signal on.



Figure 60: *TENS* 3.5 mm jack cable used for the thesis project.[19]

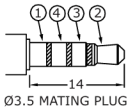
3.2.1. Schematic Diagrams

3.2.1.1. Analog Front-End

Being this second device meant to measure just a lead, it presents a simplified schematic diagram with respect to the Master board. In fact, only a differential signal is acquired so the Analog Front-End is halved with respect to the pulsECG one. Additionally, no SpO_2 sensor is present and no copper electrodes are mounted, since the contact between the patient and the system occurs via adhesive electrodes connected to a jack cable as can be seen in Figure 63. The cable is connected to is the jack port, and the component *SJ2-3594A-SMT-TR*[20] has been chosen:



Figure 61: Jack port *SJ2-3594A-SMT-TR* used for the SLVECG PCB.[20]



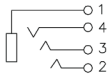
Model No.	SJ2-3594A-SMT-TR
Schematic	
PIN	
1	sleeve
2	tip
3	ring 1
4	ring 2

Figure 62: *SJ2-3594A-SMT-TR* Pins layout.[20]

Given the pinout of the component and the incoming differential signal within the *TENS* cable, **pins 1,3 and 4 have been connected to the same input of the Analog Front-End section**, whereas pin 2 represents the other input.

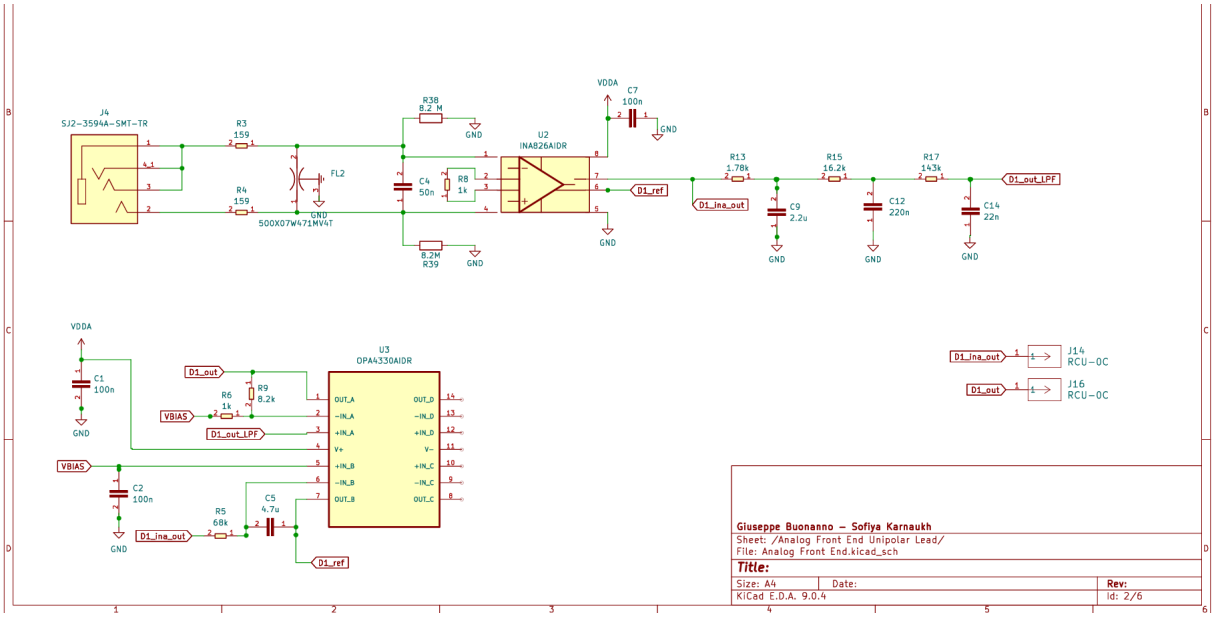


Figure 63: Analog Front-End of the slave device: amplifiers and hardware low-pass filter.

With previous considerations in mind, the ADC is only exploited for one differential channel, mapped the same way as the Master device.

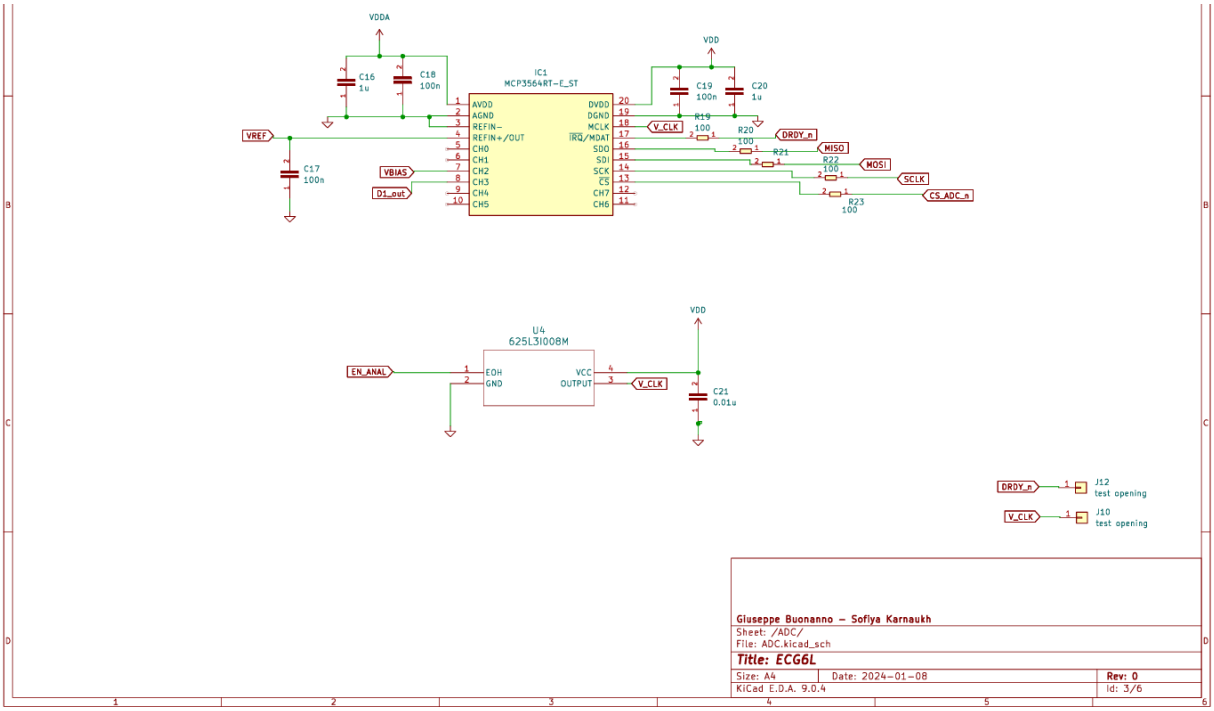


Figure 64: ADC section of the Slave device.

3.2.1.2. Microcontroller

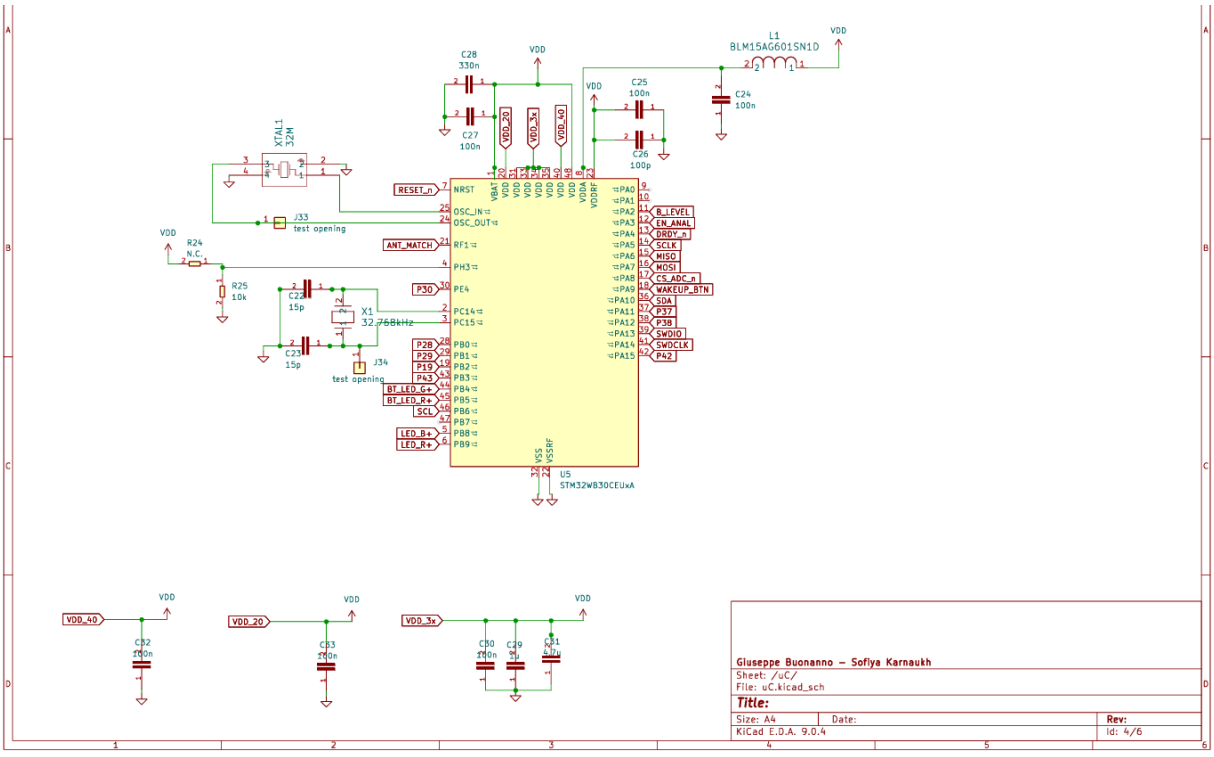


Figure 65: Microcontroller mapping of the Slave device.

3.2.1.3. Power management unit

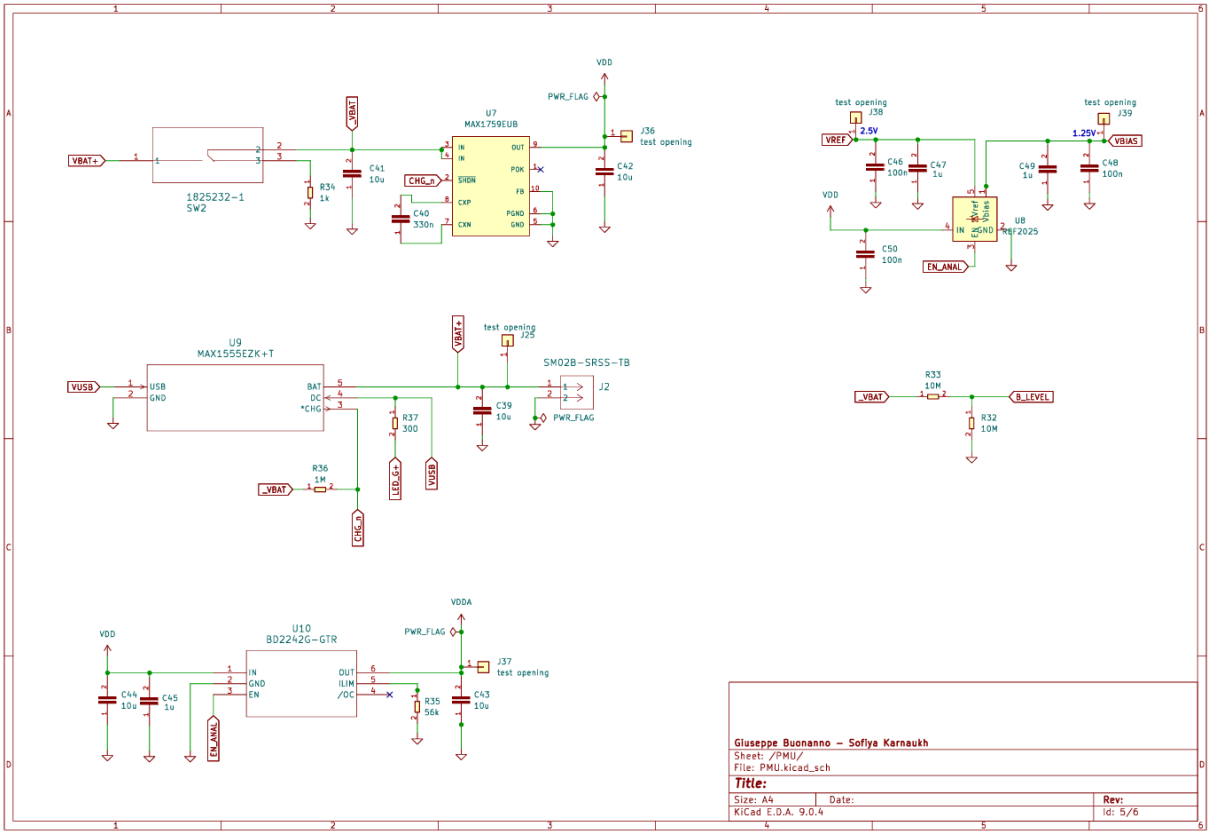


Figure 66: Power management of the Slave device.

3.2.1.4. Peripherals

Exactly like the Master device, the Slave device features two LEDs. The first LED, called *FN* is:

- Responsible for charging status (Green);
- ADC for ECG acquisition (Red for initialization, Blue for conversion and transmission).

The second LED, called *BT* is:

- Glowing in Green at a successful Bluetooth connection to the other device and the client (smartphone);
- Glowing in Red if the connection was not successful.

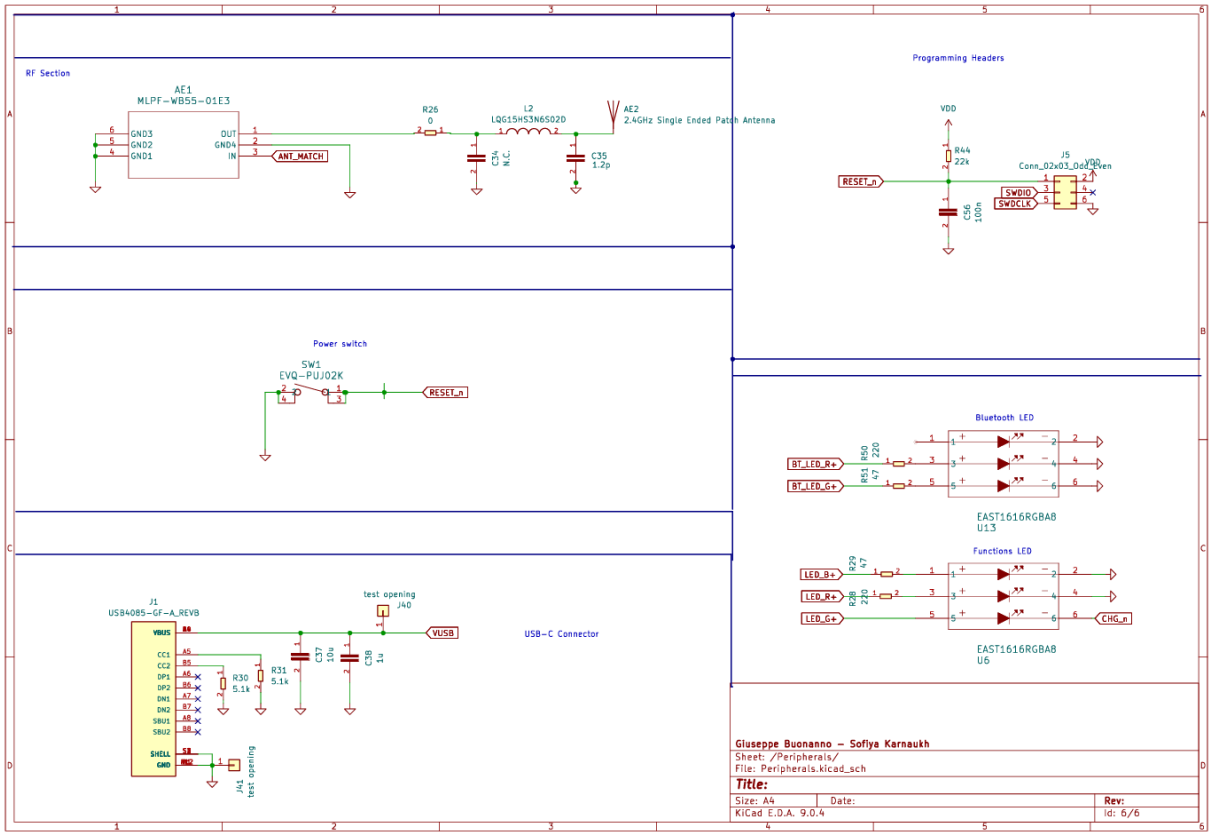
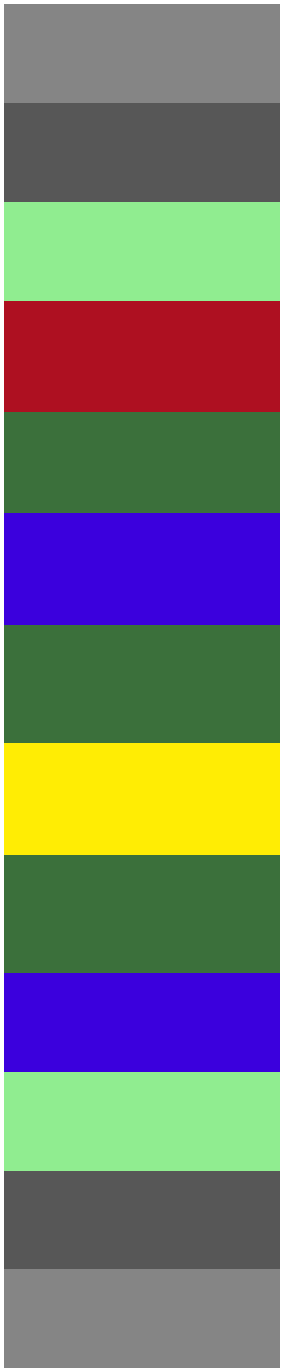


Figure 67: Peripherals of the slave device.

3.2.2. Board Overview

3.2.2.1. Stackup

Table 21: Slave device PCB stackup: table and cross-section schematic (not to scale)

Layer	Material	Thickness	ε_R	Cross-section
F.Silkscreen				
F.Paste				
F.Mask		0.01 mm	3.3	
F.Cu	Copper	0.035 mm		
Dielectric 1	PrePreg FR4	0.1 mm	4.5	
In1.Cu	Copper	0.035 mm		
Dielectric 2	Core FR4	1.24 mm	4.5	
In2.Cu	Copper	0.035 mm		
Dielectric 3	PrePreg FR4	0.1 mm	4.5	
B.Cu	Copper	0.035 mm		
B.Mask		0.01 mm	3.3	
B.Paste				
B.Silkscreen				

- **Top layer**: it hosts the whole ECG signal acquisition and conversion circuitry, the STM32 microcontroller, RF circuitry, status LEDs and the jack port for the measurement cable.
- **Ground layer** for both analog and digital signals, with a proper separation.

- **Voltages layer**: this layer is all dedicated to the 3.3 V voltage needed to power the circuit, with some minor voltage traces for the Analog Front-End or Bias voltage for the ADC. Signal and power integrity resulted to be improved with such choice.
- **Bottom layer**: contains all power-management circuitry, two pads to solder copper electrodes on and the battery connector. USB-C port and the power switch are faced on this layer. The copper electrodes were meant to be in contact with the patient's chest making a V_2 - RL measurement, but eventually it has been discarded given the uncorrectness of the measurements.

3.2.2.2. Characteristics

Table 22: Slave device PCB order parameters.

Parameter	Value	Parameter	Value
Dimensions	*54.25 mm ∗ 78.25 mm*	Electrical test	*Flying probe fully test*
PCB quantity	*5*	Castellated holes	*No*
Product type	*Industrial/Consumer electronics*	Press-fit hole	*No*
		Edge plating	*No*
Different design	*1*	Mark on PCB	*No*
Delivery format	*Single PCB*	Blind slot	*No*
PCB thickness	*1.6 mm*	Minimal via hole size/ diameter	*0.3mm/(0.4/0.45mm)*
Impedance control	*No requirement*		
PCB color	*Green*	Via plating method	*Not specified*
Silkscreen	*White*	4-wire Kelvin test	*No*
Material type	*FR4 TG135*	Paper between PCBs	*No*
Via Covering	*Plugged*	Appearance quality	*IPC Class 2 standard*
Surface finish	*HASL*	Confirm production file	*Yes*
Deburring/Edge rounding	*No*	Silkscreen technology	*Ink-jet/Screen printing silkscreen*
Outer copper weight	*1 oz*	Inspection report	*No*
Inner copper weight	*0.5 oz*	Board outline tolerance	*±0.2mm (regular)*
Specify layer sequence	*No*	UL marking	*No*
Specify stackup	*No*	Countersink hole	*No*
Layer stackup	*No requirement*[3]	Backdrill	*No*
Gold fingers	*No*		

[3]While the PCB stackup is formally not specified, at the moment of the present work the manufacturer uses JLC04161H-7628 as the default stackup for four-layer (1-oz outer, 0.5-oz inner layer) PCBs.

Table 23: Slave device stencil order parameters.

Parameter	Value	Parameter	Value
Framework	*No*	Polishing process	*Sanding*
Step stencil	*No*	Fiducials	*No*
Nano-coating	*No*	Confirm production file	*Yes*
Dimension	*380mm * 280mm*	Engrave text	*No*
Stencil side	*Top*	Ultrasonic-resistant adhesive	*No*
Stencil quantity	*1*		
Thickness	*Not specified*	Stencil process type	*Solder paste stencil*

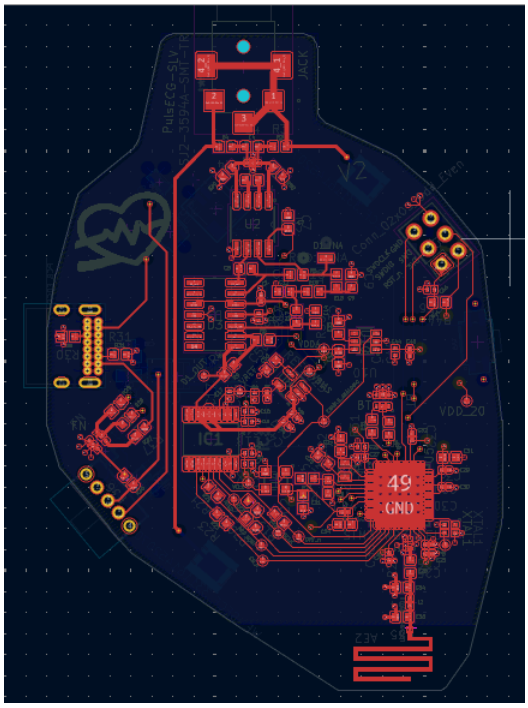


Figure 68: Top Layer.

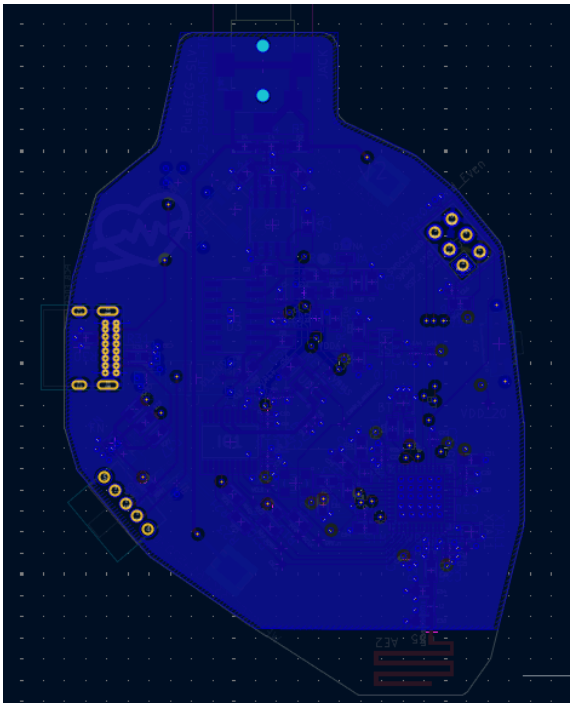


Figure 69: Ground layer.

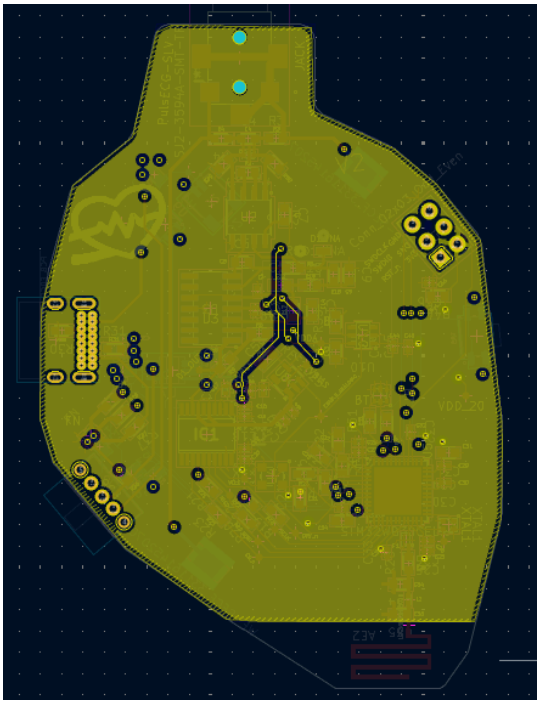


Figure 70: Voltages Layer.

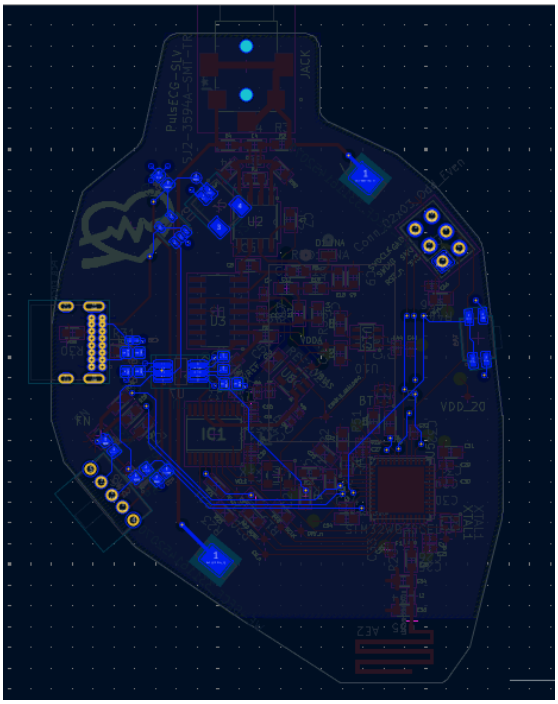


Figure 71: Bottom layer.

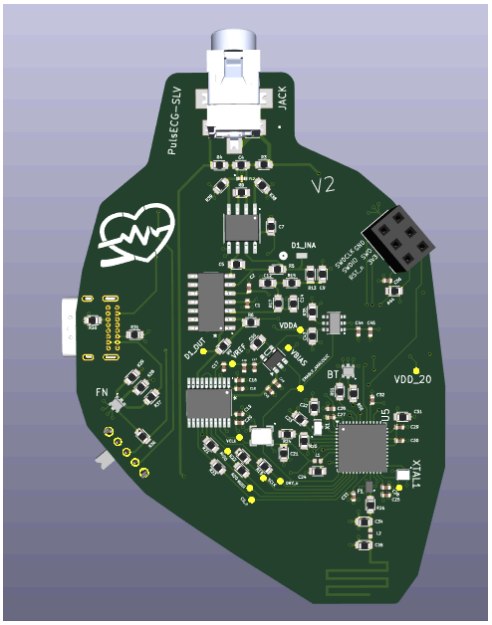


Figure 72: Top layer 3D View.

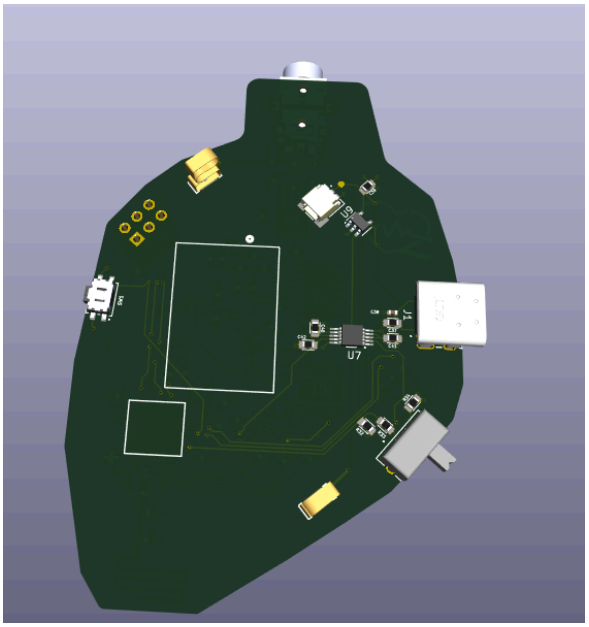


Figure 73: Bottom layer 3D View.

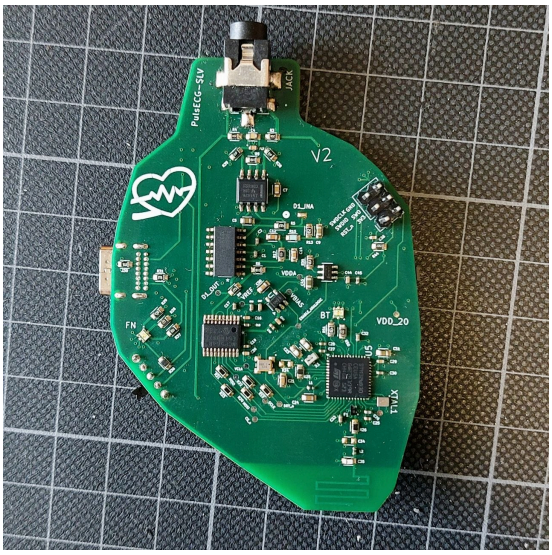


Figure 74: Assembled PCB View, front.

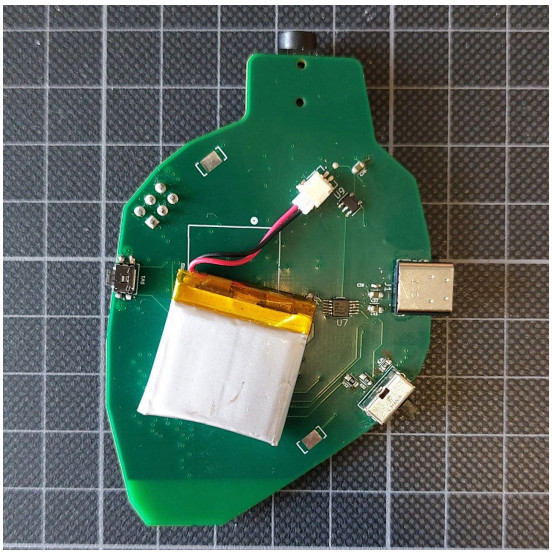


Figure 75: Assembled PCB View, back.

3.2.3. PCB Case Design

Finally, a 3D printed covering case for the circuit board has been designed, using *Fusion 360* by AutoDesk[61]. The case is shaped exactly like the PCB, and it has holes on the sides for the switch, the jack connector, the USB-C port and the push-button to reset the device. On the top, a hole is present for the programming interface as well as some circular housings for the LED beacons, the top section is decorated with some stylized artheries and veins and the project logo.

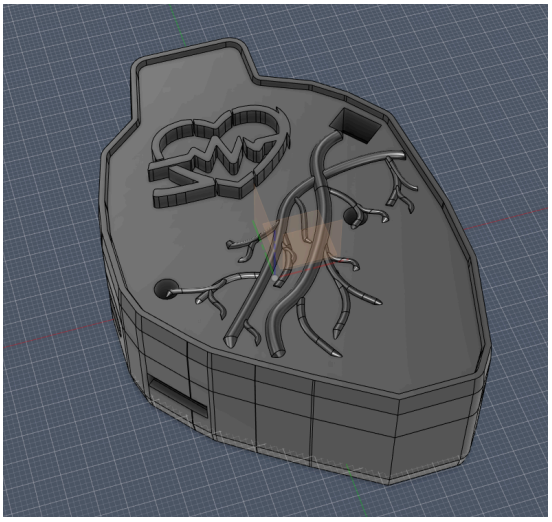


Figure 76: Case 3D View.



Figure 77: Final prototype view.

Chapter 4

Firmware development

The STM32WB30 processors found in both pulsECG and SLVECG devices run a custom firmware developed within the STM32CubeIDE environment.

4.1. STM32CubeIDE

STM32CubeIDE[63] is the official firmware production environment developed by STMicroelectronics. Within such program, it is feasible to program all ST microcontrollers and development boards, using C code. The integrated .ioc viewer is user friendly to map pins (*GPIOs*) of the chosen microcontroller to perform various functions. Depending on the microcontroller model, some pins are solely usable for a specific purpose such as power, radiofrequency or interconnection protocols (SPI, I2C, UART…).

4.2. STM32CubeProgrammer

STM32CubeProgrammer[64] is another program developed by STMicroelectronics. Unlike STM32CubeIDE, it gives deeper control on the memory of a ST microcontroller for specific purposes such as **flashing the Bluetooth Stack** or addressing and bytes handling. It is faster than STM32CubeIDE since it relies on a direct hardware interconnection.

4.2.1. Flashing the BLE Stack on STM Microcontrollers using STM32CubeProgrammer

An essential step to realize a functional BLE Device using an *STMWBXX* family microcontroller requires loading both the Bluetooth Stack and the *Firmware Upgrade Service* (FUS) onto the device memory. To do so, STMicroelectronics released on *GitHub* a fully explanatory guide [65] to flash the BLE Stack onto their devices:

- Firstly, on such guide, one has to search for the **Firmware Upgrade Services Binary Table**, and find the correspondent Address for the required FUS. As for July 2026, for a *STM32WB30* microcontroller the correspondence is:

FW Upgrade Services Binary	STM32WB3x(512K)	STM32WB3x(256K)	FUS compatibility	Version
stm32wb3x_FUS_fw_for_fus_0_5_3.bin	0x0807**A**000	0x0803**A**000	-	V1.0.0
stm32wb3x_FUS_fw_1_2_0.bin	0x0807**A**000	0x0803**A**000	-	V1.2.0
stm32wb3x_FUS_fw.bin	0x0807**A**000	0x0803**A**000	-	V2.2.0

- After that, on the **Wireless Coprocessor Binary Table**, the chosen BLE Stack address can be found:

Wireless Coprocessor Binary Table: Provides Install address for the targeted binary to be used in flash procedure "STEP 7" via USB or via SWD/JTAG.

Wireless Coprocessor Binary	STM32WB3x(512K)	STM32WB3x(256K)	FUS compatibility	Version
stm32wb3x_BLE_HCILayer_extended_fw.bin	0x08068000	0x08028000	-	V1.24.0
stm32wb3x_BLE_HCILayer_fw.bin	0x0806D000	0x0802D000	-	V1.24.0
stm32wb3x_BLE_HCI_AdvScan_fw.bin	0x08077000	0x08037000	-	V1.24.0
stm32wb3x_BLE_LLD_fw.bin	0x08078000	0x08038000	-	V1.18.0
stm32wb3x_BLE_Mac_802_15_4_fw.bin	0x0804C000	0x0800C000	-	V1.24.0
stm32wb3x_BLE_Stack_full_extended_fw.bin	0x08053000	0x08013000	FUS_v2 only	V1.24.0
stm32wb3x_BLE_Stack_full_fw.bin	0x0805C000	0x0801C000	FUS_v2 only	V1.24.0
stm32wb3x_BLE_Stack_light_fw.bin	0x08063000	0x08023000	FUS_v2 only	V1.24.0
stm32wb3x_Mac_802_15_4_fw.bin	0x0806D000	0x0802D000	-	V1.24.0
stm32wb3x_Phy_802_15_4_fw.bin	0x08069000	0x08029000	-	V1.24.0
stm32wb3x_Thread_FTD_fw.bin	0x08018000	NA	-	V1.24.0
stm32wb3x_Thread_MTD_fw.bin	0x0802C000	NA	-	V1.24.0
stm32wb3x_Thread_RCP_fw.bin	0x0806B000	0x0802B000	-	V1.24.0
stm32wb3x_Zigbee_FFD_fw.bin	0x0802B000	NA	-	V1.24.0
stm32wb3x_Zigbee_RFD_fw.bin	0x0803A000	NA	-	V1.24.0

Once these two addresses have been located, one can open the STM32CubeProgrammer, connect the custom board to the Computer and navigate to "Firmware Upgrade Services" section. There, specifying the addresses and starting a Firmware Upgrade operation for the FUS and then the BLE Stack will grant the correct upload of the BLE Stack into the microcontroller memory.[66]
After completion of the previous passages, one can now flash the firwmare code using STM32CubeIDE, and the device will be able to start BLE advertisement and perform a communication with other devices.

4.3. Interconnection protocols

An interconnection protocol is the most commonly used method for establishing communication between a microcontroller and a peripheral or another microcontroller. Utilizing a known protocol prevents compatibility failures, wiring conflicts, or timing mismatches. Furthermore, exploiting a protocol means repurposing the same infrastructure for multiple projects, reducing engineering effort. Some protocols rely on a *serial* data transmission, while others on several parallel lines running simultaneously. According to the chosen interconnection protocol, considerations about cost, systems architecture, and achievable data rate have to be taken into account, as well as ease of implementation, error detection, and flexibility for future modifications. As embedded systems grow more complex, protocols form the bedrock for stable performance, straightforward upgrades, and minimal rework. In embedded systems, protocols like *SPI*, *UART*, *I2C*, *CAN*, *USB* and *Ethernet* are widely adopted. Each of them has several advantages over the others as well as disadvantages.[67]
Given the chosen hardware components (such as the MCP3564R and the MAXM8161) for this thesis project realization, it has been decided to adopt **SPI**, **I2C**, **BLE** and **DMA** protocols for building the interconnection system within pulsECG and SLVECG devices.

4.3.1. SPI (Serial Peripheral Interface)

The SPI protocol is a 4-wire, synchronous, full-duplex serial protocol between a Master device and a peripheral device. The protocol allows the control of multiple peripheral devices from a single main device.
The interconnection length is usually short and used for simple, fast transactions with a peripheral, connectiond speed can easily reach the order of MHz.
The SPI connection wires are:

- *SPI Clock* (***SCK***): the interconnection clock signal generated by the main device;
- *Chip Select* (***$\overline{CS}$***): the logic is usually complemented, meaning the subnode is chosen when the $\overline{CS}$ signal is low (*logic 0*);
- *Main In Subnode Out* (***MISO***): Data stream from the subnode towards the main device, i.e. the microcontroller;
- *Main Out Subnode In* (***MOSI***): Data stream from the microcontroller towards the subnode, i.e. the peripheral device.

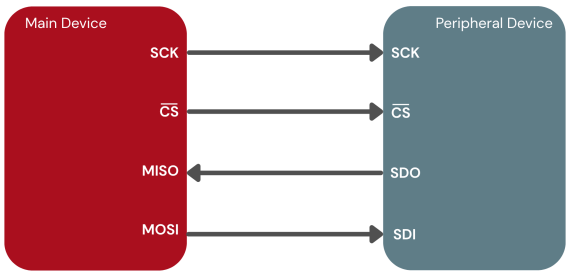


Figure 78: SPI configuration with a single peripheral.

To start a SPI transaction with a peripheral device, the main device sets the $\overline{CS}$ pin to 0, thus selecting a specific peripheral device. Furthermore, the main device starts generating the clock signal on the

SCK line.
At this point, the transaction can start, the peripheral device sends data through the *SDO/MISO* line whereas the master device sends it through *SDI/MOSI*. Both lines are concurrently active, being SPI a *full duplex* protocol, this means data is shifted in and out at the same time from both ends.
SPI clock has two parameters: *Clock Polarity* (**CPOL**) and *Clock Phase* (**CPHA**). The latter parameter dictates the data sampling/shifting on High/Low clock transition or the opposite one, whereas the former parameter chooses which polarity of the clock signal represents the *IDLE* state i.e. $\overline{CS} = 1$.

All previously exposed concepts are collected below:

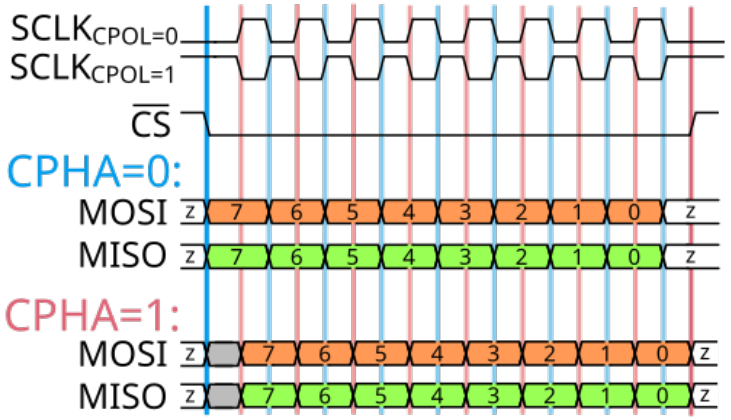


Figure 79: Example of an SPI transaction, waveforms. [21]

4.3.2. I²C

Inter-Integrated Circuit (I²C) is a two-wire synchronous serial communication protocol used for information exchange between multiple integrated circuits. The Open Systems Interconnection model distinguishes seven possible layers on which an interconnection protocol can be defined: physical, data link, network, transport, session, presentation, application layer. According to this model, the I²C protocol is defined only on physical layer and data link layer.

The current project employs the I²C protocol for the communication between the Master mcirocontroller and the PPG sensor MAXM86161.

4.3.2.1. Physical Layer

Physically, the I²C establishes that the devices involved into the communication are interconnected with a bus consisting of two wires that transmit two signals, serial data (SDA) and serial clock (SCL), correspondingly. Both wires are pulled up to the positive rail and hence bear a logical '1' when idling. Each device is interfaced to the lines with open-drain drivers. Such structure of the bus prevents accidental short circuits that may occur when two or more devices try to drive the same line simultaneously. A generalized schematic of the physical implementation of the protocol is reported in Figure 80.

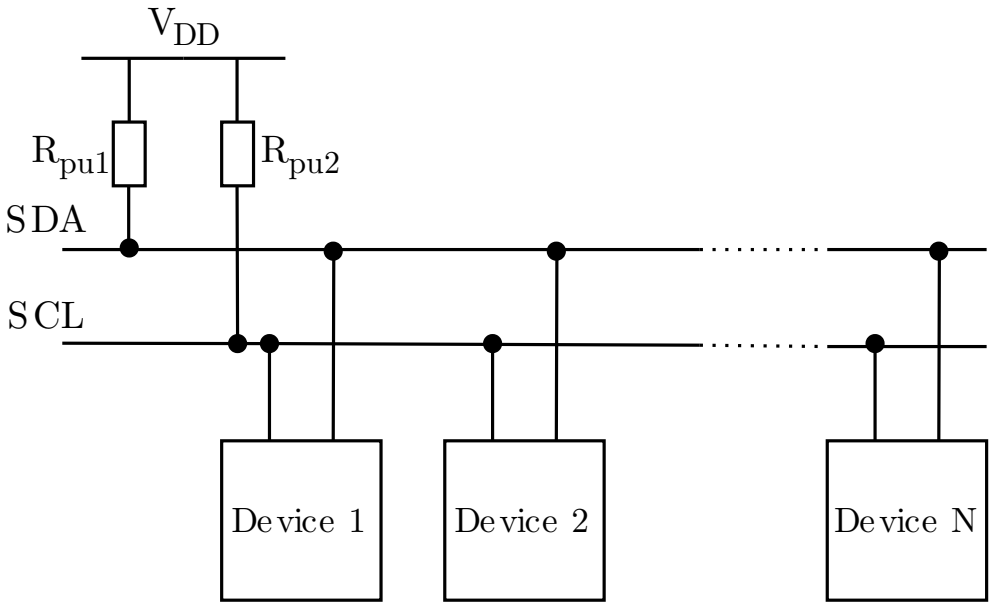


Figure 80: A generalized schematic of a physical implementation of I²C interface.

The SDA line is bidirectlional and is used to transmit stream of bits of data from controller (master) to target (slave) and vice versa. The SCL line is driven by the controller only and serves for synchronization purpose, as its rising and falling edges delimit time intervals during which the signal may be sampled by the target. In particular, SDA is sampled by target only when SCL is on the logical '1' level. Transitions on the SDA line are only allowed when the SCL stays on the logical '0' level.

4.3.2.2. Data Link Layer

Unlike SPI, I²C does not impose a strict requirement of the controller being defined at the circuit design stage. Any device connected to the I²C bus can act as a controller and initiate a transaction by sending start condition. Other devices on the same bus constantly monitor it for start and stop conditions and will not try to initiate a new transaction when the bus is busy.

At the beginning of each transaction, the controller transmits a start condition consisting in a falling edge on the SDA when the SCL is still idling and hence pulled high. Since during normal data transmission the SDA must stay constant when the SCL is pulled high, the start condition is easily distinguished from other possible configurations of the bus. After this the bus is considered "claimed" by the controller, and no other devices will try to claim it until the end of the current transaction.

After that, the controller waits for the target to transmit an Acknowledge (ACK) bit over the SDA line. If no device on the bus possesses the transmitted address, a Not Acknowledge (NACK) is received by the controller, resulting in the premature end of the transaction. After the ACK response from the target, the transaction proceeds.

The I²C does not impose any specific structure of the transaction, but on practice it is often composed of single or multiple consecutive multibyte messages. Each message begins with a byte consisting of the 7-bit target ID, MSB first, and one bit indicating the direction of the transmission, with '1' and '0' corresponding to the read and write events, respectively. The target response depends on the direction bit and the second transmitted byte. Each transmitted byte is followed by Acknowledge (ACK) or Not Acknowledge (NACK) from the device receiving the byte. Multiple messages within one transaction are separated by a Repeated Start (Sr) issued by controller, which bus configuration is identical to a normal Start.

At the end of transaction, the controller sends a Stop condition (P), which consists in a rising edge on the SDA for the SCL being at logical '1' level. Similarly to the Start condition, this bus configuration is impossible during normal data transmission and is therefore easily distinguishable. A timing diagram of a generalized I²C transaction is reported in Figure 81.

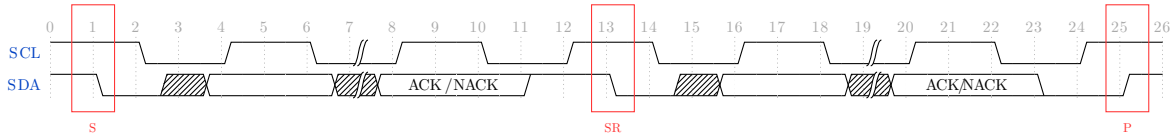
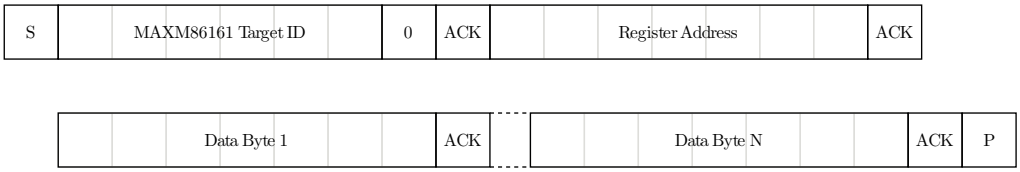


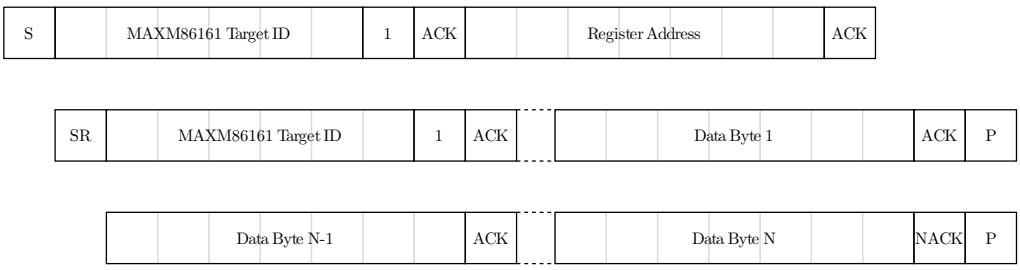
Figure 81: A timing diagram of a generalized I2C transaction. Start, Repeated Start and Stop conditions are highlighted in red.

4.3.2.3. MAXM86161 Supported Operations

In order to correctly implement communication between the microcontroller and the PPG sensor, the product specification was studied. The device supports single- and multibyte read and write operations. The bus behavior during the possible transaction types is depicted in @.



(a) Multiple Byte Write



(b) Multiple Byte Read

Figure 82: Semantic structures of the I²C transactions supported by the MAXM86161. Start, Repeated Start and Stop conditions are represented as S, SR and P, respectively.

The write transactions always consist of a single message. The controller supplies the device with the address of the first register and the array of bytes that will be written in the memory chunk starting from the provided address.

The read transactions are always multi-message, with the first message being a write operation providing the initial register address to the sensor. The second message is a read operation, in which the sensor sends the contents of the consecutive registers starting from the provided address. The data flow does not stop until the controller responds with NACK.

4.3.2.4. Arbitration

Despite the devices constantly monitoring the bus for the start and stop conditions, it is still possible for two or more devices to try to start a new transaction at the same time. For this reason, each transmitting device controls the level of the SDA after each bit transmission. A discrepancy in the transmitted and read values is an indicator of other devices trying to drive the bus, and by the arbitration rules the device that detects the discrepancy first loses the arbitration and disengages from the transmission.

4.3.3. DMA

Direct Memory Access (DMA) is the ability of a microcontroller peripheral to read and write directly to the system RAM bypassing the central processing unit (CPU).

In Digital Signal Processing (DSP), sensors and converters send continuous, high-speed data streams to the microcontroller. Without DMA, the CPU must to manage each memory access operation individually, which would lead to waste of CPU cycles and potentially stall data elaboration.

To offload the CPU, a DMA controller is used as a dedicated bus master.

In the Master and Slave device systems, the data streams are generated by two interfaces, SPI and I²C, which use two DMA channels each: one for transmission and one for reception. These channels move the data directly between the interface registers and the buffers in RAM.

4.3.4. Bluetooth© Low Energy (BLE)

The *Bluetooth© Low Energy* is wireless communication technology widely used for its low power consumption and communication speed. Such protocol is often used in IoT devices, wearable devices and, like in this project case, medical devices.

This technology follows the Generic Attribute Profile (GATT) concept to structure data transmission between two devices, using Services and Characteristics.
A **Service** is a collection of related Characteristics. A Service has to be marked with a ***UUID*** (*Universally Unique IDentifier*).
A **Characteristic** is the actual content of a BLE transaction i.e. the actual data to be exchanged. Commonly, one or more of the following operations can be indicated thus performed on a characteristic:

- **Read**: the characteristic content i.e. the data can be read by a Central device by means of a GATT request;
- **Notify**: whenever the characteristic changes, its new value is automatically forwarded (**Notified**) to the Central device, assuming the latter has *Subscribed* to the characteristic service. Notifications are also named *Indications*.
- **Write**: the characteristic can be overwritten with a value sent by the Central device, such operation can be either a direct command or can be acknowledged and responded to by a Server device (*write with response*).



Figure 83: Characteristics organization of a generic BLE service.

Devices supporting BLE are distinguished under the **GAP** (*Generic Attribute Profile*) convention, which gives the role of:

- **Client**: a Client device sends GATT commands or requests to interact with a characteristic of a service, hosted by a Server device.
- **Server**: a Server device hosts Services with their related characteristics, to be read, written or notified to Clients.

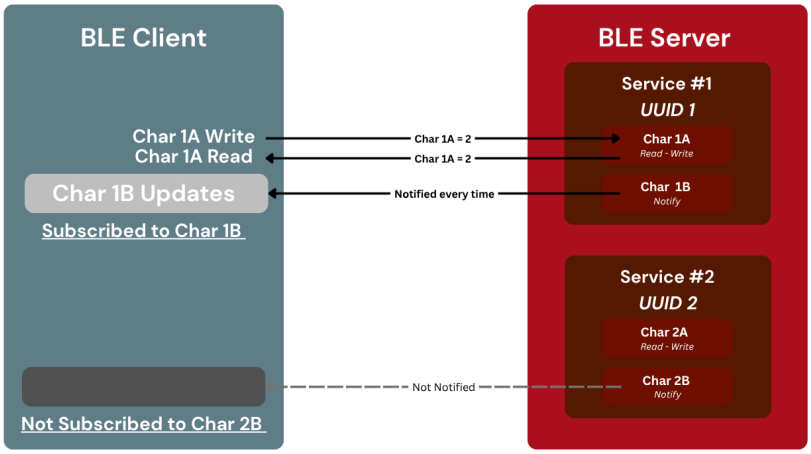


Figure 84: Example of BLE GATT transactions.

For an efficient data transfer between devices via BLE, the concept of **connection interval**, **Maximum Transfer Unit** (*MTU*) and **Payload** have to be properly evaluated:

- The *connection interval* states the *frequency* of data exchange, varying from 7.5 ms to a maximum of 4000 ms (4 seconds). After the Client device sends data (or a request), it has to wait for the Server to send an acknowledgment. Therefore, one (GATT) operation takes **two** connection intervals.
- The *MTU* indicates the maximum amount of transferable bytes within a GATT operation, including *protocol* bytes. Common MTU values range from 23 bytes to 512 bytes, depending on the *Bluetooth Stack* available on both devices.
- The *Payload* is the useful content of a transmission, thus it is smaller than the MTU since protocol bytes are excluded. The payload can assume different sizes according to the wanted operation as it can be seen in Table 24.

Table 24: Payload sizes depending on the GATT Operation.[40]

GATT Operation	Payload
Read	MTU - 1 byte
Write	MTU - 3 bytes
Notify	MTU - 3 bytes

Furthermore, the connection interval and the data rate are inversely proportional: a decrease in the connection interval brings a higher data rate. For example, using the smallest connection interval of 7.5 ms e.g., with a 125-byte payload, the data rate is:

$$\frac{1000 \ \text{ms}}{2 * 7.5 \ \text{ms}} * 125 \text{ bytes} = 8333 \ \text{bytes/s} = 66664 \ \text{bps} \quad \text{where} \quad [\text{bps}] = 8 * [\text{bytes/sec}] \tag{18}$$

Inversely, a connection interval of 4000 ms with 23-byte payload, leads to a data rate of:

$$\frac{1000 \ \text{ms}}{2 * 4000 \ \text{ms}} * 23 \text{ bytes} = 2.875 \ \text{bytes/s} = 23 \ \text{bps} \tag{19}$$

For the above-mentioned reasons, modern devices *negotiate* a suitable MTU depending on their capabilities. In the case of this thesis project, the MTU for both devices has been set to 512 bytes.

4.4. Tasks scheduling: the STM32 Sequencer

The STM32 *Sequencer* (or *Utility Sequencer*) refers to a lightweight task scheduling software provided by STMicroelectronics©. It is widely adopted in wireless applications (such as BLE or LoRa) for its

extremely low power consumption, and conflicts prevention between background tasks and interrupts. The Sequencer acts as a priority-based cooperative scheduler, and it is designed to replace complex *while(1)* loops or heavy RTOS kernels in resource-constrained applications. Peculiarities of the STM32 Sequencer are:

- **Cooperative Multitasking**: Each task runs to completion. There is no preemption. A task cannot be interrupted by another task, only by hardware interrupts.
- **Power Management**: When no tasks are pending, the sequencer automatically calls an Idle function, making it easy to enter low-power modes (Stop or Standby).
- **Priorities**: Priority is defined by the assigned bit index, where usually lower indexes correspond to higher priority.
- **Event Handling**: Allows tasks to wait for specific signals (events) before resuming execution.

For the abovementioned reasons, exploiting the Sequencer in this thesis project has been a straightforward decision. Including the *header* file of the Sequencer i.e. `stm32_seq.h` in the `main.c` code allows the usage of the Sequencer functions such as:

- `UTIL_SEQ_RegTask(1<<CFG_TASK_ID, CFG_SCH_PRIO_X, function_name)`: To register a function `function_name` as a Task, associating it to an *ID* (`CFG_TASK_ID`) that can be customized. Moreover, `CFG_SCH_PRIO_X` indicates the Task priority (X), which can start from 0 up to 32.
- `UTIL_SEQ_SetTask(1<<CFG_TASK_ID, CFG_SCH_PRIO_X)`: To notify the Sequencer that a specific Task has to be executed with a given priority. If the set priority differs from the one given at Task registration, the Task execution won't be coherent with expectations.
- `UTIL_SEQ_Run()`: This function constantly checks for ready tasks and executes them following the priority order. Usually, it can be found as `UTIL_SEQ_Run(UTIL_SEQ_DEFAULT)` inside the `MX_APPE_Process()` function, which is closed in a `while(1)` loop in `main.c`.
- `UTIL_SEQ_WaitEvt(EVT_NAME)`: Suspends a Task execution until the reception of the event `EVT_NAME`. Such an event is usually an Interrupt.

As will be seen in the following sections, the usage of the Sequencer functions has been merged with the previously cited Interconnection protocols to create an effective, non-blocking chain of operations that can be triggered via simple BLE commands.

4.5. Code overview

4.5.1. main

The main code is responsible of the initialization of the whole firmware part since it initializes all required peripherals within the microcontroller used in the project, as well as the Bluetooth stack.

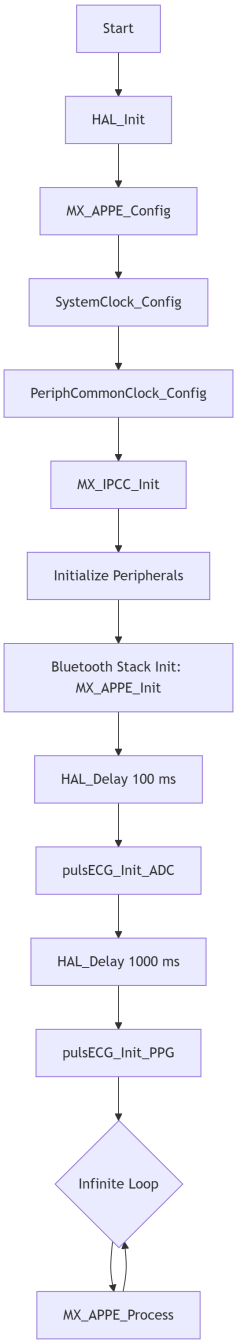


Figure 85: main.c flow of pulsECG.

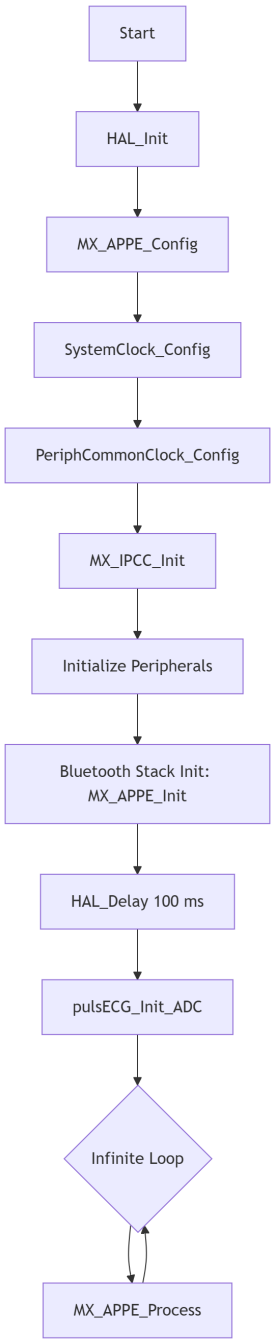


Figure 86: main.c flow of SLVECG.

4.5.2. ECG Acquisition

Files `adc.h` and `adc.c` include all the implemented functions to enable both the analogic and digital circuitry responsible of ECG signals acquisition. These files are included in both devices firmware.

4.5.2.1. Setup

As seen in the previous section, the first function to be used is `pulsECG_Init_ADC`, which is responsible of creating and registering the *MCP3564R* ADC initialization task, scheduled immediately after, as well as registering the battery level task.
The function associated to the ADC initialization task is `ADC_init`, which communicates via SPI with the MCP3564R, setting its registers in preparation for ECG acquisitions.
Among such registers, the *CONFIG3* register allows modifying the format of output data. In fact, the 32 bits of the ADC output data register can be organized into various formats, and since the master device acquires samples from two distinct channels (for the LA-RA and LL-RA pairs of electrodes), it has been necessary to highlight the channel from which the converted data is coming from. By setting both bits 5 and 4 of the CONFIG3 register to '1', the output format is subsequently organized as:

- Bits **31:28**: *CHID[3:0]* i.e. 4 bits dedicated to the channel the converted data belongs to;
- Bits **27:23**: 4 bits of sign extension of converted data;
- Bits **23:0**: 24-bit converted data;

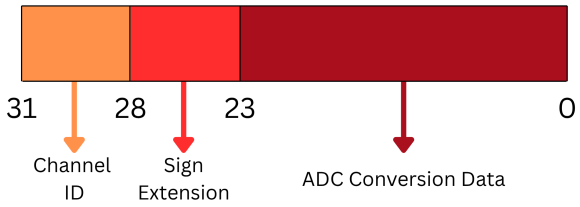


Figure 87: Output format of the MCP3564R for this project.

In this way, data belonging to lead I or lead II can be easily distinguished on the receiver side, since the ADC channel bits are hardcoded by the manufacturer and can be retrieved from the datasheet. Recalling Equation 14, the MCP3564R sampling frequency is 390 Hz, meaning 195 Hz per channel. The complete initialization flow of the MCP3564R is shown in Figure 88

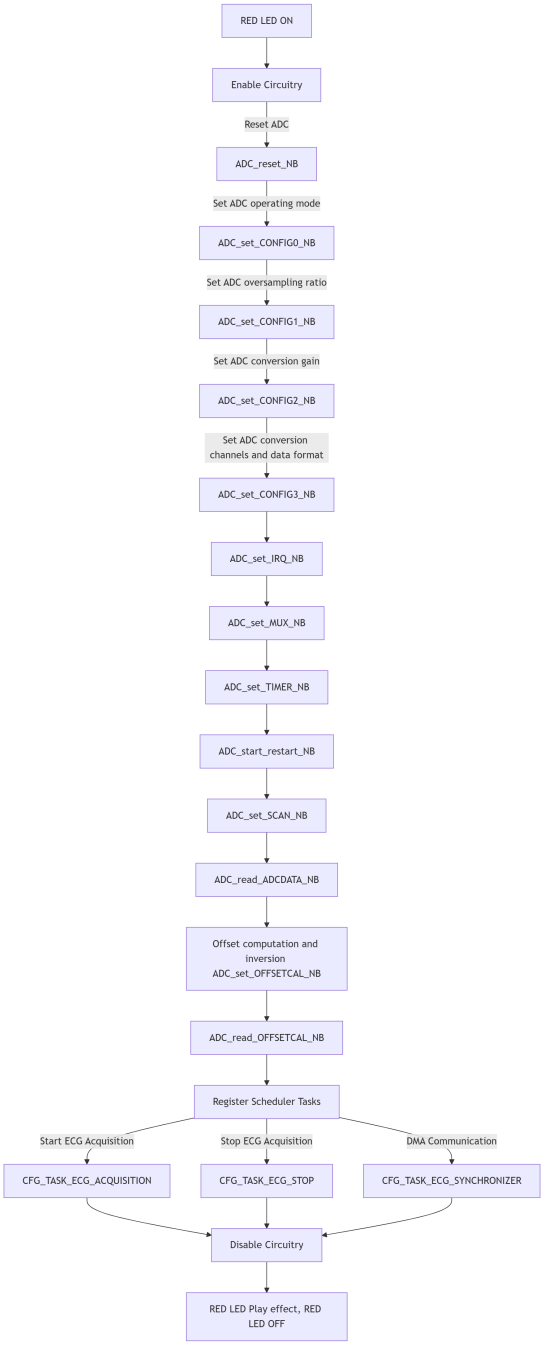


Figure 88: MCP3564R Initialization task flow.

Once the initialization task has been completed, the circuitry is put on stand-by again, waiting for a Bluetooth command to start an acquisition.

4.5.2.2. Sequencer tasks

Table 25: Seuqencer tasks related to the ECG acquisition

Task name	Priority	Task function
`CFG_TASK_ECG_ACQUISITION`	0	`void ADC_ACQUISITION(void)`
`CFG_TASK_ECG_SYNCHRONIZER`	1	`void ADC_buffer_out(void)`
`CFG_TASK_ECG_STOP`	0	`void ADC_STOP(void)`

4.5.2.3. Bluetooth Services and Characteristics

Before presenting the sequence of firmware operations to capture ECG signals, an overview of BLE Services and Characteristics for such operations has to be introduced, since both devices are meant to be controlled by a Bluetooth Client, which is the smartphone App.
The ECG service, called `ECG_Service` for both devices, contains two characteristics:

- **CharSS**: to start/stop an ECG acquisition, it has the *Write* property and its length is of two bytes. Writing '1' to the least significant byte of the characteristic will start an acquisition, whereas writing '0' terminates it;
- **CharECG**: characteristic containing ECG converted samples by the MCP3564R, it has a Payload of 247 bytes.
  This characteristic has been set to *Notify* to forward samples to the Client subscribed to this characteristic;

Table 26: BLE GATT entries used for ECG data transfer, pulsECG device

Entry	Type and UUID	Scope
ECG	Service 00000001- CC7A-482A-984A-7F2ED5B3E58F	Hosts the ECG-related characteristics
CharSS	Characteristic 00000002-8E22-4541-9D4C-21EDAE82ED19	Write-only characteristic defined on 2 bytes and used as a state variable by the microcontroller. By writing 0x0000 or 0x0001 to this characteristic, the user device commands the microcontroller to stop or start the acquisition, respectively
CharECG	Characteristic 00000003-8E22-4541-9D4C-21EDAE82ED19	Read and *Notify* characteristic with maximum length of 247 bytes used as data buffer for raw ECG data. Notifies the subscribed user device when new data is written onto the characteristic

Table 27: BLE GATT entries used for ECG data transfer, SLVECG device

Entry	Type and UUID	Scope
ECG	Service 00000101- CC7A-482A-984A-7F2ED5B3E58F	Hosts the ECG-related characteristics
CharSS	Characteristic 00000022-8E22-4541-9D4C-21EDAE82ED19	Write-only characteristic defined on 2 bytes and used as a state variable by the microcontroller. By writing 0x0000 or 0x0001 to this characteristic, the user device commands the microcontroller to stop or start the acquisition, respectively
CharECG	Characteristic 00000033-8E22-4541-9D4C-21EDAE82ED19	Read and *Notify* characteristic with maximum length of 247 bytes used as data buffer for raw ECG data. Notifies the subscribed user device when new data is written onto the characteristic

The need to distinguish between Master services and Slave services was due to avoid conflicts between the two devices when they are both active and connected to the same Client device. In fact, the latter one has

to be capable of distinguishing the source of the BLE notifications, thus the services and characteristics of the two devices have to be set with different UUIDs.

4.5.2.4. Starting an acquisition

To start an ECG signals acquisition, it is necessary to write '1' on the *CharSS* characteristic from a Client device.

Both devices receive the command on the Bluetooth listener code (i.e. `custom_stm.c`), and in this case the `CFG_TASK_ECG_ACQUISITION` task is scheduled, its associated function `ADC_ACQUISITION` is consequently executed. The acquisition task turns the conversion circuitry on by setting `ENABLE_ANALOGIC` pin to '1', initializes a new SPI transaction with the ADC setting $\overline{CS}$ to '0'. Then, by sending the `ADC_START_RESTART` command, the ADC starts converting signals from the analog front-end i.e. the ECG signals of the patient interacting with the systems. Being the ADC peripheral enabled for SPI transactions, DMA calls are triggered, thus the `ADC_DRY_Handler` function is called, which is responsible of filling a buffer with converted data. In the meantime, the `CFG_TASK_ECG_SYNCHRONIZER` task is scheduled. Its task function `ADC_buffer_out` takes chunks of the conversion buffer and forwards them via Bluetooth to the client device subscribed to the *CharECG* characteristic. In other words, the two functions work along, one is responsible of filling the buffer of converted data arriving from the ADC, and the other forwards a portion of it, creating a **circular buffer** improving the throughput without losing information on the receiver's end. A graphical explanation of the acquisition process can be found in Figure 89

4.5.2.5. Stopping an acquisition

The acquisition flow renews itself by checking some flags such as `is_receiving_samples_ADC`, however it can be stopped if devices receive by a client a '0' writing on the *CharSS* characteristic. When this occurs, the same steps occur as for the acquisition start: `CFG_TASK_ECG_STOP` task is scheduled, and the `ADC_STOP` function is executed. Such function resets the SPI interface, sets the $\overline{CS}$ signal to '1' and the `ENABLE_ANALOGIC` to '0', switching off the whole conversion circuitry on both devices. The power consumption of both devices is significantly reduced in such a scenario.

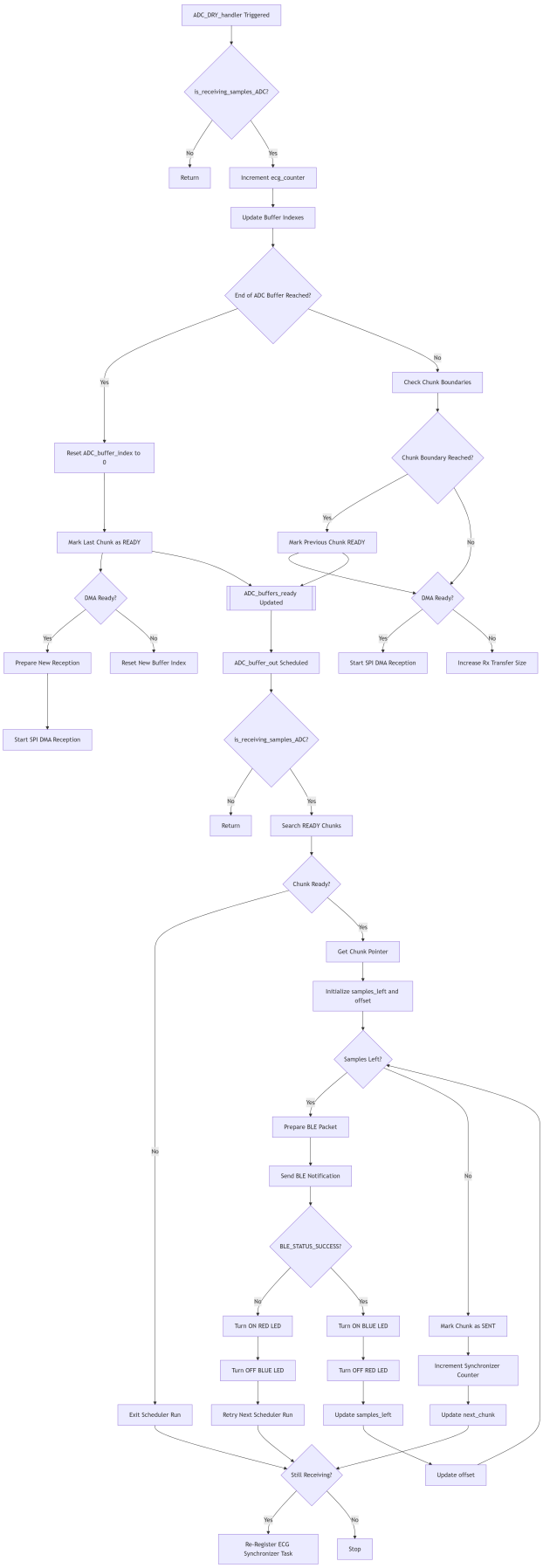


Figure 89: ECG Acquisition flow, Devices side.

4.5.3. SpO_2 Acquisition

In the present project, the SpO_2 and the ECG acquisitions were designed separately but using the same principles. The following sections overview the basic functionality of the PPG side of the firmware.

4.5.3.1. Startup

At the Master device startup, the part of the GATT profile associated with the PPG is registered by the microcontroller. It is defined in `custom_stm.h` and `custom_stm.c` and consists of the PPG service, along with the characteristics `CharPPGStart` and `CharPPGNotify`. Their UUIDs and scope are described in the following section.

Prior to entering the main loop of the sequencer, the function `pulsECG_Init_PPG` is invoked to register all sequencer tasks related to the PPG. The corresponding task list is reported in Table 28, while the associated are described in the sebsequent sections. Task identifiers are defined using the enumerator values provided in `app_conf.h`. The highest priority level is assigned the value '0'.

Table 28: Seuqencer tasks related to the PPG sensor

Task name	Priority	Task function
`CFG_TASK_PPG_START_ACQUISITION`	0	`void PPG_acquisition(void)`
`CFG_TASK_PPG_SYNCHRONIZER`	1	`void PPG_buffer_out(void)`
`CFG_TASK_PPG_STOP_ACQUISITION`	0	`void PPG_stop(void)`

4.5.3.2. Bluetooth Services and Characteristics

The PPG service and related characteristics are described in Table 29.

Table 29: BLE GATT entries used for PPG data transfer

Entry	Type and UUID	Scope
`PPG`	Service 00000003-cc7a-482a-984a-7f2ed5b3e58f	Hosts the PPG-related characteristics
`CharPPGStart`	Characteristic 00000005-8e22-4541-9d4c-21edae82ed19	Write-only characteristic defined on 2 bytes and used as a state variable by the microcontroller. By writing 0x00 or 0x01 to this characteristic, the user device commands the microcontroller to stop or start the acquisition, respectively
`CharPPGNotify`	Characteristic 00000006-8e22-4541-9d4c-21edae82ed19	Read-only characteristic with maximum length of 247 bytes used as data buffer for raw PPG data. Notifies the user device when new data is written

4.5.3.3. Starting acquisition

The acquisition begins with the user device writing '1' into the `CharPPGStart` characteristic. This triggers a custom event handler defined in `custom_stm.c`, which sets the task `CFG_TASK_PPG_START_ACQUISITION` to be executed next by the sequencer.

Upon execution, the task function sets `EN_ANAL = 1` and therefore powers on the analog circuitry, then proceeds to initialize the PPG registers. The values written in the design-relevant registers are explained in Table 30.

Table 30: MAXM86161 register initialization values

Address and register	Value and explanation

0x0D System Control	0b00001000 `SINGLE_PPG = 0b1` as prescribed by the datasheet, `LP_MODE = 0b0` to not have sampling rate limited to 256 Sa/s
0x2A LED Range 1	0b00111111 Current ranges of all three LEDs are set to their maximal value, 124 mA
0x29 LED PILOT PA	0b00100000 Current of the pilot LED in the proximity mode is set to 15.56 mA
0x15 Photo Diode Bias	0b00000001 `PDBIAS1 = 0b001` configures the photodiode bias circuit to match the lowest range of C_{PD} values
0x10 PPG Sync Control	0b10000000 `TIME_STAMP_EN = 1` enables timestamp being saved each 8 samples in the FIFO to control integrity of the samples
0x11 PPG Configuration 1	0b00001111 `PPG_TINT = 0b11` for the maximal integration time, `PPG1_ADC_RGE = 0b11` for the maximal ADC range, `ALC_DISABLE = 0b0` to enable ambient light compensation
0x12 PPG Configuration 2	0b00101010 `SMP_AVE = 0b010` to average on 4 samples, `PPG_SR = 0b00101` for 400 Sps sample rate
0x13 PPG Configuration 3	0b11000000 `BURST_EN = 0b0` to disable burst mode, `BURST_RATE = 0b00` since burst mode is disabled, `DIG_FILT_SEL = 0b0` for ambient light cancellation with Central Difference Method, which offers superior performance, `LED_SETLNG = 0b11` to let the LEDs settle before the ADC integration starts
0x09 FIFO Configuration 1	0b00000000 Since `A_FULL_EN` interrupt is disabled, the value of `FIFO_A_FULL` is irrelevant
0x0A FIFO Configuration 2	0b00000000
0x20 LED Sequence Register 1	0b00110010 `LEDC1 = IR LED`, `LEDC2 = RED LED`
0x21 LED Sequence Register 2	0b00001001 `LEDC3 = Ambient light`
0x22 LED Sequence Register 3	0b00000000 No exposures programmed for `LEDC5` and `LEDC6`
0x23 LED1 PA	0b01000000 Set green LED driving current to 31.12 mA
0x24 LED2 PA	0b01000000 Set IR LED driving current to 31.12 mA
0x25 LED3 PA	0b01000000 Set RED LED driving current to 31.12 mA
0x14 Prox Interrupt Threshold	0d48 Threshold value of 48 was proved experimentally to not cause false positives in proximity detection.

0x02 Interrupt Enable 1	0b01010000 `DATA_RDY_EN = 0b1` and `PROX_INT_EN = 0b1` to make the sensor generate an interrupt on data ready and proximity events

Before exiting, the task function sets the flag `PPG_is_acquiring_samples = 1` and enables the interrupts from the PPG sensor. It clears the interrupt flags in the Interrupt Status 1 register to allow for the new interrupts to occur, and sets for the execution the task `CFG_TASK_PPG_SYNCHRONIZER`.

4.5.3.4. Acquiring samples

The data acquisition architecture is comprised of two asynchronous processes: local buffering of the PPG data on the microcontroller and subsequent transmission to the user device via BLE.

Local buffering is managed by a finite state machine (FSM). Deterministic state transitions of the FSM are driven by hardware interrupts generated by the I_2C interface and by the sensor itself at `INT_SpO2` pin. The state diagram of the FSM is illustrated in Figure 90.

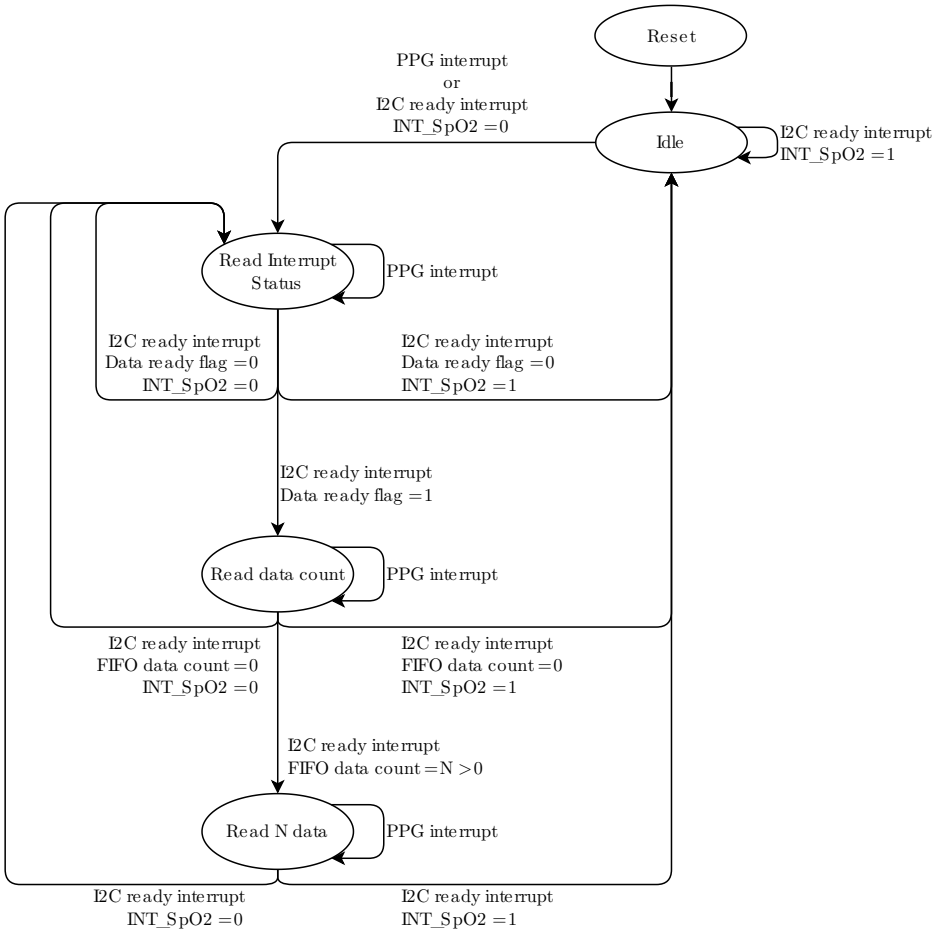


Figure 90: The state diagram of the FSM responsible for the PPG acquisition.

During execution, the FSM sequentially writes PPG samples into a circular buffer, designated as `PPG_buffer`, at the memory location referenced by the pointer `PPG_buffer_write_index`. To ensure high throughput of outgoing BLE packets per unit time, the buffer is partitioned in six discrete blocks, from now on referred to as chunks, containing 40 samples each. The chunks are sent one by one as they are filled with new data, as seen in Figure 91. The buffer segmentation approach allows to reduce the throughput of the transmitted payloads, thus facilitating the real-time digital processing on the user device.

A helper function `PPG_update_buffer_pointer` is called at each buffer write. It manages pointer wrapping and activates the flag `PPG_can_send = 1`, signaling that a new chunk is ready for the transmission.

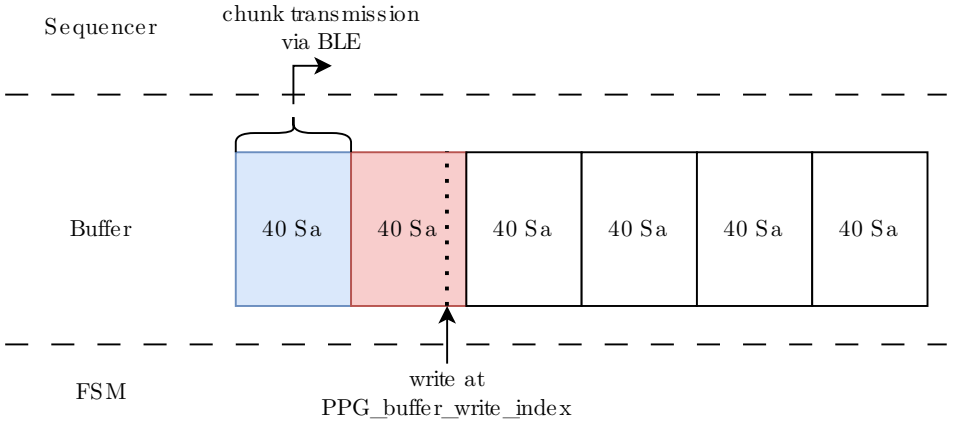


Figure 91: The circular buffer for the PPG data samples and its access to by the sequencer and the FSM.

The transmission of the chunks via BLE is managed by the `CFG_TASK_PPG_SYNCHRONIZER` task, which is executed periodically by the sequencer. Upon execution, the task function checks the `PPG_can_send` flag, determines the index of the currently active chunk, and decrements this index by one to obtain the index of the chunk that needs to be transmitted. To achieve periodic execution, the task reschedules itself at the end of the task function.

This implementation relies on the assumption that the sequencer runs the task with a frequency sufficient to avoid multiple chunks being filled between two consecutive task executions. The validity of this assumption was confirmed on practice.

4.5.3.5. Stopping acquisition

The acquisition will stop when the user device writes 0x00 in the `CharPPGStart` characteristic. This triggers an event handler that schedules `CFG_TASK_PPG_STOP_ACQUISITION` task for execution, which resets the buffer writing pointer, resets the FSM state to Idle, and powers off the analog front end.

Chapter 5

Mobile Application: pulsECG-X

The acquisition start/stop mechanism was initially validated using the ST BLE Toolbox application [68]. Such application served as a debugging tool confirming the expected functional behavior for both hardware systems. However, the ST BLE Toolbox utility is limited to displaying raw hexadecimal data lacking the capability to convert continuous data streams into charts such as the ECG data of this project. Consequently, a custom mobile application was developed to interface with both devices and provide both real-time and a report-like visualization of ECG and SpO_2 waveforms. A primary objective for this development was to ensure a simple, intuitive, and user-friendly interface, for such sake, the application has been developed using **Flutter**.

5.1. The app engine: Flutter

Flutter is a high-performance, open-source framework developed by *Google* for building cross-platform applications using the Dart programming language. Its primary strength lies in its versatility, as it facilitates the seamless development of applications ranging from web platforms to mobile systems (iOS and Android) from a single codebase. The core architecture of a Flutter application is based on the hierarchical arrangement of Widgets, which serve as the fundamental building blocks for the entire visual layout.

In Flutter, everything is treated as a widget, from structural layouts to specific user interface elements such as buttons, icons, sliders, and more. This widget-based approach allows for the creation of highly responsive and customizable interfaces where various complex operations can be triggered directly through user interaction. A critical feature for engineering applications is Flutter's ability to interface with low-level logic; widgets can be configured to execute writable C functions, enabling the application to perform high-performance tasks that might be too computationally intensive for a standard high-level language. This capability ensures that intensive operations, such as real-time calculations, are executed efficiently within the application framework without sacrificing a simple user interaction experience. Furthermore, Flutter's capabilities are extensively augmented by a global community of developers who contribute *packages* (modular libraries) that simplify the integration of advanced features. Consequently, Flutter proved to be a reliable and robust choice for designing a system capable of managing simultaneous BLE communication with the pulsECG and SLVECG devices while maintaining an intuitive and user-friendly interface.

5.2. App organization and design

The user interface has been designed following widely used apps: a modern, minimalist design in user elements and color palette. The resulting interface balances functionality with modernity.

5.2.1. Icon



Figure 92: App icon style.



Figure 93: Final icon result.

5.2.2. Colors

Given the purpose of the app, the chosen color palette is inspired by medical environments and online platforms such as the American Heart Association website. [69]

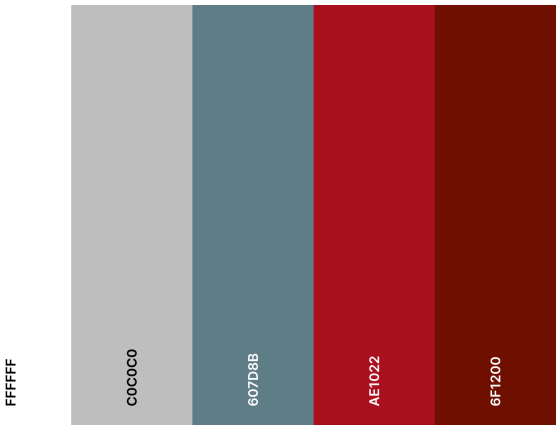


Figure 94: App colors palette. [22]

- White (*0xFFFFF*) is used for the background color, as well as selected icons and the app logo.
- Silver (*0xC0C0C0*) is used for unselected icons in the application menu, visual separators and disconnected devices icon.
- Slate gray (*0x607D8B*) is used for some custom card-like elements, items selection and some minor texts.
- Ruby red (*0xAE1022*) is the dominant color, it creates a simple medical interface fashion for the app layout. It is also used to display ECG leads, important UI elements and texts, connected devices icons and chosen settings.

- Molten Lava (*0x6F1200*) goes around the dominant red color, it is used for titles and card-like elements for vital signs acquisitions, it is meant to give a focused perception on those UI elements creating a deep contrast with white and gray sections.

A minor, yet worth mentioning color is black (*0x00000*) which is used for most of the app guide text for better readability.

5.2.3. Layout

The pulsECG-X App functionalities can be accessed by means of such navigation bars, constantly displayed on the top and bottom part of the screen.
On the top, an Appbar is present, displaying the App logo on the center. A long press restarts the app. On the right, a question mark icon redirects the user to the App guide



Figure 95: Appbar.

The central section of the screen is dedicated to the page content and is potentially scrollable.

On the bottom part of the screen, a navigation bar can be found:



Figure 96: Navigation bar.

Tapping on the leftmost icon opens the Bluetooth Connectivity page, the central icon redirects to the Acquisitions Page/Home Page, whereas tapping on the rightmost one forwards to the Settings page.

5.3. App guide page

To assist the user on the app and devices usage, a detailed guide has been inserted, and it is reachable by tapping on the question mark icon located on the top right of the screen (as shown in Figure 95). The user is welcomed to a “Table of contents” view, as the guide is divided into chapters, a tap on a chapter title redirects the user to that chapter. Each chapter carefully guides the user in discovering each implemented functionality of the app, and instructs to the wearing of devices. Videos are available to give further assistance.

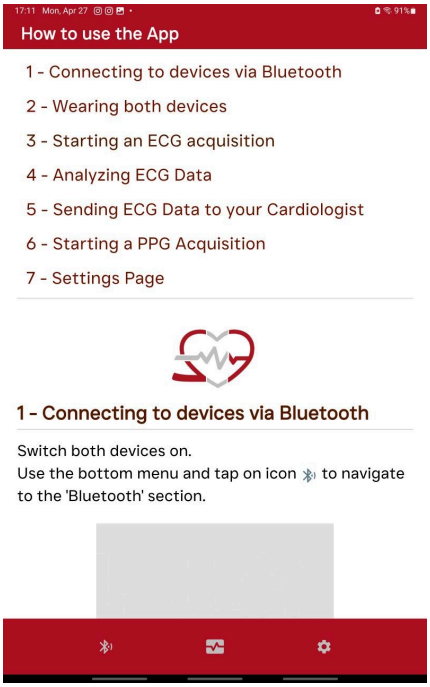


Figure 97: Guide Page Snapshot.

Either a tap on the top left side or on a navigation bar icon allows exiting the guide page.

5.4. Bluetooth Connectivity page

On this page, the application scans for nearby BLE devices, with a major priority for pulsECG and SLVECG devices and a timeout of 30 seconds (the scan can be restarted by tapping the refresh icon, which appears at scan timeout on the page).

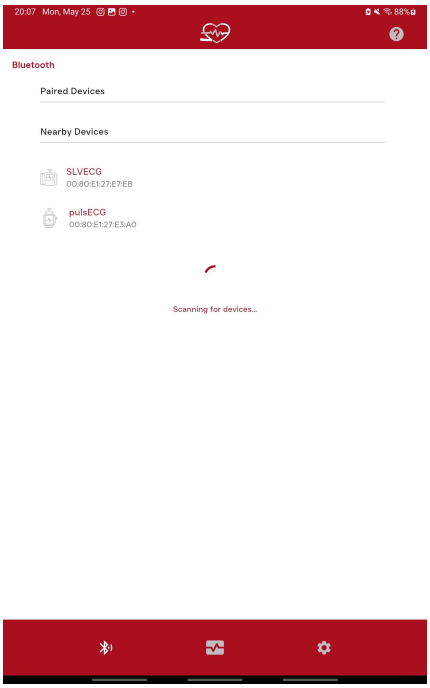


Figure 98: Bluetooth Page, scanning for devices.

When pulsECG is chosen by the user, an *Overlay* appears showing a first connection attempt to the master device.



Figure 99: Connection to pulsECG.



Figure 100: Connection to SLVECG.

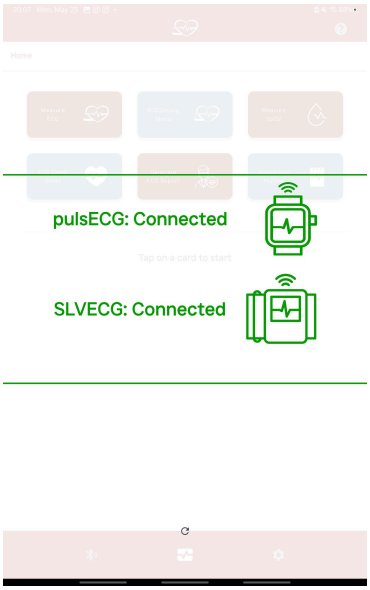


Figure 101: Connection Completed.

If the connection doesn't occur, the App performs a new connection attempt for a maximum of five attempts. If a connection is instead successful, all services and characteristics of the master device are discovered and saved. After that, the App automatically attempts to connect to SLVECG as well, awaring the user by updating the Overlay, thus giving a visual indicator of attempts. When both connections are successfully established, the Overlay disappears, redirecting the user to the Acquisitions page.
At this point, the application acts as a BLE Client, and it has subscribed to both ECG and SpO_2 characteristics; it will receive notifications coming from devices.

5.5. Home Page / Acquisitions page

This page represents the core of the App, as on the top section, a scrollable list of *cards* (a custom *widget*) is present. Each card is tied to specific functions regarding ECG and SpO_2 measurements, which are executable by a simple tap.
The cards view is displayed as an extended grid, as shown in Figure 102 when no function has not yet been selected.

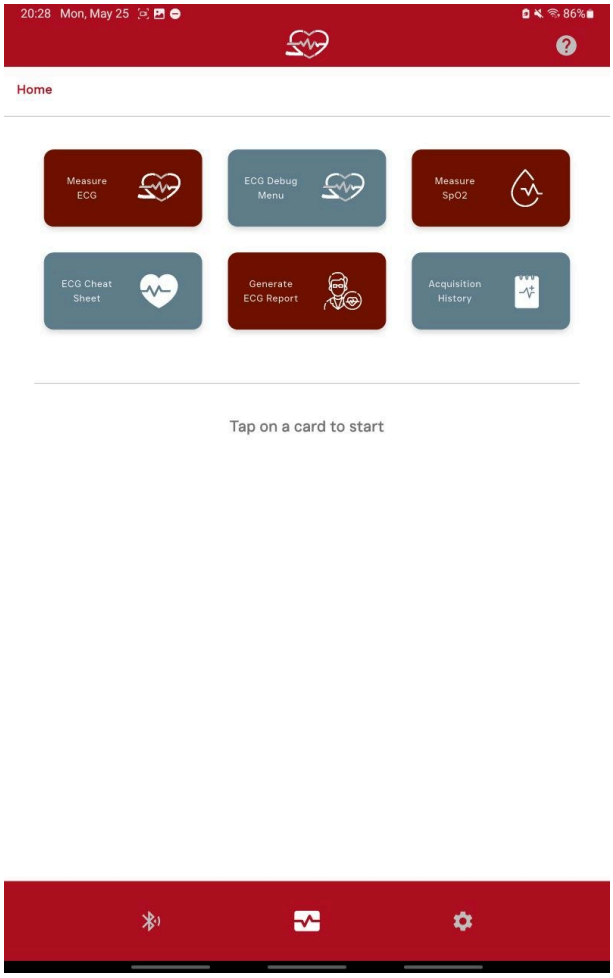


Figure 102: Acquisitions Page, no selected function.

A tap on a card shrinks the card grid to just a row, leaving more room on the central section of the screen to display data and/or charts.

5.5.1. Acquisition of ECG signals

When tapping on the "Measure ECG" card, the user is first reminded to keep a steady position, and a 10-seconds countdown is displayed as illustrated in Figure 103. 5 seconds before the countdown expiration, the application writes '1' on the **CharSS** characteristic for both devices, starting an acquisition. This is done to give enough time for the devices and skin to create a solid contact avoiding motion artefacts as much as possible. During such 5 seconds, sampled values are neither stored or displayed.



Figure 103: Acquisition countdown.

The acquisition lasts *30 seconds* by default. During the acquisition window, the application receives notifications from both devices and starts elaborating them. Each notification involves a certain amount of bytes from the devices, processed iteratively in groups of four bytes. The app decrypts the quartet of bytes following the 32-bit layout seen in Figure 87:

- Each quartet is interpreted as an *unsigned* 32-bit sample, of which the 4 MSBs are used to extract the channel ID where the ADC converted data comes from;
- Extracts the raw 24-bit data from the quartet, sign-extends it to 32 bits again, this sample is already distinguished as a lead I, lead II, or lead V_2 one, and it's copied to the respective *queue* for post-acquisition processing;
- Performs the voltage conversion of the sample:

$$V_{\text{lead sample}} = \text{ADC}_{\text{code}} \times \frac{V_{\text{REF}}}{2^{N_b-1}} \quad \text{where} \quad V_{\text{REF}} = 2.5 \text{ V}, N_b = 24 \tag{20}$$

The previously decscribed processing of received notifications bytes is shown in Figure 104.

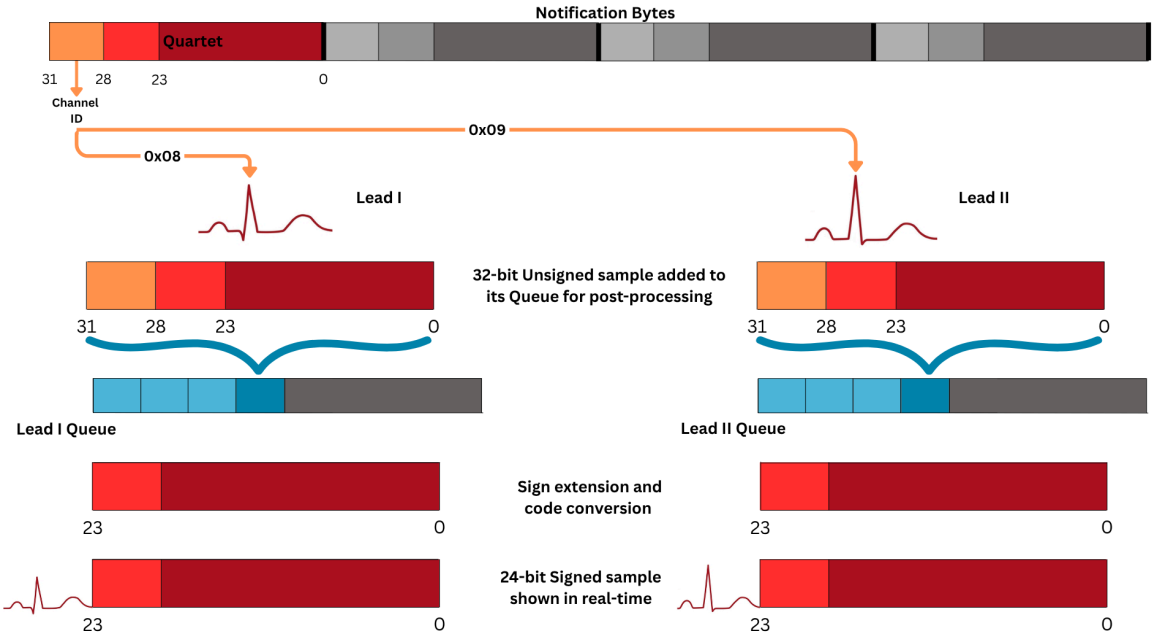


Figure 104: Real-time processing of a received notification, pulsECG device case.

As a result of the processing, real-time ECG leads are displayed on screen during the acquisition, as can be seen in Figure 105. The *ScrollBar* acts as a visual timer, representing an upward counter towards the end of the acquisition; shown leads haven't yet been filtered hence they present some baseline deviations and noise.

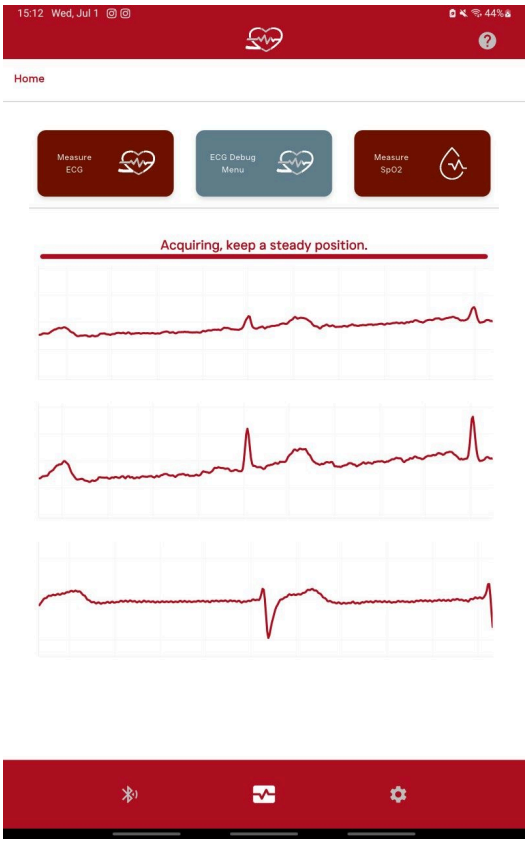


Figure 105: Real-time display of Lead I, Lead II and V_2.

Once the acquisition time window expires, the app writes '0' on both devices *CharSS* and stops listening to notifications until a new acquisition has to be performed. Real-time displays are now hidden to display an Overlay for post-processing.

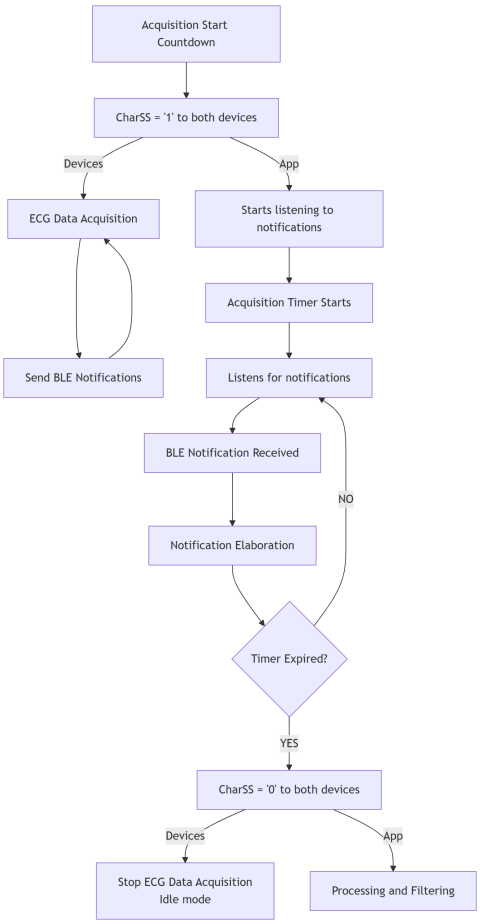


Figure 106: ECG Acquisition workflow, App side.

5.5.1.1. Conversion and Filtering of ECG Signals

At the end of an acquisition, all raw enqueued data is first converted using Equation 20 and then processed by a chain of digital filters to remove the main known sources of disturbance in ECG signals. Via the *Butterworth* package, the following filters are automatically applied:

5.5.1.2. Limb Leads

- Notch Filter: order 3, frequency of 390 Hz, centered window at 50 Hz with a range of 1.5 Hz;
- High-Pass Filter: order 3, frequency of 390 Hz, cut-off frequency of 2 Hz;
- Low-Pass filter: order 2, frequency of 390 Hz, cut-off frequency of 100 Hz;

5.5.1.3. Precordial Leads

- Notch Filter: order 3, frequency of 390 Hz, centered window at 50 Hz with a range of 2 Hz;
- High-Pass Filter: order 3, frequency of 390 Hz, cut-off frequency of 0.05 Hz;
- Low-Pass filter: order 3, frequency of 390 Hz, cut-off frequency of 100 Hz;

For debugging purposes, a long press on the "ECG Debug Menu" card displays filtering settings and FFT analysis of the just-acquired ECG signals. This has been necessary to tune parameters and reapply filtering during the testing phase. The menu shows the amount of acquired samples and the data rate for each channel i.e. lead I data, lead II data and lead V_2 data. Moreover, there's the possibility to edit each filtering stage parameter and see the results, or to revert to the original set of parameters.



Figure 107: ECG Debug Menu.

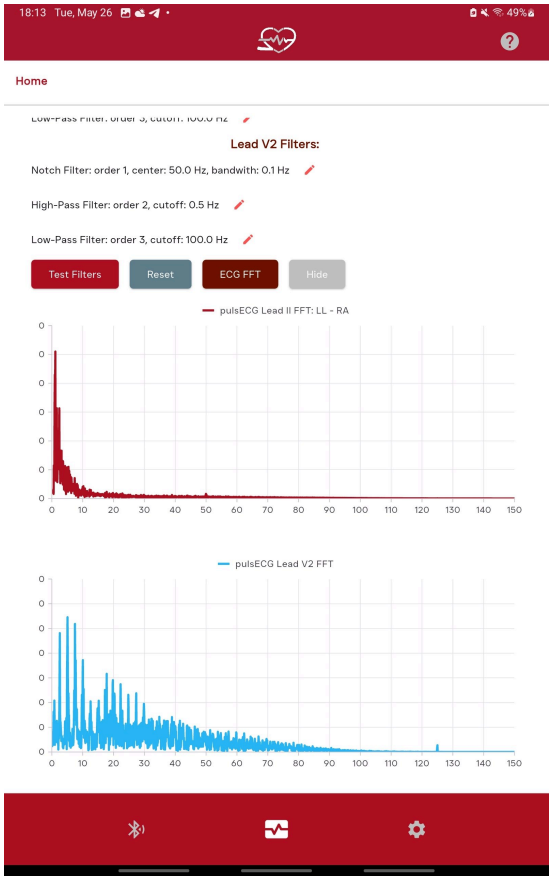


Figure 108: FFT of Lead I and lead V_2.

Once the filtering process for acquired leads has been completed, the App uses them to reconstruct the remaining four leads (III, aVR, aVR, aVF) using Einthoven's Formula, Equation 10, Equation 11 and Equation 12. Reconstructed leads, as a consequence, are intrinsically filtered.

5.5.1.4. Complete Display of ECG Waveforms

Following the filtering stage, the application organizes the cardiac data into a structured interface designed for clinical readability. The first information is the patient's heartbeat, which is followed by the Leads. Each acquired and reconstructed lead is displayed within a specialized Flutter widget called "*ECG Paper*" that replicates the structure of standard ECG grid-like paper.
On the right of the widget, a theoretical reference lead is shown to provide an immediate comparison. The ECG paper widget supports horizontal scrolling, allowing the user to navigate the entire duration of the acquisition. A significant debugging process was required on the insertion of the proper value in the *sampleRateHz* of the widget.
In fact, the sampling frequency of 390 Hz for the MCP3564R is referring to **both** acquisition channels, therefore it has to be halved to properly display the ECG signal. A wrong value leads to horizontally stretched or shrunk ECG waveforms erasing their value.



Figure 109: Acquired ECG signals.



Figure 110: Reconstructed ECG signals.



Figure 111: Reconstructed ECG signals, scrolled view.

5.5.2. ECG Report generation

An additional feature that has been later on added in the application development is the generation of a medical report, containing the last 5 seconds of each ECG Lead from the most recent measurement, as well as basic details on the user (name, sex, age).
Such functionality has been introduced as a tribute to the previous iterations of ECG monitoring apps developed within the Politecnico. On the acquisitions page, the report is automatically generated when tapping on the *Generate ECG Report* card. At generation completion, it is asked to choose where to save the document, so to allow easier access at a second moment. The generated report is a PDF file that can be effortlessly forwarded to the patient's cardiologist, for instance.



Figure 112: First page of a generated ECG Report.

5.5.3. SpO_2 acquisition page

5.5.3.1. Processing logic overview

The SpO_2 measurement starts by activating the "Measure SpO_2" card. Upon initialization of the page, the application issues a command to the Master microcontroller to enable the analog circuitry and enter the PPG acquisition loop. The command is issued by writing into the microcontroller BLE characteristic `CharPPGStart = 1`. Immediately after that, the app enters the acquisition loop, and the microcontroller starts sending BLE payloads with raw PPG data from the Red and Infrared channels. The page features a plot displaying filtered PPG data and readout labels with the measured SpO_2 value, the status of the acquisition, and other metrics, described further in Chapter 5.5.3.4.

Since the displayed information and how the data is processed depend on the received data, a state machine is used to implement the acquisition loop. It encompasses five states discussed in detail in Chapter 5.5.3.5.

5.5.3.2. Filtering

To ensure low-latency visualization of the signal, the acquired samples undergo real-time digital filtering. Because all real-time filters are inherently causal, they introduce a slight phase delay to the underlying waveform. To maintain mathematical coherency between the processed Infrared (IR) and Red channels, an identical filter topology was applied across both channels. This ensures that phase distortion remains identical between channels, which preserves the integrity of the SpO_2 calculation.

The digital signal processing chain utilizes two parallel filtering pipelines. The outputs of both pipelines are preserved in the corresponding buffers until the start of a new acquisition.

5.5.3.2.1. The primary pipeline

The primary pipeline removes the DC baseline wander and high-frequency noise to expose the underlying pulsatile morphology of the PPG. This is achieved by a first-order band-pass filter with cutoff frequencies of 0.5Hz and 7Hz. These frequencies have been chosen due to the human heart rate being in the interval of 30 to 420 bpm. The resulting signal is then displayed on the PPG acquisition page of the smartphone app.

The band-pass filter was implemented as a chain of a first-order high-pass and a first-order low-pass stages. Both stages are implemented as discrete time-domain difference equations:

$$y_{\text{hp}}[n] = \alpha \cdot \big(y_{\text{hp}}[n-1] + x[n] - x[n-1]\big) \tag{21}$$

$$y_{\text{lp1}}[n] = y_{\text{lp1}}[n-1] + \alpha_{\text{lp}} \cdot \big(y_{\text{hp}}[n] - y_{\text{lp1}}[n-1]\big) \tag{22}$$

$$y_{\text{out}}[n] = y_{\text{out}}[n-1] + \alpha_{\text{lp}} \cdot \big(y_{\text{lp1}}[n] - y_{\text{out}}[n-1]\big) \tag{23}$$

where $x[n]$ represents the raw input sample, $y_{\text{hp}}[n]$ and $y_{\text{lp1}}[n]$ are intermediate high-pass and first low-pass outputs, and $y_{\text{out}}[n]$ is the final output displayed within the application user interface.

In these equations, α denotes the smoothing coefficient derived from the cut-off frequency f_c and the sampling interval $\Delta t = \frac{1}{f_s}$:

$$\alpha = \frac{\text{RC}}{\text{RC} + \Delta t}, \quad \text{where} \quad \text{RC} = \frac{1}{2\pi f_c} \tag{24}$$

while low-pass smoothing coefficient α_{lp} is defined as:

$$\alpha_{\text{lp}} = \frac{\Delta t}{\text{RC}_{\text{lp}} + \Delta t}, \quad \text{where} \quad \text{RC}_{\text{lp}} = \frac{1}{2\pi f_{\text{lp}}} \tag{25}$$

The block diagram of the pipeline is reported in Figure 113.

To visualize the effects of the primary pipeline, a dataset comprising both channels was acquired from a test subject. This dataset is designated as the reference dataset and will therefore be utilized consistently across all subsequent visualizations of the filtering effect on the data. The pipeline outputs are plotted in Figure 114.

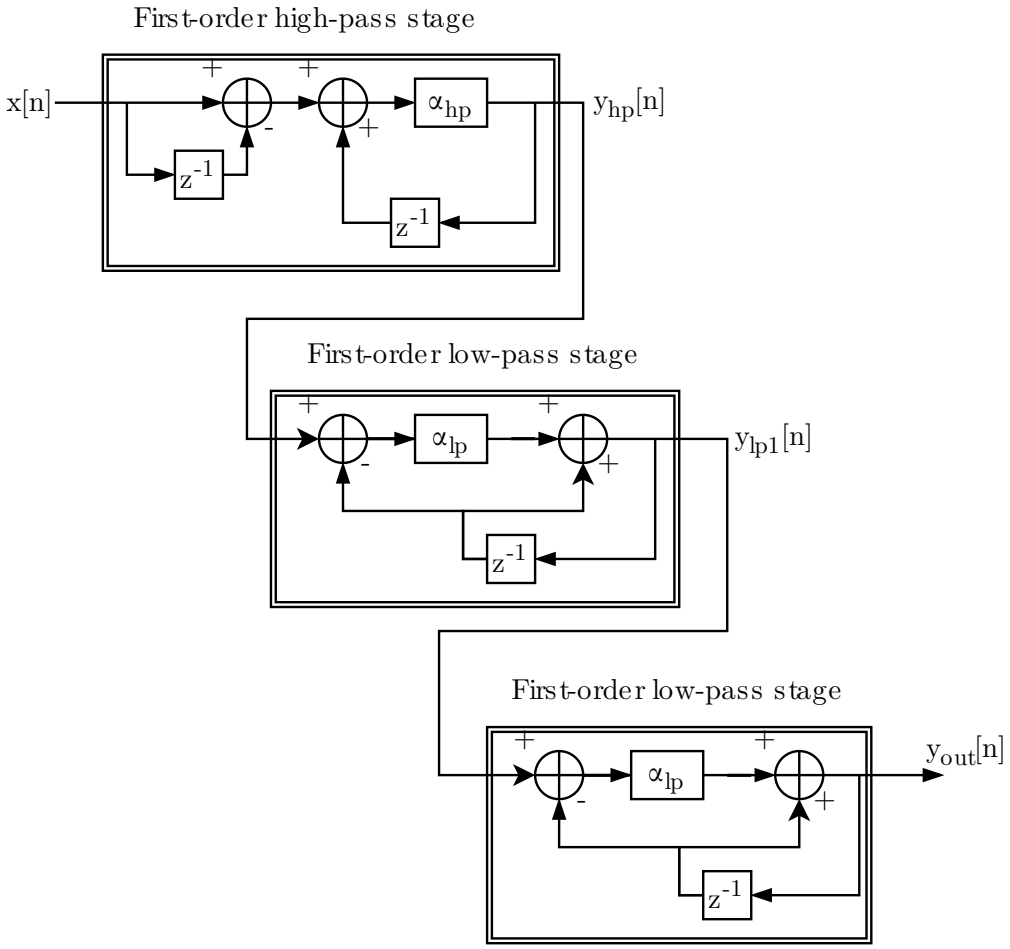


Figure 113: The block diagram of the discrete time-domain filtering of the primary pipeline.

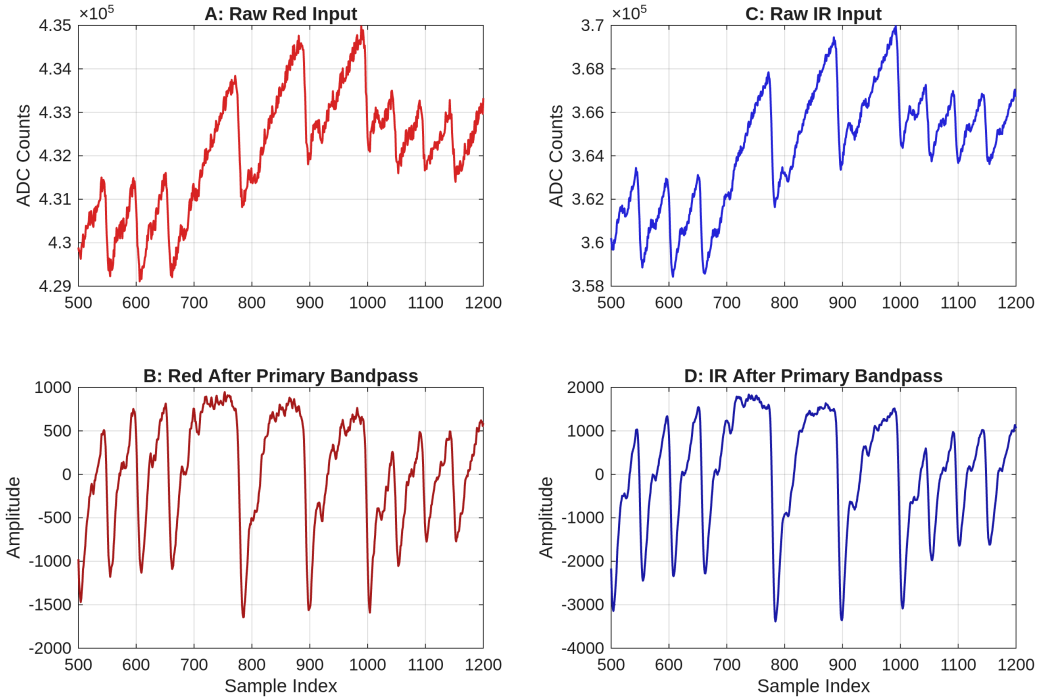


Figure 114: The primary pipeline effect on the Red and Infrared channels. The plot is centered on three extrasystoles, which despite filtering retain morphology of a PPG signal.

5.5.3.2.2. The secondary pipeline

Conversely, the secondary, more complex pipeline isolates and amplifies the post-systolic dicrotic notches (roll-offs) following each cardiac cycle. These emphasized roll-offs are subsequently fed into a peak-and-valley detection algorithm for precise SpO_2 extraction.

This second pipeline is implemented as a cascade combining a fourth-order Butterworth band-pass filter and a moving difference filter, following the methodology proposed by Canac et al. [70]. The band-pass filter was implemented as a cascade of four second-order stages, since the direct usage of eighth-order equations leads to numerical instability due to the finite precision of the digital representation of real numbers. The cutoff frequencies have been chosen to be equal to the ones proposed by Canac et al. [70], which are 0.5 to 10 Hz. The coefficients for the band-pass stages were calculated in MATLAB, using the chosen cutoff and sampling frequencies, and were manually inserted into the Flutter code. The resulting Z-domain transfer functions of each stage are reported below in Equations 26, 27, 28 and 29.

$$H_1(z) = \frac{0.001074 - 0.002148z^{-1} + 0.001074z^{-2}}{1 - 1.382644z^{-1} + 0.493756z^{-2}} \tag{26}$$

$$H_2(z) = \frac{1 + 2.000085z^{-1} + 1.000085z^{-2}}{1 - 1.590511z^{-1} + 0.752160z^{-2}} \tag{27}$$

$$H_3(z) = \frac{1 + 1.999915z^{-1} + 0.999915z^{-2}}{1 - 1.936771z^{-1} + 0.938008z^{-2}} \tag{28}$$

$$H_4(z) = \frac{1 - 2.000000z^{-1} + 1.000000z^{-2}}{1 - 1.977691z^{-1} + 0.978700z^{-2}} \tag{29}$$

Their equivalent linear expressions in time domain are reported in Equations 30, 31, 32 and 33, correspondingly. For each input value $x[n]$ the output value of the realtime band-pass filter is $y_4[n]$ is calculated and then fed into the moving difference filter.

$$\begin{aligned} y_1[n] = 0.001074x[n] - 0.002148x[n-1] + 0.001074x[n-2] \\ +1.382644y_1[n-1] - 0.493756y_1[n-2] \end{aligned} \tag{30}$$

$$y_2[n] = y_1[n] + 2.000085y_1[n-1] + 1.000085y_1[n-2] + 1.590511y_2[n-1] - 0.752160y_2[n-2] \tag{31}$$

$$y_3[n] = y_2[n] + 1.999915y_2[n-1] + 0.999915y_2[n-2] + 1.936771y_3[n-1] - 0.938008y_3[n-2] \tag{32}$$

$$y_{BP} = y_4[n] = y_3[n] - 2.000000y_3[n-1] + 1.000000y_3[n-2] + 1.977691y_4[n-1] - 0.978700y_4[n-2] \tag{33}$$

The moving difference filter performs a subtraction between the current output of the band-pass filter and the delayed output, as seen in Equation 34. The delay, in the equation denoted as w, was chosen to be 12, which corresponds to a 120 ms window with the sampling rate of 100 Sa/s.

$$y_{MD}[n] = y_{BP}[n] - y_{BP}[n-w] \tag{34}$$

The resulting waveform exhibits deep valleys corresponding to the falling edges of the pulsatile component of the PPG. To visualize the dicrotic notch amplification performed by the secondary pipeline, the same dataset of the Figure 114 was used. The morphological isolation of the dicrotic notches is illustrated in Figure 116.

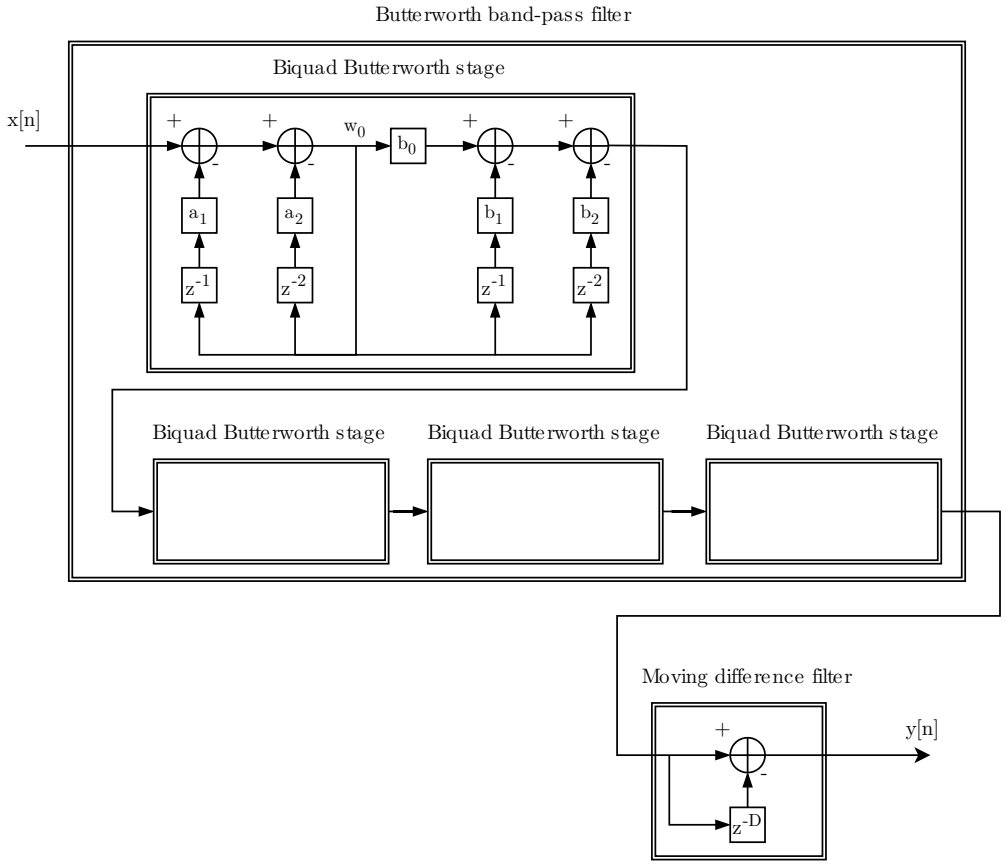


Figure 115: The block diagram of the discrete time-domain filtering of the secondary pipeline. The detailed internal structure is explicitly shown only for the initial biquadratic stage. The subsequent three stages feature an identical schematic topology and differ only by the coefficient values, and are therefore depicted abstractly to preserve visual clarity.

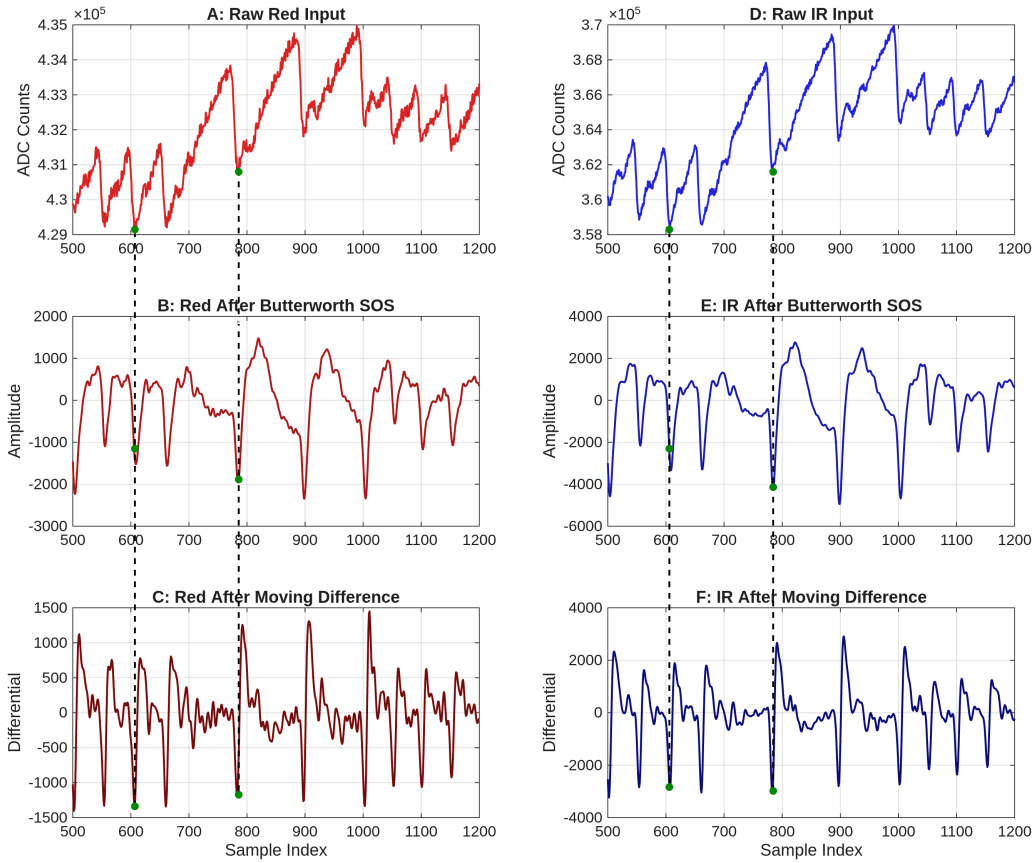


Figure 116: The secondary pipeline effect on the Red and Infrared channels. Two cardiac cycles were chosen to depict correspondence between the valley in the MD-filtered data to the end of the dicrotic notch in the raw data with green circles.

Effect of the filters of the secondary pipeline on the Red (left column, subplots A-C) and Infrared channels (right column, subplots D-F) spanning samples 500-1200. Subplots B and E depict the signals processed by the Butterworth band-pass filter. The MD-filtered data is featured in subplots C and F. The correspondence between the valleys in the MD-filtered data and the dicrotic notches in the raw data is illustrated with a dashed line joining the simultaneous data points across all plots. The specific intersection points between along each dashed line and the plots is highlighted by green circles.

5.5.3.2.3. Moving variance

As it will be seen further, to keep track of the stability of the signal, the variances of the raw signal and of the secondary pipeline output, $y_{\mathrm{MD}}[n]$, are calculated. Moving variance is calculated as

$$s_n^2 = \frac{1}{W-1} M_{2,n} = \frac{1}{W-1} \sum_{i=n-W+1}^{n} (x_i - \mu_n)^2 \tag{35}$$

where $M_{2,n}$ is the square sum of differences between the samples and the mean, W is the length of the sample window on which the variance is calculated, and μ_n is the sliding sample mean and is defined as:

$$\mu_n = \frac{1}{W} \sum_{i=n-W+1}^{n} x_i \tag{36}$$

In order to reduce the computation time and not iterate over all samples in the window at each processing iteration, the algorithm only calculates the effect of the newly added value and the oldest value that is to be removed from the window, which lets us approximate the new variance as

$$s_n^2 = \frac{M_{2,n}}{W-1} = \frac{M_{2,n-1} + (x_n - x_{n-W}) \cdot (x_n + x_{n-W} - \mu_n - \mu_{n-1})}{W-1} \tag{37}$$

$$\mu_n = \mu_{n-1} + \frac{x_n - x_{n-W}}{W} \tag{38}$$

where x_n is the newly added sample and x_{n-W} is the oldest sample.

5.5.3.2.4. Autocorrelation

Autocorrelation is a parameter that quantifies the self-similarity between a signal and a time-shifted version of itself. In the PPG acquisition system, this metric is used to evaluate signal periodicity.

The normalized autocorrelation coefficient $R(L)$ is defined for a time lag L as:

$$R(L) = \frac{\sum_{i=0}^{N-1-L} (x_i - \mu) \cdot (x_{i+L} - \mu)}{\sum_{i=0}^{N-1} (x_i - \mu)^2} \tag{39}$$

where μ represents a mean calculated across a sliding window of length W and L is the lag between the original and shifted signals.

Since frequency of a PPG signal is unknown a priori, the algorithm of autocorrelation calculation, `getBestAutocorrelation`, sweeps L across a predefined range of possible values and finds the specific lag that maximizes autocorrelation. Such L directly corresponds to the period of the cardiac cycle expressed in samples.

The predefined range of possible values is derived from the interval of possible heart rates, assumed to be 40 to 222 bpm, and the sampling frequency of the PPG signal, i.e. 100 Sa/s. The range hence becomes 27 to 150 samples.

Besides the best autocorrelation, the algorithm returns the corresponding sample lag, which indicates the best periodicity, from which the instantaneous heart rate can be derived.

5.5.3.3. Peaks and valleys detection

The work of Canac et al. [70] served as the basis of the current implementation of the peak detection algorithm. To be able to calculate the SpO_2 value, the application scans individual cardiac cycles delimited by dicrotic notches and finds the position of the two valleys and the peak of a particular cardiac cycle. For this algorithm to be simplified, it was assumed that the Red and Infrared signals are synchronized, and hence it is enough to individuate noticeable points of one of the channels only. The Infrared channel was selected as the one to be fed into the peak detection algorithm.

The algorithm is executed at each received couple of samples from the Red and Infrared channels after they were passed through the secondary pipeline of filters. At each iteration, the algorithm checks the current Infrared sample against the latest memorized valley and peak values. If the current sample is found to be bigger that the memorized peak or smaller than the memorized valley, the corresponding noticeable point is overwritten with the index of the current sample. The process continues until the MD-filtered Infrared signal drops below a threshold, which corresponds to a dicrotic notch and denotes the end of cardiac cycle.

Upon the completion of each cardiac cycle, the algorithm extracts the coordinates of the systolic peak and two bounding valleys from the raw Infrared and Red waveforms. These three points form a triangle, as illustrated in Figure 117. The subsequent calculations are adapted from the Maxim Integrated Application Note for reflective pulse oximeter evaluation kit [71]. To isolate the AC and DC components of the waveform, the apex of the triangle is projected vertically onto the opposite side. This geometric projection forms a vertical line, the length of which is the AC component of the PPG for that specific cardiac cycle. Consequently, the DC baseline component is calculated by subtracting the AC magnitude from the raw signal amplitude measured at the triangle's apex.

Mathematically, the application finds the coordinates of the projection of the P1 on the baseline by using parametric vector equations for the baseline V_1V_2 and a unitary line originating from P_1 and going towards the horizontal axis:

$$P_1 + \begin{pmatrix} 0 \\ -1 \end{pmatrix} s = V_1 + (V_2 - V_1)t \quad \Leftrightarrow \quad (V_2 - V_1)t + \begin{pmatrix} 0 \\ 1 \end{pmatrix} s = P_1 - V_1 \tag{40}$$

Which can be rewritten as a first-order linear equation system:

$$\begin{pmatrix} x_{\mathrm{V2}} - x_{\mathrm{V1}} & 0 \\ y_{\mathrm{V2}} - y_{\mathrm{V1}} & 1 \end{pmatrix} \begin{pmatrix} t \\ s \end{pmatrix} = \begin{pmatrix} x_{\mathrm{P1}} - x_{\mathrm{V1}} \\ y_{\mathrm{P1}} - y_{\mathrm{V1}} \end{pmatrix} \tag{41}$$

The linear system is solved for t and s, after which the components are calculated for the Red and Infrared channels as follows:

$$\begin{aligned} \mathrm{AC} &= s \\ \mathrm{DC} &= y_{\mathrm{V1}} + (y_{\mathrm{V2}} - y_{\mathrm{V1}})t \end{aligned} \tag{42}$$

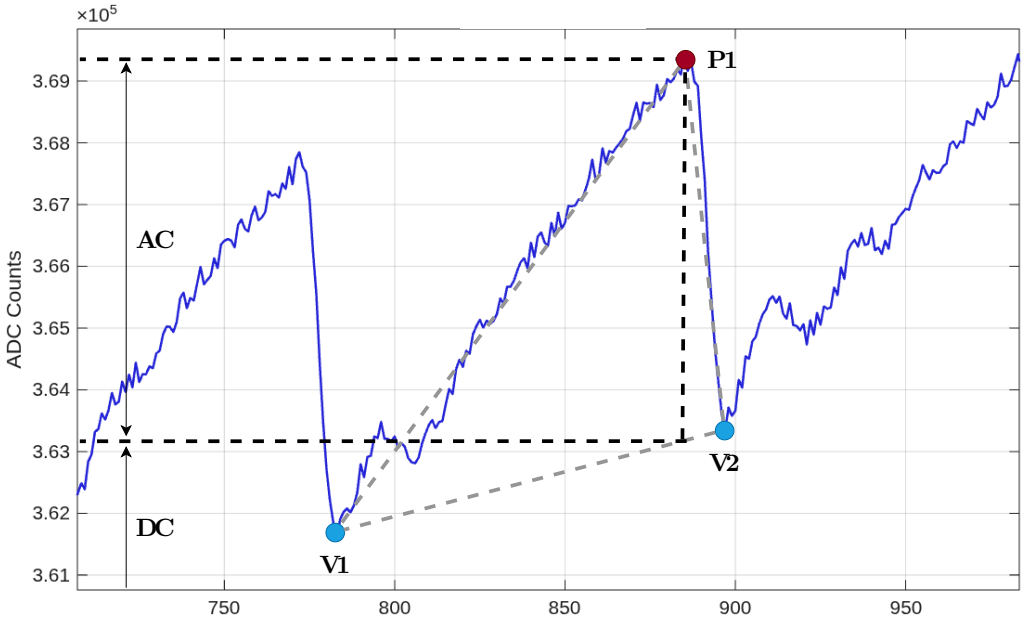


Figure 117: Triangular structure of the Infrared waveform with the identified bounding valleys (V_1, V_2) and the systolic peak (P_1) for a single cardiac cycle from the reference dataset. The vertical projection of the P1 onto the baseline V_1V_2 defines the magnitude of the AC component of the waveform. The DC component magnitude corresponds to the Y-coordinate of the projected point.

After that, the value known as ratio of ratios is calculated using Equation 4.

The peripheral oxygen saturation is subsequently derived from this ratio using the empirical second-order polynomial model used by Analog Devices technical articles [72]:

$$\mathrm{SpO}_2 = aR^2 + bR + c \tag{43}$$

where a, b and c denote calibration constants. The constants were calibrated by acquiring R values with test subjects in varying conditions and measuring SpO_2 with a pulse oximeter reported in Figure 118. After accumulating more samples, the R values were fit to a parabolic curve using linear least square regression. The resulting coefficients are reported below.

$$\begin{aligned} a &= 19.48 \\ b &= -23.38 \\ c &= 102.8 \end{aligned} \tag{44}$$

Finally, the latest peak and valley indices and the newly calculated SpO_2 values are saved into the corresponding buffers, after which the temporary variables are cleared to prepare for the next cardiac cycle processing.



Figure 118: Pulse oximeter used for the SpO_2 curve coefficients calibration. [23]

5.5.3.4. Results visualization

The PPG page displays the following metrics: SpO_2, heart rate, instantaneous autocorrelation and signal stability, as seen in Figure 120.

The SpO_2 label is refreshed each time a new SpO_2 value is calculated and pushed to the buffer. The value displayed on the label is derived each time from R using the parabolic Equation 43. For the R calculation, 10% trimmed means of the components AC_{RED}, DC_{RED}, AC_{IR} and DC_{IR} are used. Such trimmed mean is calculated by ordering the values and discarding the smallest and the biggest fraction of the values, which eliminates artifacts from the dataset that may arise from irregularities in the PPG waveform, such as motion artifacts or occasional ambient light noise that the sensor fails to cancel out.

The heart rate label is updated together with the SpO_2 label and is derived from 20% trimmed mean of the saved period values.

The autocorrelation label serves as signal quality index: when its value descends below 0.5, the signal is assumed to be too unstable to be used for SpO_2 calculation, and the AC and DC components of the Red and IR signals obtained under such condition will not be processed. The label shows a red cross value when low autocorrelation is detected to inform the user of bad signal quality.

The signal stability is used as another signal quality index and is calculated as standard deviation of the MD-filtered signal. For a stable IR signal acquired at wrist, the standard deviation is low and stays in range of 10-30. Big variations of the signal caused by motion artifacts or due to the filters settling lead to the variation increasing by several orders of magnitude. For comprehension purposes, the standard deviation values are mapped onto 0% to 100% range, with 0% corresponding to infinite standard deviation and 100% corresponding to zero standard deviation, using the empirically derived equation Equation 45. With such mapping, the signal quality is bigger than 90% for stable IR signal acquired at wrist. The mapping is represented graphically in Figure 119. It is worth noting that by itself, low signal stability does not lead to the calculations being discarded to leave the possibility of index finger measurements, which naturally lead to much bigger standard deviation even for a stable signal, as the signal amplitude itself is much bigger.

$$\text{Signal Stability} = 100 \times \text{clip}\left(1 - \frac{\log_{10}(n) - 1}{4.30103}, 0, 1\right) \tag{45}$$

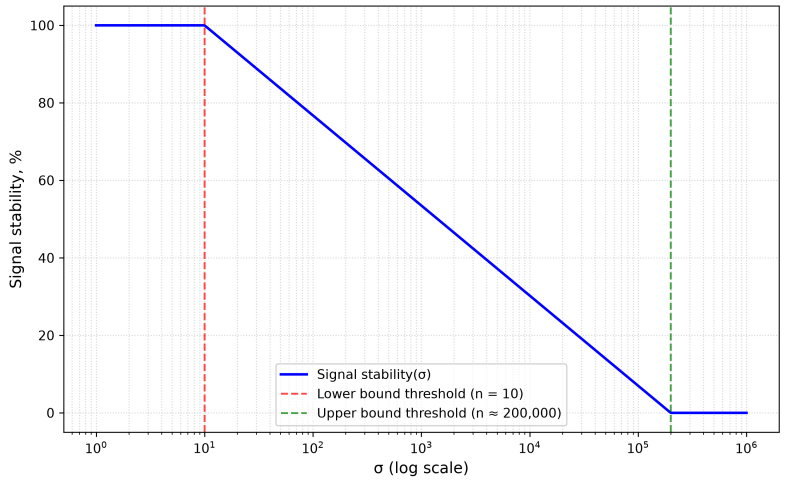
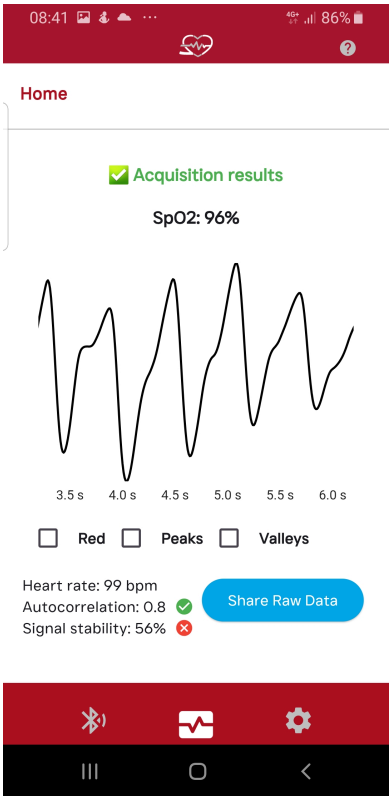


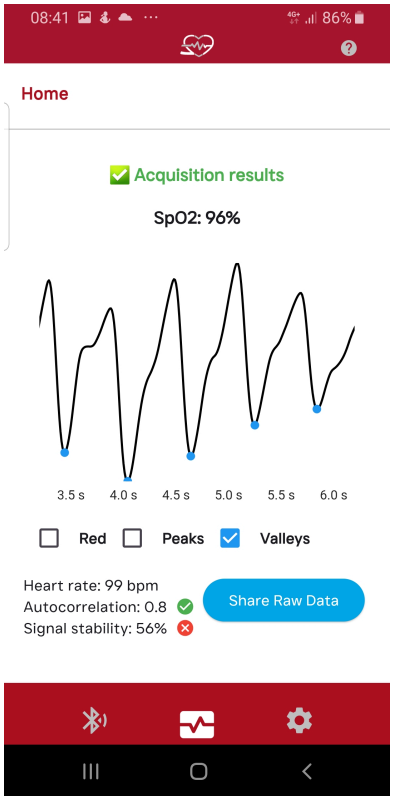
Figure 119: Mapping from the standard deviation of the IR signal into the signal stability parameter.

Besides the numerical metrics, the results page displays the real-time plot of the acquired IR and Red signals filtered with the bandpass filter of the primary pipeline. The plot also features the detected peaks and valleys. The blue and orange colors are associated to the valleys and peaks, respectively. All components of the plot besides the IR signal may be turned off at any moment, which is demonstrated in Figure 120.

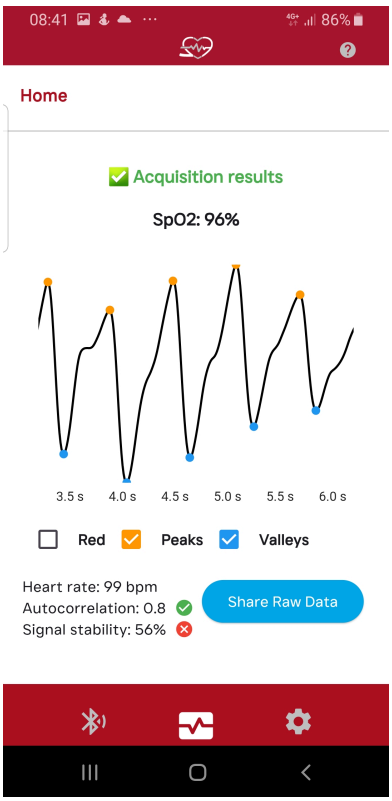
The acquisition results can be exported using the corresponding button. Upon activation, `void exportData()` method is invoked, which compiles raw data in a .csv file and opens a system dialog to choose file share destination.



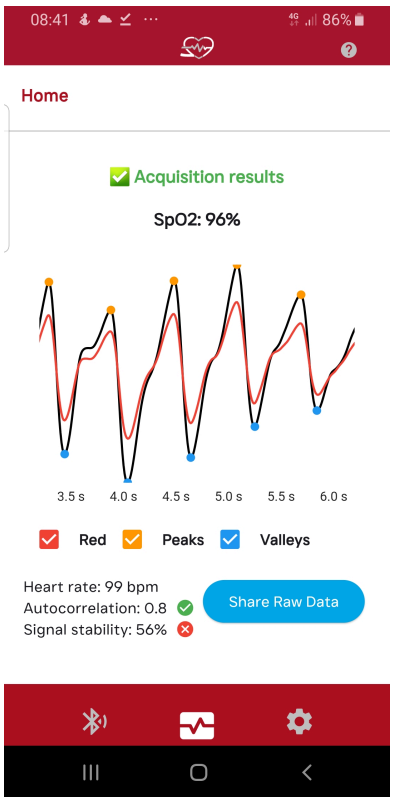
(a) PPG page with only IR signal plotted



(b) PPG page with IR signal and valleys plotted



(c) PPG page with IR signal, valleys and peaks plotted



(d) PPG page with IR signal, its valleys and peaks, and Red signal plotted

Figure 120: Results page with various combinations of active plot options. Due to the signals being bandpass-filtered, they appear superimposed due to the baseline being removed.

5.5.3.5. Finite State Machine implementation

The acquisition is split in several stages, because the sensor requires time to calibrate the ALC algorithm, and the filters need to settle before they start producing stable results on the output. The transitions between the states is controlled by a time-triggered Mealy FSM, whose state diagram is reported in Figure 121.

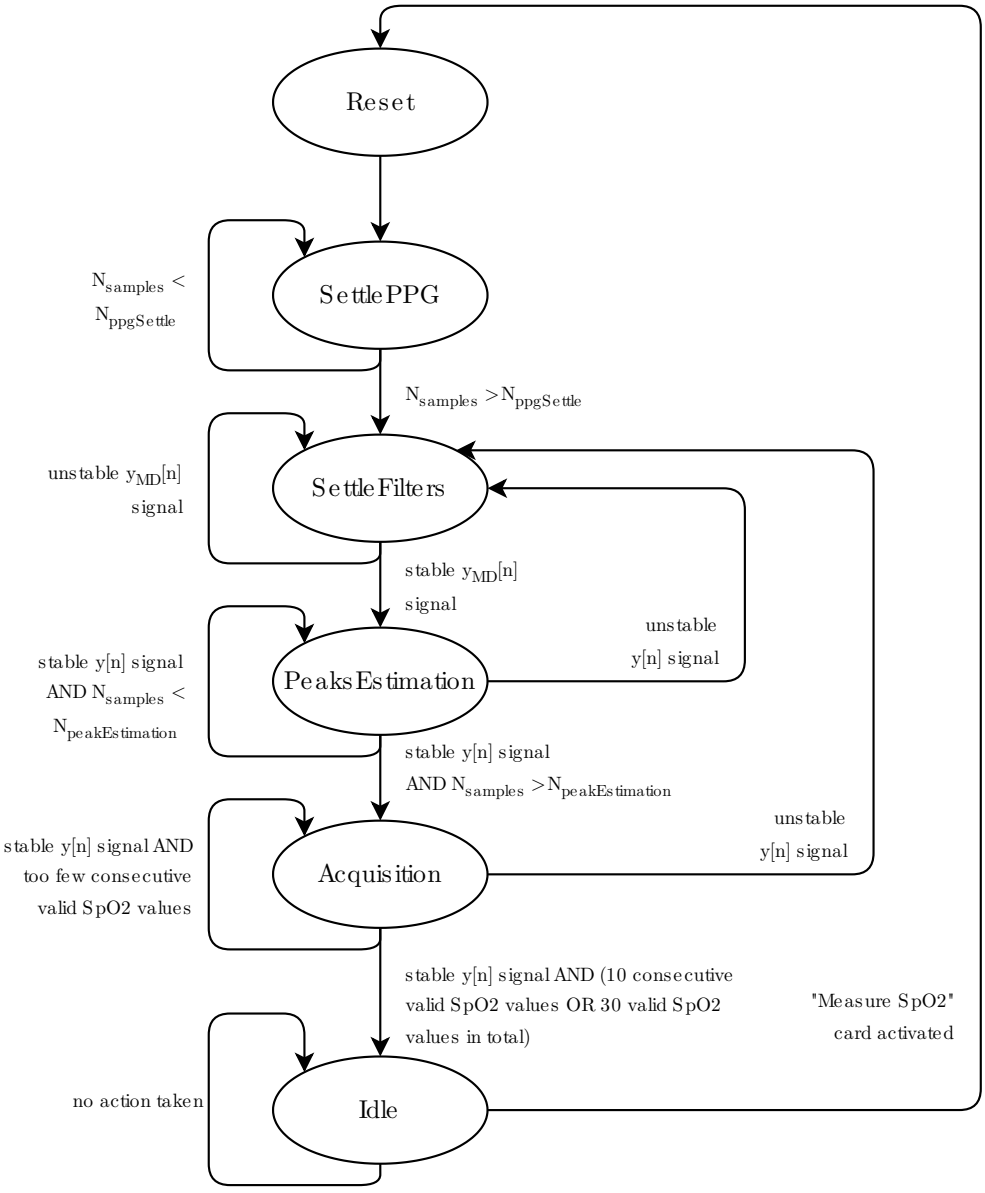


Figure 121: The diagram of the FSM governing the signal acquisition.

The time-triggered FSM was chosen over various alternatives for its compatibility with the Flutter structure of the application, which lacks the main loop and executes everything asynchronously instead, and it allows for very deterministic output due to state transitions being well-defined.

For the FSM to be time-triggered and asynchronous, it was implemented as a function executed by a timer each 50 ms. The function checks the current state and the current outputs and decides whether to evolve into another state or to remain in the current one.

5.5.3.6. Reset state

The sole purpose of the Reset state is to clear all variables employed in the signal acquisition. After that, the machine unconditionally transitions to SettlePPG state.

5.5.3.7. SettlePPG state

Within this state, the machine counts and discards incoming samples until the internal counter reaches a threshold value $N_{\text{ppgSettle}} = 160$. At the beginning of the acquisition, a high-amplitude spike occurs on the raw readings, caused by the user adjusting the physical sensor position. Moreover, the ALC algorithm and the on-board sigma-delta ADC are both memory-dependent systems, the output of which depends on the previous inputs. Therefore, this initial spike causes a transient response on the sensor's output, requiring some settling period to decay. Experimental validation indicated that a 160-sample truncation window is sufficient to make the effect of the initial sensor movement negligible. After this threshold is reached, the machine transitions to the SettleFilters state.

5.5.3.8. SettleFilters state

At each iteration of this state, all incoming samples stored in the queues are processed by the filters, after which the buffers are cleared. Each pair of Red and Infrared values is fed into the both filter pipelines discussed previously. Since the filters used for the PPG signal are memory-dependent, and since their internal variables are initialized to zeros for the ability to process the signal in real time, the output will undergo a transient. The transient will be considered extinguished when the standard deviation of the last 100 $y_{\text{MD}}[n]$ outputs varies by less than 2%, a threshold value established experimentally.

After the filters are stabilized, the FSM evolves into the PeaksEstimation state.

5.5.3.9. PeaksEstimation state

Starting from the PeaksEstimation state, the output of the primary filter pipeline starts being plotted on screen. At each iteration of this state, a constant amount of samples is popped from the Red and Infrared queues and is fed into the filter pipelines. The restriction on the amount of samples to be processed in one iteration arises from the fact that the same timer governing the FSM also causes the real-time PPG plot to refresh, and for the plot to move smoothly it is necessary to plot the exact amount of samples that arrives between two consecutive iterations of the timer.

The delta of samples that provides the maximal smoothiness of the real-time plotting and guarantees that the samples do not accumulate in the queues was calculated as in Equation 46.

$$\Delta N = \Delta T_{\text{timer}} \times \frac{f_{\text{SR}}}{\text{SMP_AVE}} = 50 \text{ ms} \times \frac{400 \text{ Sa/s}}{4} = 5 \text{ Samples} \tag{46}$$

To ensure the samples queue is emptied by the next BLE payload arrival, the actual amount of processed samples in a timer iteration was increased and set to 6.

In this state, the FSM uses an algorithm proposed by Canac et al. [70] to calculate the initial threshold for the dicroting nothes detection on the MD-filtered Infrared signal. Since the threshold is not known yet, the peaks and valleys detection algorithm is not engaged in this state.

At each processed Red and Infrared pair, the standard deviation of the raw signal is calculated. When a sudden movement of the user or other noise makes the standard deviation change at high rate, the FSM falls back into the SettleFilters state and waits for the transient on the filters output to extinguish.

As soon as a critical amount of samples, $N_{\text{peakEstimation}}$, has been acquired in this state, the system transitions into the Acquisition state.

5.5.3.10. Acquisition state

In this state, the incoming data is processed similarly to the PeaksEstimation state, but the peaks and valleys detection algorithm is executed. The detected critical points along with the DC and AC components of the Red and IR signals are saved into buffers under condition that the instantaneous

autocorrelation is bigger than 0.5, meaning that the signal is periodic with well-pronouced periods. The SpO_2 value is calculated as per Chapter 5.5.3.4. The PPG page in the Acquisition state is seen in Figure 122.

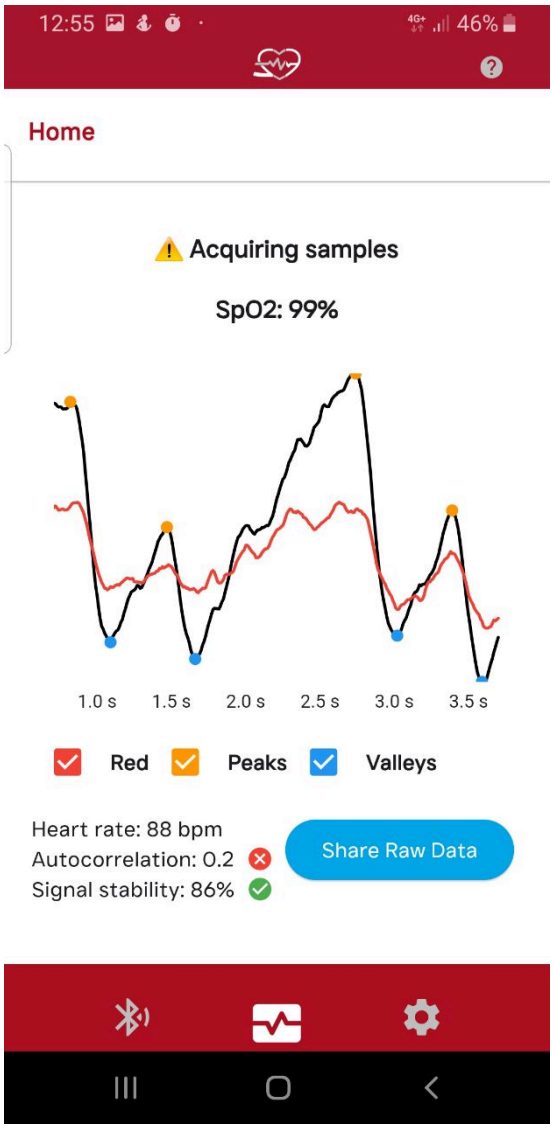


Figure 122: The PPG page when FSM is in the Acquisition state.

If the raw signal becomes too unstable, i.e. the Infrared standard deviation changes at more than 2% rate, the FSM falls back into the SettleFilters state.

As soon as 10 consecutive valid SpO_2 samples are acquired, the acquisition is considered finished, and the FSM transitions to the Idle state. if the device fails to detect 10 consecutive valid samples, it counts up to 30 valid samples and stops the acquisition, displaying the results nonetheless.

5.5.3.11. Idle state

Upon transition to the Idle state, the application sends a BLE command for the Master microcontroller to turn off the analog circuitry. No samples arrive to the application, and the plot remains frozen but scrollable to let the user explore the waveform.

The timer that triggered the FSM execution is stopped. To start a new acquisition and activate the FSM again, the user has to press the “Measure SpO_2” card again.

5.6. Devices settings page

The settings page is organized to firstly show both devices battery percentage, which is fetched every time the user accesses the page or by tapping on the refresh icon if both devices are connected. In addition, the acquisition duration for ECG signals can be adjusted to either predefined amounts or a different one by means of a circular selector, as well as the preferred leads to be shown in real time during the acquisition, from just one lead to all of them. Furthermore, the user can insert their full name, sex and age, for the previously presented *Generate ECG Report* feature.

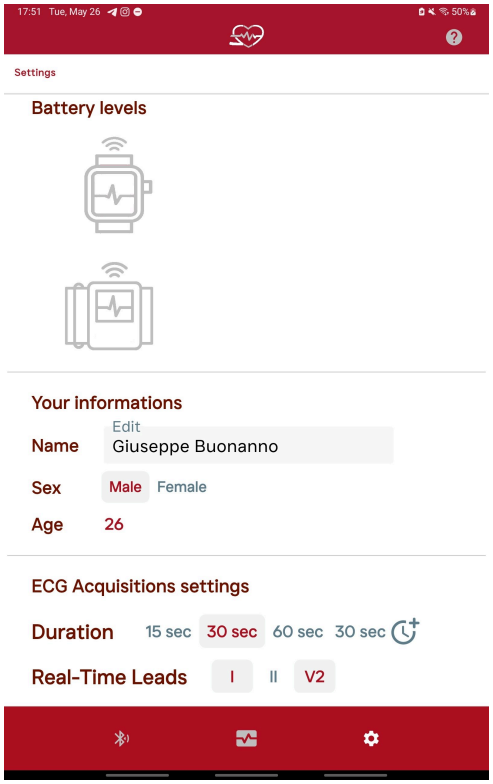


Figure 123: Settings Page: both devices disconnected.

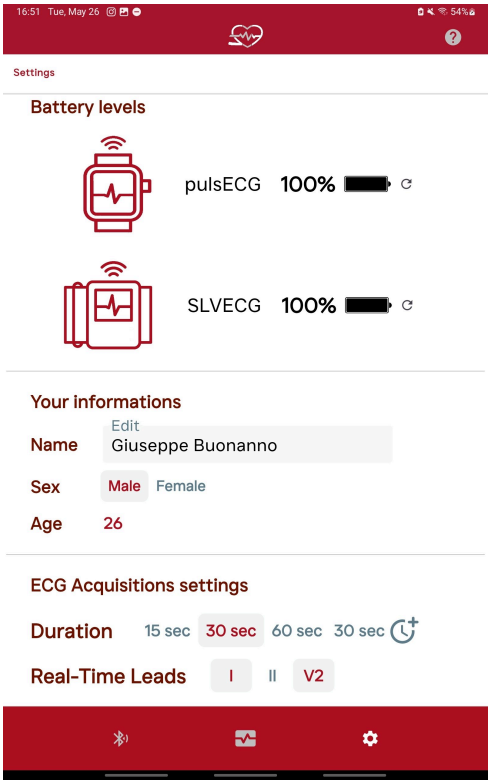


Figure 124: Settings Page: both devices connected.

5.6.1. Computation of the battery percentage

In order to retrieve the battery percentage for both devices, it has been necessary to configure the internal ADC of the STM32WB30, which is responsible for reading the voltage of the battery. However, being the battery voltages range between 3.3 V and 4.2 V and the microcontroller ADC reference voltage of 3.3 V, a voltage divider has been implemented to scale down the battery voltage to a readable range for the ADC.

Chosen resistor values for the voltage divider are 10 MΩ, thus the voltage at the ADC input can be calculated as:

$$B_{\text{code}} = V_{\text{battery}} \times \left(\frac{10M\Omega}{10M\Omega + 10M\Omega} \right) \tag{47}$$

On the App side, sending a *read* command to both devices on the **CharB** characteristic triggers an ADC battery level reading, forwarding the converted value to the App via BLE. To give an intuitive display of the battery percentage following other consumer eletronic devices, like in Figure 124, a mapping of percentages has been introced, where 100 % is mapped to 4.2 V and 0 % to 3.5 V. The mapping is performed using a *Lookup Table* shown in Table 31.

Table 31: Battery Level Lookup Table.

ADC Code	Voltage (V)	Percentage (%)
101	4.30	100
98	4.18	100
97	4.14	95
96	4.10	90
94	4.02	80
93	3.97	70
92	3.92	65
91	3.89	60
90	3.84	50
89	3.80	40
88	3.77	35
86	3.70	20
84	3.65	10
82	3.50	0

Each element in the Lookup table has three fields: the battery level code, the corresponding voltage and the corresponding percentage:

$$\mathrm{LUT}_{[\text{code, volt, \%}]} \tag{48}$$

Therefore, to give a percentage value for a received battery level code, the app iteratively checks the LUT entries to find the right one. If the received battery level exceeds the upper and lower bounds of the table, it is automatically clamped to the maximum or minimum battery percentage, respectively.
. Additionally, if the received code lies between two entries $\mathrm{LUT}_{[i]}$ and $\mathrm{LUT}_{[i+1]}$ then the intermediate values are interpolated:
:

$$B_{\text{avg,code}} = \frac{B_{\text{code}} - \mathrm{LUT}_{[\text{i,code}]}}{\mathrm{LUT}_{[\text{i+1, code}]} - \mathrm{LUT}_{[\text{i, code}]}} \tag{49}$$

$$B_{\text{avg,volt}} = \mathrm{LUT}_{[\text{i, volt}]} + B_{\text{avg,code}} \times \left(\mathrm{LUT}_{[\text{i+1, volt}]} - \mathrm{LUT}_{[\text{i, volt}]}\right) \tag{50}$$

$$B_{\text{avg,\%}} = \mathrm{LUT}_{[\text{i, \%}]} + B_{\text{avg,code}} \times \left(\mathrm{LUT}_{[\text{i+1, \%}]} - \mathrm{LUT}_{[\text{i, \%}]}\right) \tag{51}$$

This has been implemented to give a more accurate battery percentage value, as the mapping of 100 % to 4.2 V and 0 % to 3.5 V is not linear.

Chapter 6

Testing and Results

This chapter reports the results of pulsECG and SLVECG acquisitions performed on several **participants of the research team** within the Politecnico members of the Neuronica Lab, with a varying age, sex and lifestyle. During the testing phase of both prototypes, the copper electrodes were a significant bottleneck for a proper ECG acquisition. Volunteers had a different skin composition that didn't allow electrodes placement on the same point, some reported skin irritation after prolonged contact with copper electrodes leading to a signal quality degradation after multiple uses, showing even a color change due to oxidation For such reason, substituting the copper electrodes with more comfortable and skin-friendly materials, such as silver/silver chloride ($Ag/AgCl$) electrodes, enhanced the quality of ECG signals acquisition by reducing noise and ensuring better skin contact. These electrodes are widely used in medical applications for their superior conductivity and reduced skin irritation. Such electrodes perform better when slightly wet with a conductive gel. For the testing phase, a homemade gel has been created using aloe vera and kitchen salt, in 3:1 proportions. It prepared volunteers skin for an acquisition.



Figure 125: Ag/AgCl electrode. [24]

The following results for ECG measurements are organized in columns: on the **left** the acquisition with **copper** electrodes whereas on the **right** ***AgCl*** electrodes acquisitions.

6.0.1. Participant 1: Male, 26 years old

This Participant is not affected by heart diseases. Follows an active lifestyle.

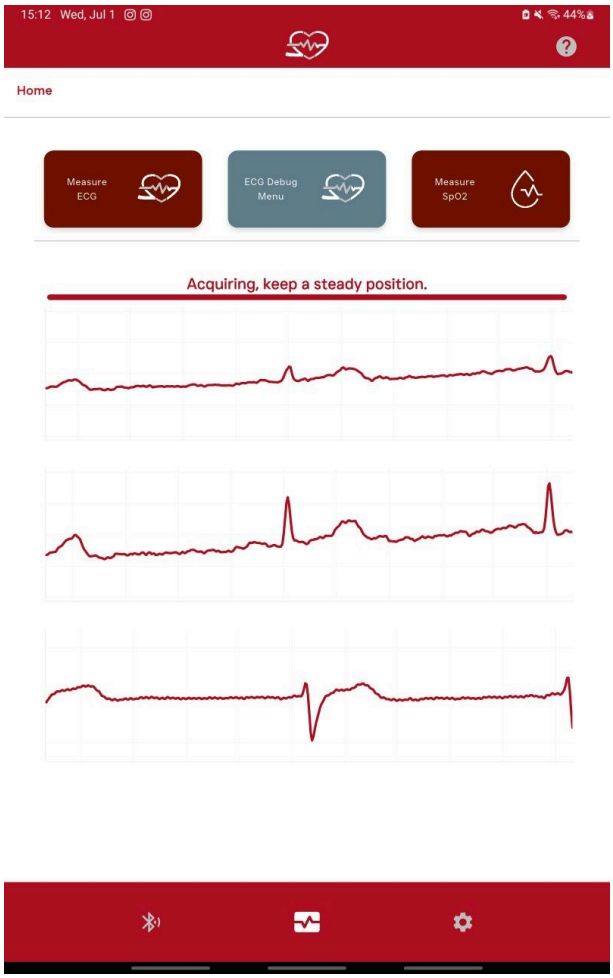
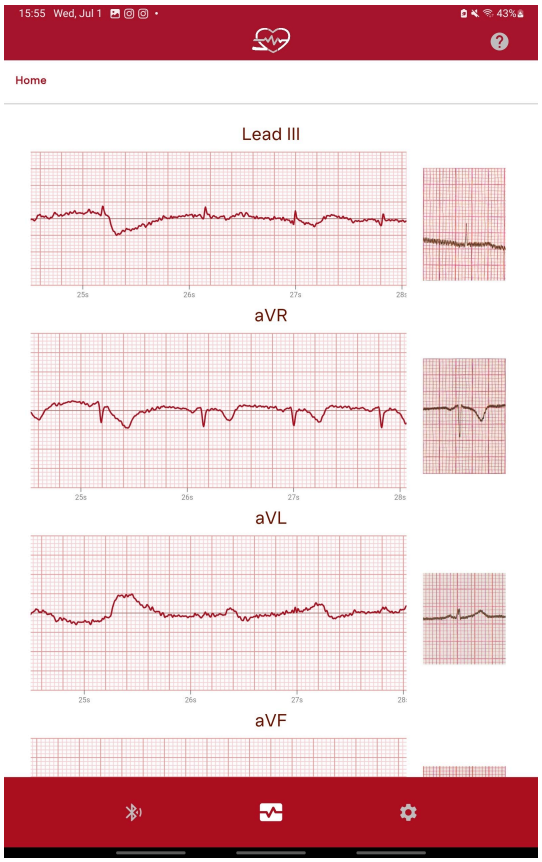
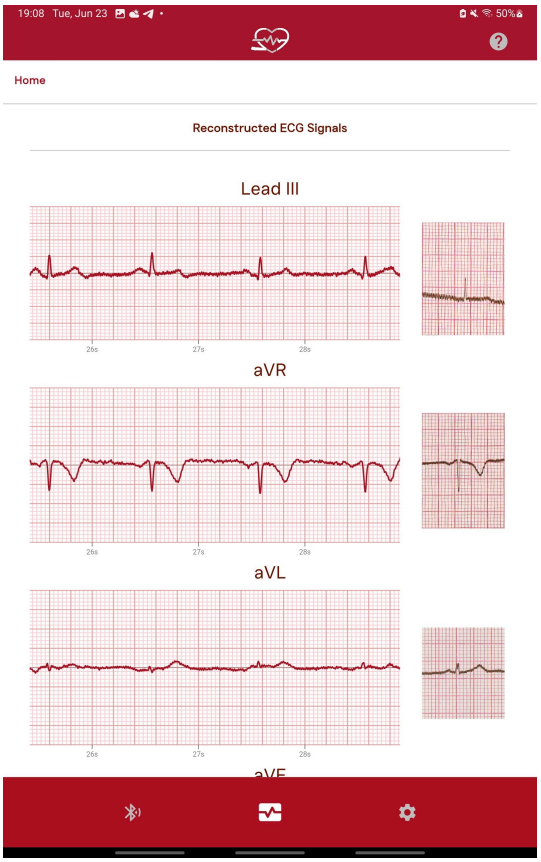


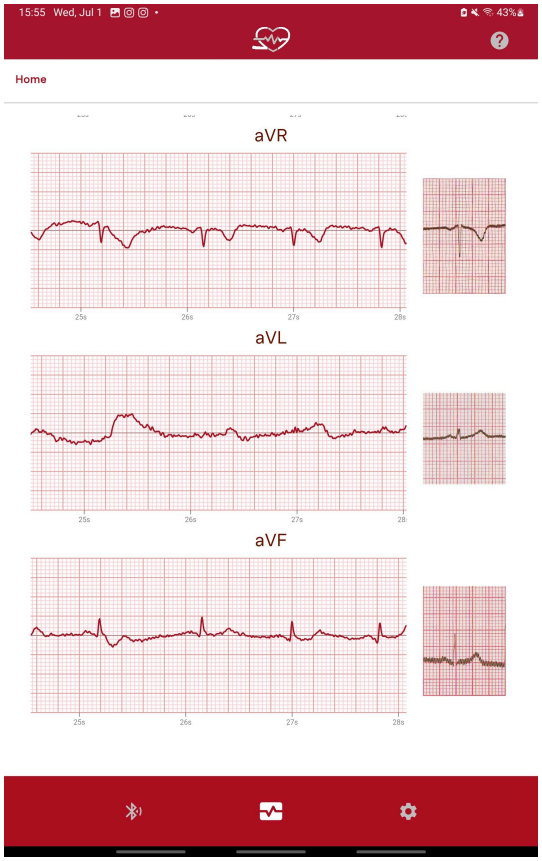
Figure 126: Real-time acquisition.

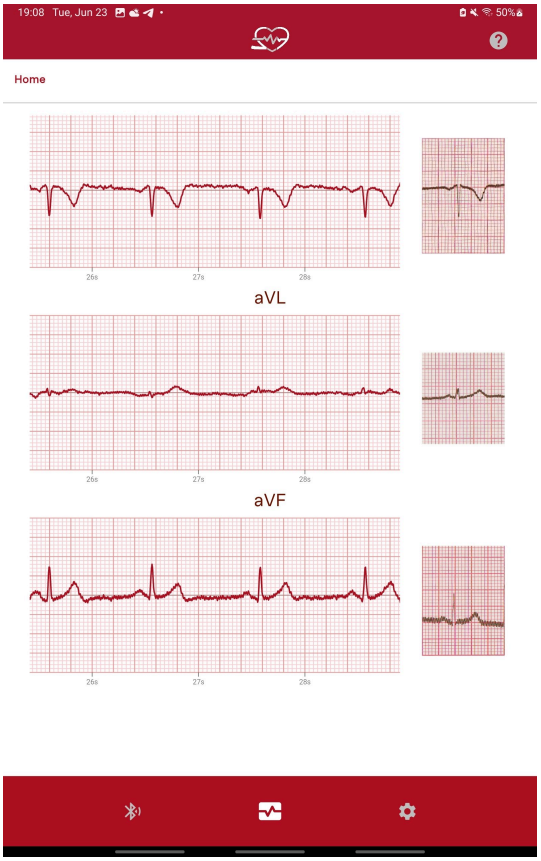

15:55 Wed, Jul 1
43%
Home
Heart Rate: 97 bpm
Lead I
Lead II
V2


19:08 Tue, Jun 23
50%
Home
Measured ECG Signals
Heart Rate: 69 bpm
Lead I
Lead II
V2


15:55 Wed, Jul 1
43%
Home
Lead III
aVR
aVL
aVF


19:08 Tue, Jun 23
50%
Home
Reconstructed ECG Signals
Lead III
aVR
aVL


15:55 Wed, Jul 1
43%
Home
aVR
25s
26s
27s
28s
aVL
25s
26s
27s
aVF
25s
26s
27s
28s


19:08 Tue, Jun 23
50%
Home
26s
27s
28s
aVL
26s
27s
28s
aVF
26s
27s
28s

6.0.2. Participant 2: Female, 25 years old

This Participant is affected by extrasystole.

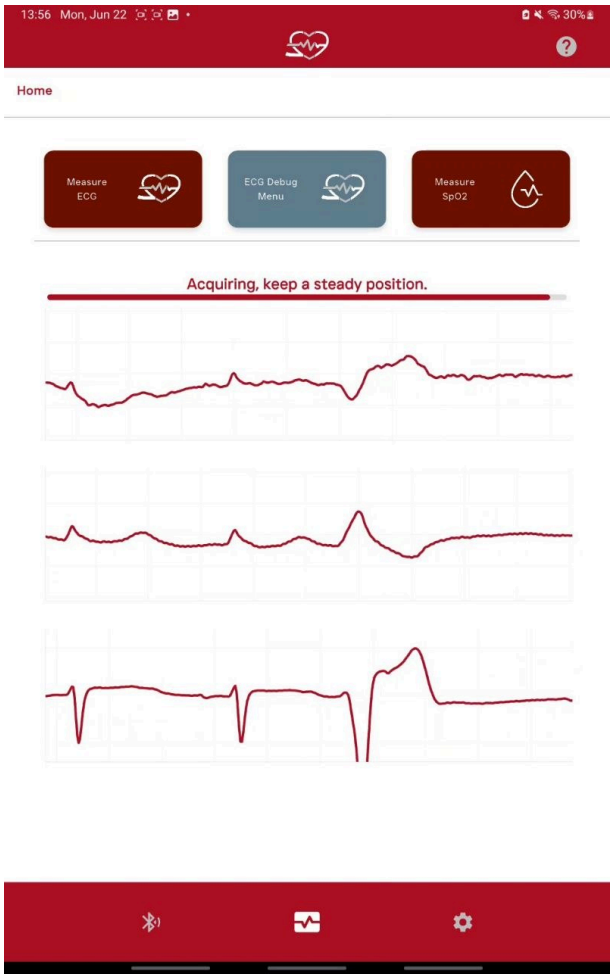


Figure 127: Extrasystole in real-time acquisition.


15:58 Wed, Jul 1
43%
Home
Heart Rate: 85 bpm
Lead I
Lead II
V2


15:25 Wed, Jul 1
44%
Home
Heart Rate: 88 bpm
Lead I
Lead II
V2


15:58 Wed, Jul 1
43%
Home
Lead III
aVR
aVL
aVF

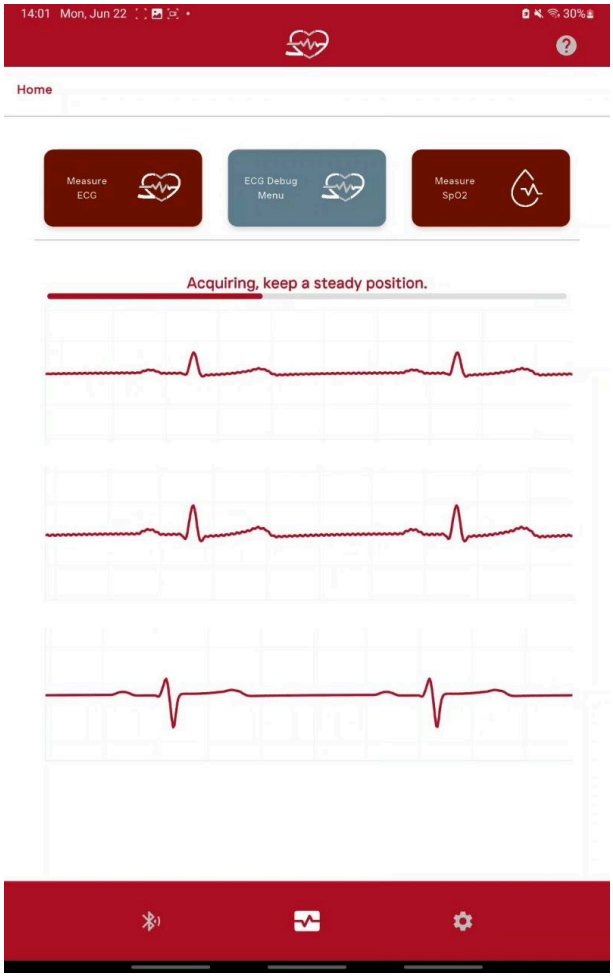

15:25 Wed, Jul 1
44%
Home
Lead III
aVR
aVL
aVF


15:58 Wed, Jul 1
43%
Home
aVL
aVF
18s
19s
20s
21s


15:25 Wed, Jul 1
44%
Home
aVL
aVF
27s
28s
29s

6.0.3. Participant 3: Fluke ProSim 3[1]

The usage of the Fluke ProSim 3 has been useful for various tests with initial and final prototypes, with the same default settings and a heartbeat of 60 bpm.






17:13 Fri, May 29
69%
Home
Reconstructed ECG Signals
Lead III
aVR
aVL
26s
27s
28s

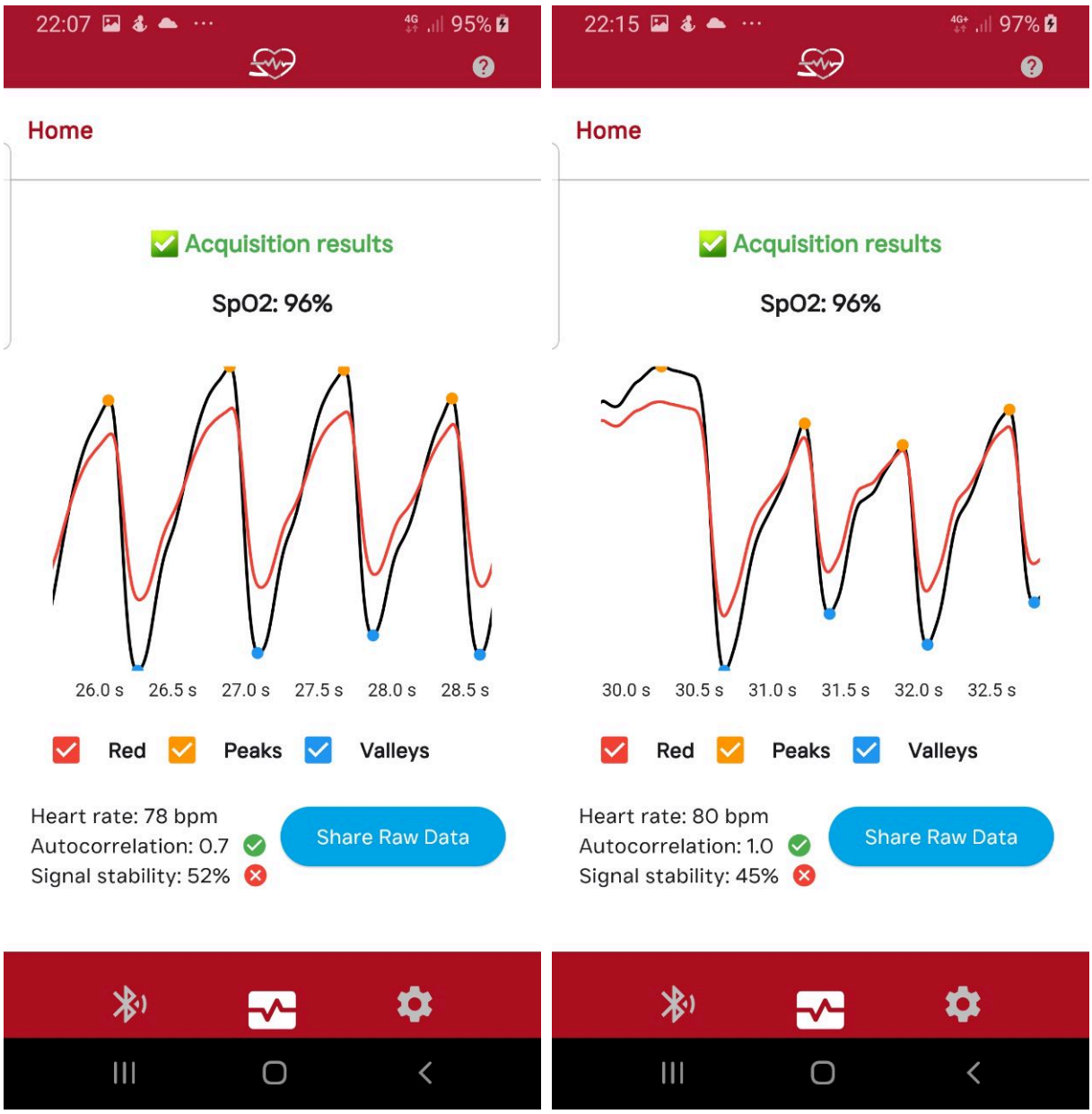

17:13 Fri, May 29
69%
Home
aVR
aVL
aVF
26s
27s
28s

Chapter 7

SpO_2 testing and results

The SpO_2 acquisition functionality has been verified on test subjects (relatives) to verify the performance and calibrate the coefficients of Equation 43. The device was battery-powered and galvanically isolated from the test subjects, hence posing no risk to the test subjects.

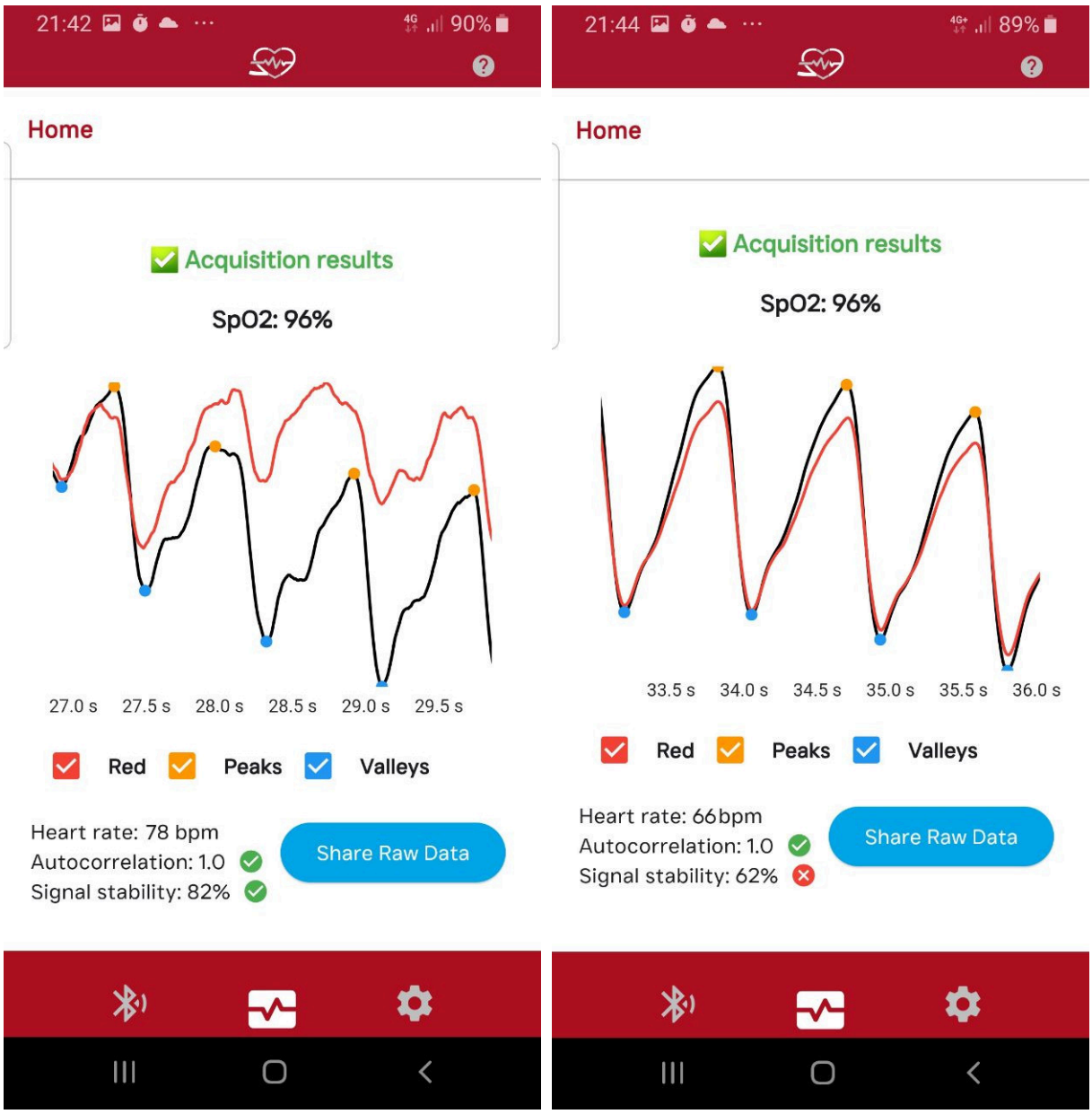
7.1. Volunteer 1



(a) Wrist measurement (b) Thumb measurement

Figure 132: Measured IR and Red waveforms and metrics.

7.2. Volunteer 2

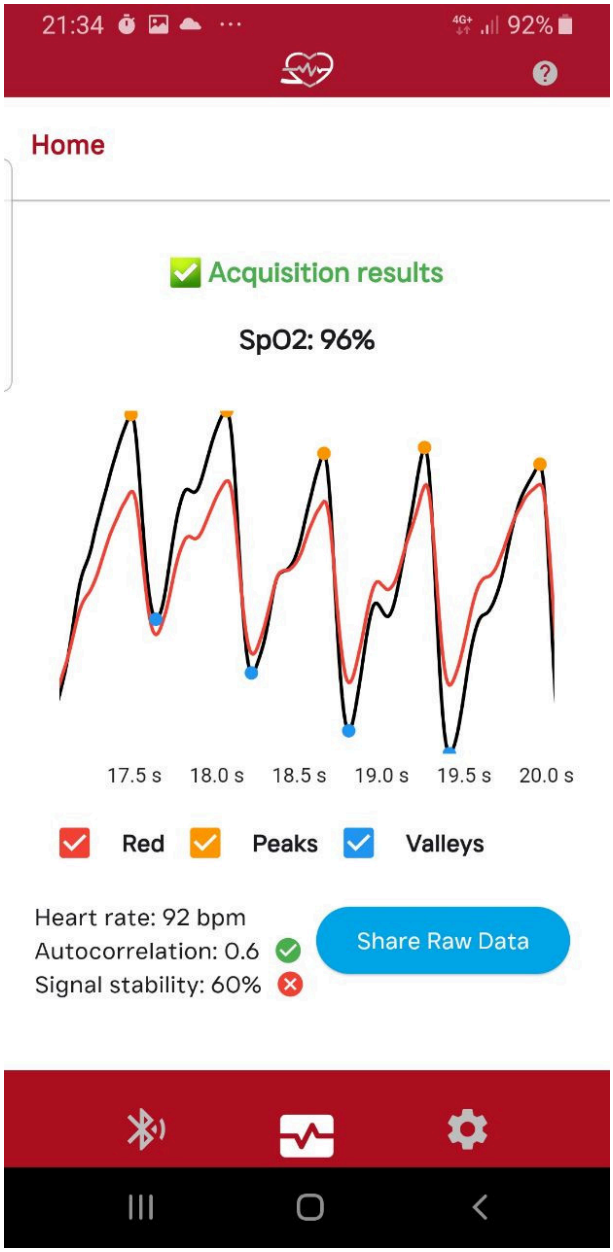


(a) Wrist measurement (b) Thumb measurement

Figure 133: Measured IR and Red waveforms and metrics.

7.3. Volunteer 3

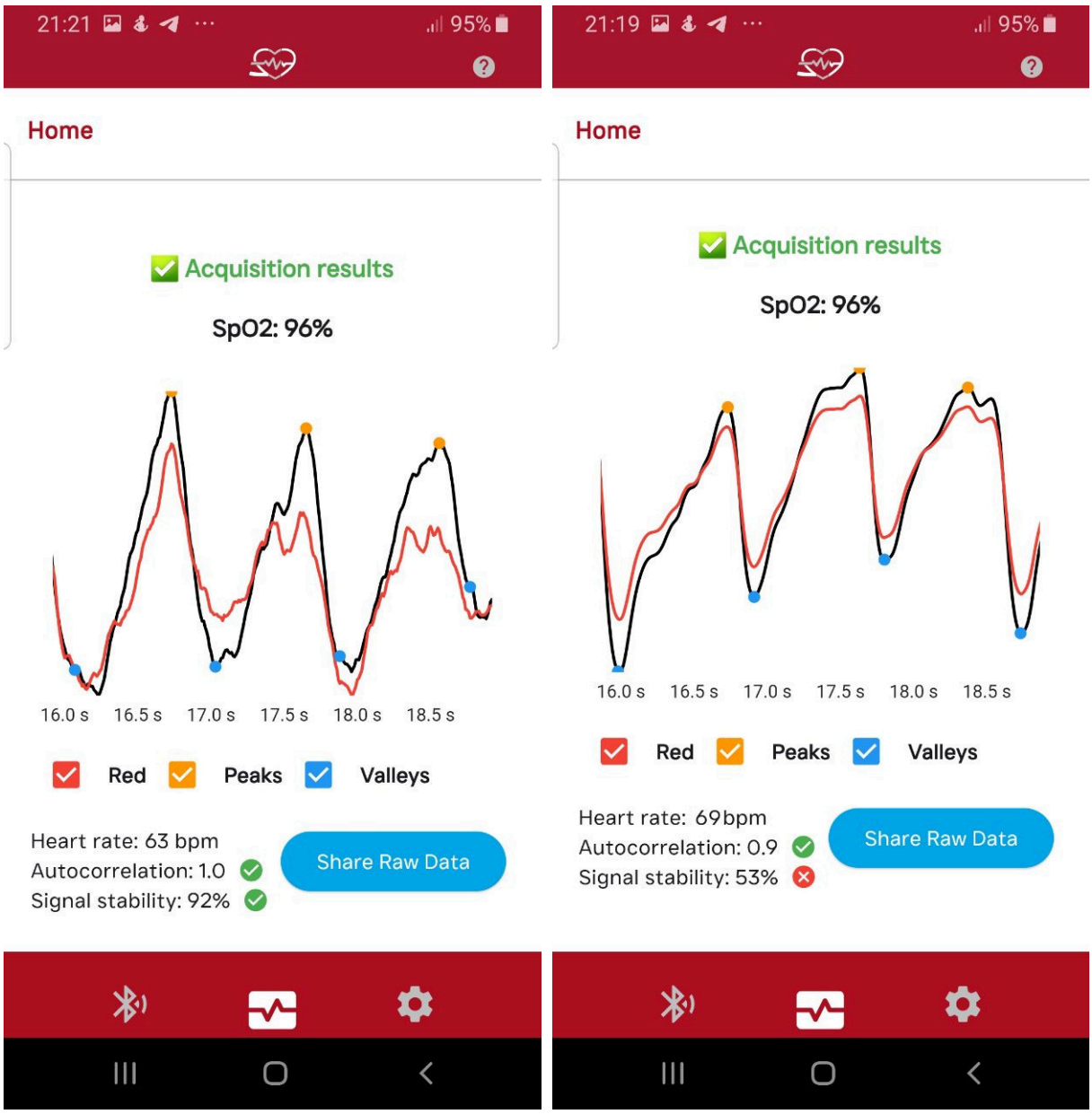
Due to difficulties in measuring the signal at wrist in case of Volunteer 3, only thumb data is available.



(a) Thumb measurement

Figure 134: Measured IR and Red waveforms and metrics.

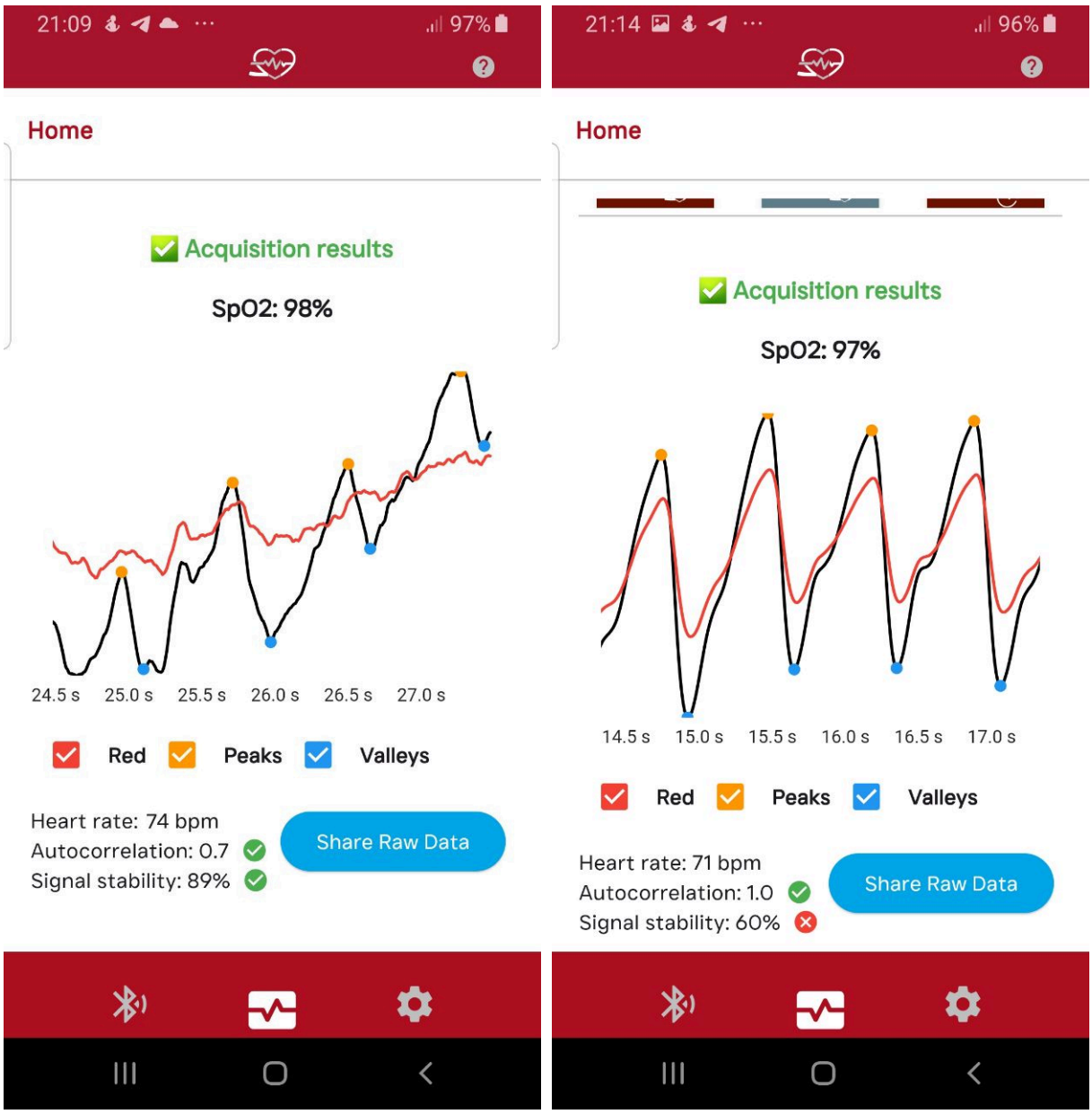
7.4. Volunteer 4



(a) Wrist measurement (b) Thumb measurement

Figure 135: Measured IR and Red waveforms and metrics.

7.5. Volunteer 5



(a) Wrist measurement (b) Thumb measurement

Figure 136: Measured IR and Red waveforms and metrics.

7.6. Observations

Despite the device being capable of measuring SpO_2 and the related metrics, it is evident that wrist measurements yield more noisy and unreliable results, making thumb measurements preferrable. It is still remarkable that the sensor manages to acquire PPG signal at all at the wrist, despite it being designed for in-ear applications and hence being more compatible with thin epidermis of an ear canal.

It is worth noting that the thumb measurements led to higher standard deviation values, which caused the Signal Stability to appear smaller, despite the actual signals being stable.

Chapter 8

Future Improvements

8.1. Insertion of a neural network for remaining leads

The introduced work has put the hardware foundation for the 12-lead ECG measurement with only 5 electrodes. The first subsequent step consists in exploiting the cited Neural Network to recpnstruct the remaining five leads i.e. V_1, V_3, V_4, V_5, V_6, and eventually inserting such neural network capability into the smartphone app itself.

8.2. Devices minimization and components update

Making an additional improvement for both devices consists in a minimization of the design, by changing the package size for all passive and active components scaling from a majority of *0603* components to *0402* or even *0201* package sizes. Furthermore, some components can be replaced with more recent counterparts, like the MAX1759EUB-T. On the PCB, it would be required to accomodate the snap connectors to attach the AG/Cl electrodes to, thus allowing the user to easily replace electrodes when needed, as well as to clean the snap connectors to avoid signal degradation:



Figure 137: Snap connectors for Ag/AgCl electrodes. [25]

8.3. Movement detections systems

In the state of the art devices, a widely adopted solution consists in pausing vital signs reception when the patients movements affect the quality of the measurement, some techniques exist and they imply major controls on both devices firmware and smartphone app sides.

8.4. PPG sensor substitution

As mentioned before, the currently used MAXM86161 PPG sensor is optimized for in-ear applications. To the device more suitable for wrist measurements, the sensor should be replaced with MAX30101, which integrates an optical sub-system, or with MAX86141, which requires external optical components (LEDs and photodiodes). Datasheets of both components confirm the alternatives being designed for wrist applications.

Such substitution would increase signal-to-noise ratio of the PPG signal, and hence improve the precision of the measured metrics.

Bibliography

[1] Fluke Biomedical, "ProSim 2 and 3 Patient Simulator." [Online]. Available: https://www.flukebiomedical.com/products/patient-simulators/prosim-2-and-3-vital-signs-patient-simulators

[2] L. Learning, "Cardiac Muscle and Electrical Activity." [Online]. Available: https://courses.lumenlearning.com/pgcc-ap2/chapter/cardiac-muscle-and-electrical-activity/

[3] U. Embryology, "Cardiovascular System - Heart Histology." [Online]. Available: https://embryology.med.unsw.edu.au/embryology/index.php?title=File:Heart_histology_003.jpg

[4] A. V. W. Willem De Vynck, "Bundle Branch Blocks (LBBB, LAFB, RBBB, Trifascicular Block)." [Online]. Available: https://emergencycarebc.ca/clinical_resource/clinical-summary/bundle-branch-blocks-lbbb-lafb-rbbb-trifascicular-block/

[5] M. Cadogan, "ECG Lead positioning." [Online]. Available: https://litfl.com/ecg-lead-positioning/

[6] My EKG, "Electrocardiogram Paper." [Online]. Available: https://en.my-ekg.com/basic-principles/paper-ekg.html

[7] "Mortara ELI™ 230." [Online]. Available: https://www.praxisdienst.com/it-it/prodotto/mortara-eli-230-senza-cavo/149735

[8] "Cardioline ECG 200L." [Online]. Available: https://www.elettromedicalcenter.it/prodotto/cardioline-ecg-200l/

[9] Wikipedia, "Holter Monitor." [Online]. Available: https://commons.wikimedia.org/wiki/File:Holter_Monitor.png

[10] Omron Healthcare, "KardiaMobile 1L." [Online]. Available: https://www.omron-healthcare.it/prodotti/kardiamobile-1l

[11] Apple Inc., "App ECG e notifiche di ritmo cardiaco irregolare da oggi disponibili su Apple Watch." [Online]. Available: https://www.apple.com/it/newsroom/2019/03/ecg-app-and-irregular-rhythm-notification-on-apple-watch-available-today-across-europe-and-hong-kong/

[12] HowToDevices, "Apple Watch Ultra 3: How to do ECG." [Online]. Available: https://youtu.be/dz-E-2wG6WM?si=hKeTZ_KJj3EeqQHk

[13] M. Technology, "Two/Four/Eight-Channel, 153.6 ksps, Low Noise 24-Bit Delta-Sigma ADCs with Internal Voltage Reference." Jan. 2021. [Online]. Available: https://www.microchip.com/en-us/product/mcp3564r

[14] "Two/Four/Eight-Channel, 153.6 ksps, Low Noise 24-Bit Delta-Sigma ADCs with Internal Voltage Reference, author = MicroChip Technology." Jan. 2021. [Online]. Available: https://www.microchip.com/en-us/product/mcp3564

[15] DigiKey, "SLW-66527511-SMT-TR Slide Switch Product Photo." [Online]. Available: https://www.digikey.it/it/products/detail/same-sky-formerly-cui-devices/slw-66527511-smt-tr/21259964

[16] Global Connector Technology, "USB Type C Receptacle, Through-hole, PCB Top Mount (USB4085) Product Specification." May 2023. [Online]. Available: https://gct.co/files/specs/usb4085-spec.pdf

[17] STMicroelectronics, "Multiprotocol wireless 32-bit MCU Arm®-based Cortex®-M4 with FPU, Bluetooth® 5.4 or 802.15.4 radio solution Datasheet." Aug. 2023. [Online]. Available: https://www.st.com/resource/en/datasheet/stm32wb30ce.pdf

[18] Micro Crystal AG, “CM8V-T1A Tuning Fork Crystal 32.768 kHz Datasheet.” 2019. [Online]. Available: https://www.microcrystal.com/fileadmin/Media/Products/32kHz/Datasheet/CM8V-T1A.pdf

[19] Top Homer, “4 pezzi TENS cavo di filo, elettrodo cavo cavi cavi per decine macchine da 3,5 mm spina a 3,5 mm Snap.” [Online]. Available: https://amzn.eu/d/0aoaE0f0

[20] “AUDIO JACK, author = SAME SKY DEVICES.” Dec. 2024. [Online]. Available: https://www.sameskydevices.com/product/resource/sj2-3594a-smt-tr.pdf

[21] Wikipedia, “Serial Peripheral Interface.” [Online]. Available: https://en.wikipedia.org/wiki/Serial_Peripheral_Interface

[22] “Coolors.” [Online]. Available: https://coolors.co/

[23] F. Loret, “Fingertip Pulsossimetro YM101.” [Online]. Available: https://farmacialoreto.it/fingertip-pulsossimetro-2-458075

[24] CFS, “Elettrodo periferico a piastra F9010SSC - Adulti (conf. 4 pz.).” [Online]. Available: https://www.cfs.it/products/elettrodo-periferico-a-piastra-f9010ssc-adulti-conf-4-pz

[25] AliBaba, “Elettrodo periferico a piastra F9010SSC - Adulti (conf. 4 pz.).” [Online]. Available: https://www.alibaba.com/product-detail/Ecg-Snap-Button-Electrode-3-5mm_62147731703.html

[26] Hypercell, “Li-ion Polymer Battery Specification.” Oct. 2017. [Online]. Available: https://www.mouser.com/catalog/additional/MikroElektronika_HypercellHPL402323-2C-3.7V-190mAhdatasheet.pdf

[27] Analog Devices, Inc., “MAX1555EZK+T Analog Devices / Maxim Integrated Product datasheet.” Mar. 2015. [Online]. Available: https://analog.com/

[28] Maxim Integrated Products, “MAX1759 Buck/Boost Regulating Charge Pump Datasheet.” Jun. 2000. [Online]. Available: https://www.mouser.it/datasheet/3/1014/1/MAX1759.pdf

[29] ROHM Co., Ltd., “1 Channel Compact High Side Switch ICs: 1ch Adjustable Current Limit High Side Switch ICs Datasheet.” Nov. 2020. [Online]. Available: https://fscdn.rohm.com/en/products/databook/datasheet/ic/power/power_switch/bd2242g-e.pdf

[30] Texas Instruments, “REF20xx Low-Drift, Low-Power, Dual-Output, VREF and VREF / 2 Voltage References Datasheet.” Feb. 2022. [Online]. Available: https://www.ti.com/lit/ds/symlink/ref2025.pdf

[31] Samtec, Inc., “Tiger Eye™ Flat IDC Wire Cables (1.27 mm) .050" Pitch - FFSD Series Datasheet.” 2022. [Online]. Available: https://suddendocs.samtec.com/catalog_english/ffsd.pdf

[32] Samtec, Inc., “Surface Mount Micro Header (1.27 mm) .050" Pitch - FTSH Series Datasheet.” 2022. [Online]. Available: https://suddendocs.samtec.com/catalog_english/ftsh_smt.pdf

[33] Texas Instruments, “INA826 Precision, 200-µA Supply Current, 3-V to 36-V Supply Instrumentation Amplifier With Rail-to-Rail Output Datasheet.” Jun. 2020. [Online]. Available: https://www.ti.com/lit/ds/symlink/ina826.pdf

[34] Texas Instruments, “OPAx330 50-µV VOS, 0.25-µV/°C, 35-µA CMOS Operational Amplifiers Zero-Drift Series Datasheet.” Aug. 2016. [Online]. Available: https://www.ti.com/lit/ds/symlink/opa4330.pdf

[35] Microchip Technology Inc., “MCP3561/2/4R Two/Four/Eight-Channel, 153.6 ksps, Low Noise 24-Bit Delta-Sigma ADCs with Internal Voltage Reference Datasheet.” 2021. [Online]. Available: https://ww1.microchip.com/downloads/aemDocuments/documents/APID/ProductDocuments/DataSheets/MCP3561_2_4R-Data-Sheet-DS200006391C.pdf

[36] CTS Corporation, "Model 625 HCMOS Clock Oscillator Datasheet." 2017. [Online]. Available: https://www.ctscorp.com/Files/DataSheets/Passives/FCP/Clock-Oscillators/clock-ocillators-625-datasheet.pdf

[37] Analog Devices, Inc., "MAXM86161 Single-Supply Integrated Optical Module for HR and SpO2 Measurement Datasheet." 2019. [Online]. Available: https://www.analog.com/media/en/technical-documentation/data-sheets/maxm86161.pdf

[38] STMicroelectronics, "MLPF-WB55-01E3: 2.4 GHz Low Pass Filter Matched to STM32WB55Cx/Rx, STM32WB50Cx, STM32WB35Cx and STM32WB30Cx Datasheet." Nov. 2022. [Online]. Available: https://www.st.com/resource/en/datasheet/mlpf-wb55-01e3.pdf

[39] Everlight Americas Inc., "SMD B EAST1616RGBA8 Datasheet." Apr. 2015. [Online]. Available: https://www.mouser.com/datasheet/2/143/EAST1616RGBA8-1595283.pdf

[40] Silicon Labs, "Throughput with Bluetooth Low Energy Technology," 2026, [Online]. Available: https://docs.silabs.com/bluetooth/3.2/bluetooth-general-system-and-performance/throughput-with-bluetooth-low-energy-technology#introduction

[41] S. Antipolis, "Global surge in serious heart rhythm disorders sparks urgent call to action from experts: 1 in 3 people at risks," *Website*, 2025, [Online]. Available: https://www.escardio.org/news/press/press-releases/global-surge-in-serious-heart-rhythm-disorders-sparks-urgent-call-to-action-from/

[42] J. Rojas Camayo *et al.*, "Reference Values for Oxygen Saturation from Sea Level to the Highest Human Habitation in the Andes in Acclimatised Persons," *Thorax*, vol. 73, no. 8, pp. 776–778, 2018, doi: 10.1136/thoraxjnl-2017-210598.

[43] Pfizer, "Flashback: The First ECG ." [Online]. Available: https://www.pfizer.com/news/articles/flashback_the_first_ecg

[44] Gerard H. Smith, Dawie J. Van den Heever,Wayne Swart, "The Reconstruction of a 12-Lead Electrocardiogram from a Reduced Lead Set Using a Focus Time-Delay Neural Network." [Online]. Available: https://www.researchgate.net/publication/348807851_The_Reconstruction_of_a_12-Lead_Electrocardiogram_from_a_Reduced_Lead_Set_Using_a_Focus_Time-Delay_Neural_Network

[45] JST Sales America Inc., "SM02B-SRSS-TB Side Entry Shrouded Header Product Photo." [Online]. Available: https://www.digikey.it/it/products/detail/jst-sales-america-inc/SM02B-SRSS-TB/926708

[46] Mouser Electronics Inc., "MAX1555EZK+T Analog Devices / Maxim Integrated Product Photo." [Online]. Available: https://www.mouser.it/ProductDetail/Analog-Devices-Maxim-Integrated/MAX1555EZK%2BT?qs=LHmEVA8xxfYLEoVKeceKJA%3D%3D

[47] Mouser Electronics Inc., "MAX1759 Buck/Boost Regulating Charge Pump Product Photo." [Online]. Available: https://www.mouser.it/ProductDetail/Analog-Devices-Maxim-Integrated/MAX1759EUB%2bT?qs=Mqkh4jHMT8xogxZdp8jJ3w%3D%3D

[48] Texas Instruments, "REF2025 Dual-Output Voltage Reference Product Photo." [Online]. Available: https://www.ti.com/product/REF2025

[49] Mouser Electronics Inc., "331171302030 Wurth Elektronik WE-SECF EMI Contact Finger Product Photo." [Online]. Available: https://www.mouser.it/ProductDetail/Wurth-Elektronik/331171302030?qs=P%2FTEqz%252BQfnfG6dGWv4bLRQ%3D%3D

[50] DigiKey, "FTSH-105-01-F-DV-K-P-TR Samtec Inc. High Reliability Header Strip Product Photo." [Online]. Available: https://www.digikey.com/en/products/detail/samtec-inc/FTSH-105-01-F-DV-K-P-TR/2649977

[51] DigiKey, “OPA4330AIDR Texas Instruments Quad CMOS Operational Amplifier Product Photo.” [Online]. Available: https://www.digikey.com/en/products/detail/texas-instruments/OPA4330AIDR/2345375

[52] Microchip Technology Inc., “MCP3564R 24-Bit Quad/Octal Channel Delta-Sigma ADC Product Photo.” [Online]. Available: https://www.microchip.com/en-us/product/mcp3564r

[53] Analog Devices, Inc., “MAXM86161: Single-Supply Integrated Optical Module for HR and SpO2 Measurement, Data Sheet, Rev. 1.” 2019. Accessed: Jun. 11, 2026. [Online]. Available: https://www.analog.com/en/products/maxm86161.html

[54] Mouser Electronics Inc., “MAXM86161 Analog Devices / Maxim Integrated Optical Bio-Sensor Product Photo.” [Online]. Available: https://www.mouser.it/new/analog-devices/maxim-maxm86161-optical-bio-sensor/

[55] STMicroelectronics, “Guidelines for meander design using low-cost PCB antennae with 2.4 GHz radio for STM32WB/WB0 MCUs.” Apr. 2024. [Online]. Available: https://www.st.com/resource/en/application_note/an5129-guidelines-for-meander-design-using-lowcost-pcb-antennae-with-24-ghz-radio-for-stm32wbwb0-mcus-stmicroelectronics.pdf

[56] STMicroelectronics, “How to develop RF hardware using STM32WB MCUs.” Apr. 2026. [Online]. Available: https://www.st.com/resource/en/application_note/an5165-how-to-develop-rf-hardware-using-stm32wb-mcus-stmicroelectronics.pdf

[57] Panasonic Corporation, “Small-sized Side-operational SMD Light Touch Switches Type: EVQPU Datasheet.” Mar. 2017. [Online]. Available: https://4donline.ihs.com/images/VipMasterIC/IC/PANA/PANA-S-A0003211477/PANA-S-A0004028532-1.pdf?hkey=CECEF36DEECDED6468708AAF2E19C0C6

[58] STMicroelectronics, “STM32WB35 and STM32WB30 Dual-Core Wireless MCU Product Photo.” [Online]. Available: https://blog.st.com/stm32wb35-stm32wb30/

[59] Seiko Epson Corporation, “MHz Range Crystal Unit FA-128 Specification Datasheet.” 2025. [Online]. Available: https://download.epsondevice.com/td/pdf/brief/FA-128_en.pdf

[60] S. Smith, D. Connell, and B. Christian, “Weight Limits for Double Sided Reflow of QFNs,” in *Proceedings of the SMTA International Conference on Soldering and Reliability (ICSR)*, Surface Mount Technology Association (SMTA), 2010. [Online]. Available: https://www.circuitinsight.com/pdf/weight_limit_qfn_smta.pdf

[61] “AutoDesk Fusion.” [Online]. Available: https://www.autodesk.com/it/products/fusion-360/overview

[62] JLCPCB, “JLCPCB Impedance Calculator.” Accessed: Jun. 11, 2026. [Online]. Available: https://jlcpcb.com/pcb-impedance-calculator

[63] STMicroelectronics, “Integrated Development Environment for STM32.” [Online]. Available: https://www.st.com/en/development-tools/stm32cubeide.html

[64] STMicroelectronics, “STM32CubeProgrammer software for all STM32.” [Online]. Available: https://www.st.com/en/development-tools/stm32cubeprog.html

[65] STMicroelectronics, “STM32CubeWB Copro Wireless Binaries.” [Online]. Available: https://github.com/STMicroelectronics/STM32CubeWB/tree/master/Projects/STM32WB_Copro_Wireless_Binaries/STM32WB3x

[66] P. Lab, “ (Sponsored) STM32 Bluetooth Firmware Tutorial (Bring-Up) - Phil's Lab #129.” [Online]. Available: https://youtu.be/-xYoI84zJew?si=DWQ3_byxpS30ycId&t=577

[67] I. OPAL-RT TECHNOLOGIES, “6 types of communication protocols in embedded systems.” [Online]. Available: https://www.opal-rt.com/blog/6-types-of-communication-protocols-in-embedded-systems/

[68] STMicroelectronics, "Debugging application for ST Bluetooth low energy devices." [Online]. Available: https://www.st.com/en/embedded-software/stbletoolbox.html

[69] "American Heart Association." [Online]. Available: https://www.heart.org/

[70] N. Canac *et al.*, "Algorithm for Reliable Detection of Pulse Onsets in Cerebral Blood Flow Velocity Signals," *Frontiers in Neurology*, vol. 10, p. 1072, 2019, doi: 10.3389/fneur.2019.01072.

[71] Maxim Integrated Products, Inc., "User Guide 6409: MAXREFDES220# Smart SpO2 Presentation System Evaluation Kit." Mar. 2018. [Online]. Available: https://analog.com/

[72] Analog Devices, Inc., "Guidelines for SpO2 Measurement." [Online]. Available: https://www.analog.com/en/resources/technical-articles/guidelines-for-spo2-measurement%E2%80%93maxim-integrated.html

[73] DigiKey, "BD2242G-GTR Power Switch Product Photo." [Online]. Available: https://www.digikey.com/en/products/detail/rohm-semiconductor/BD2242G-GTR/4843515

[74] T. Lan, G. Li, and L. Lin, "A Non-Contact Oxygen Saturation Detection Method Based on Dynamic Spectrum," *Infrared Physics & Technology*, vol. 127, p. 104421, 2022, doi: 10.1016/j.infrared.2022.104421.